Strength characteristics of fine-grained soils at dyke slope surfaces

by

Anand PANTA

A thesis submitted in partial fulfilment of the requirement for the Doctor of Philosophy

Examination Committee: **Prof. Satoshi Nishimura**

Prof. Tatsuya Ishikawa

Prof. Yoichi Watabe

Prof. Koichi Isobe

Division of Field Engineering for Environment

Graduate School of Engineering, Hokkaido University

September 2018

ABSTRACT

Shallow slope instability poses challenging problem to the maintenance of many natural and engineered slopes, as triggered by heavy or incessant rainfall events, and the frequency of such events are predicted to increase due to the global climate change. For the shallow slope stability analysis of such earth structures, accurate characterization of soil strength at low effective stresses (5-20kPa), corresponding to soil failure at shallow depths of about 1-2m depth, is required. The accuracy of characterization of soil strength at the low effective stress, particularly in the fine-grained soils, is strongly dependent on capturing the characteristics of strength envelope with appropriate strength parameters, and how this is affected by soil structure and then potentially altered in field environment. In the first part of this study, the undrained strength behaviours of three fine-grained soils in natural (intact), reconstituted (intrinsic) and compacted states were investigated in laboratory to explore the characteristics of strength at low stresses. The studied fine-grained soils include two natural plastic clays, heavily overconsolidated Izumi clay and soft normally consolidated Atsuma clay, and a clay-sand mixed soil sampled from a river dyke construction site in Maizuru.

The study focused on characterizing the state bounding surfaces of fine-grained soils by performing a series of constant-volume direct shear tests supplemented by hollow cylinder simple shear tests on Izumi clay, Atsuma clay and Maizuru clay-sand mixed soil in intact, reconstituted (intrinsic) and compacted states. Comparisons of non-linear bounding surfaces expressed by a power-law strength criterion for different states of clays suggested that the normalized strength and the degree of its non-linearity at intact states were higher than at the corresponding intrinsic states, probably due to inter-particle bonding as confirmed by the hollow cylinder simple shear tests. Whereas, the normalized compacted strength was significantly lower than the equivalent intrinsic strength, which was explained by meso-scale

discontinuities in the compacted specimens by X-ray micro CT-Images. This difference was not significant in the clay-sand mixed soil. From these observations, it should be noted that the meso-structure in compacted clays is significantly different than that in more homogenous intact and reconstituted clays, and the conventional normalization based on the equivalent pressure concept does not capture it.

In the second part, the study focused on characterizing the temporal and spatial variations in the near-surface strength of river dyke by taking a particular dyke site as example; Maizuru dyke, supplemented by limited data from Higashinosato dyke. Portable static/dynamic cone penetrometer tests were performed on a monthly basis in the year 2016/2017, and the results were interpreted with laboratory-compacted model ground penetration tests and consolidated-undrained triaxial tests. The surface strength of Maizuru river dyke increased gradually with depth showing small spatial and temporal variations in strength, and the strength was consistently found higher at a depth of about 0.4-0.5m from the surface than the Higashinosato river dyke and laboratory-compacted model ground, which were young and showed uniform strength along the depth. This may indicate that the Maizuru surface was subject to crusting (overconsolidation of clays as a result of desiccation) after a few cycles of seasons. The strength of soils from the studied dyke sites was characterized by following the approach discussed in the first part of this study, but with triaxial apparatus. Synthesis of the laboratory-measured strength parameters and the field-measured pore water pressure led to estimated field strength of the shallow layers. This surface strength and static portable cone penetrometer resistance exhibited a correlation consistent with lab-established one for 0.4-0.5m depth, but that for depth shallower than this was significantly different. A further study is necessary to endorse extending a simple, single-line correlation between the strength and cone penetrometer resistance to very shallow depth of compacted earth structure.

ACKNOWLEDGEMENTS

I would like to express my sincere gratitude to my supervisor, Dr. Satoshi Nishimura, for his consistent support, guidance and understanding throughout my study. I am particularly thankful for providing me all the opportunities in the laboratory, in terms of research facilities, laboratory seminars and regular site visits, which helped broaden my knowledge of soil strength characterization.

I would like to extend my sincere gratitude to Prof. Hiroyuki Tanaka and Prof. Yoichi Watabe for their valuable advices on my research in the laboratory seminars and discussions. The advices and assistances from Dr. Fumihiko Fukuda and Mr. Yutaka Kudoh are also gratefully acknowledged.

I would like to thank my senior colleagues Mr. Yohei Sugiyama and Mr. Yuta Fukutomi for their help in performing hollow cylinder simple shear tests. Without their help, it would not have been possible to perform these tests.

I would also like to express my sincere gratitude to all my lab-mates in Soil Mechanics laboratory for their help in this research.

I wish to acknowledge the MEXT scholarship from the Japanese Government through English Engineering Education Program (e3), Graduate School of Engineering, Hokkaido University.

Last but not least, I would like to express my love and gratitude to my wife and my parents for their consistent support and encouragement throughout my study.

TABLE OF CONTENTS

ABSTRACT i
ACKNOWLEDGEMENTS iii
TABLE OF CONTENTS iv
LIST OF FIGURES viii
LIST OF TABLES xiii
LIST OF SYMBOLS xiv
CHAPTER 1 INTRODUCTION 16
1.1 GENERAL BACKGROUND 16
1.1.1 CHARACTERIZATION OF UNDRAINED STRENGTH OF FINE-GRAINED SOILS AT LOW EFFECTIVE STRESSES 17
1.1.2 CHARACTERIZATION OF NEAR-SURFACE STRENGTH OF RIVER DYKE SLOPES UNDER CHANGING CLIMATES 19
1.2 OBJECTIVES OF THE RESEARCH 21
1.3 OUTLINES OF THESIS 22
CHAPTER 2 LITERATURE REVIEW ON SHALLOW SLOPE FAILURE AND ITS STABILITY ANALYSIS 26
2.1 INTRODUCTION 26
2.2 MECHANISM OF SHALLOW SLOPE FAILURE 26
2.3 STABILITY ANALYSIS FOR SHALLOW SLOPE FAILURE 28
2.4 STRENGTH PARAMETERS FOR SHALLOW SLOPE STABILITY ANALYSIS 29
2.5 LINEAR AND NON-LINEAR STRENGTH CRITERIA 31
2.4.1 MOHR-COULOMB FAILURE CRITERION 32
2.4.2 POWER LAW FAILURE CRITERION (ATKINSON, 2007) 33
2.4.3 UNDRAINED STRENGTH EXPRESSION (MITACHI & KITAGO, 1976) 34
2.6 STATE NORMALIZATION AND BOUNDARY SURFACES 34
2.7 STRUCTURED SOIL AND ITS TRUE COHESION 37
CHAPTER 3 LITERATURE REVIEW ON NEAR-SURFACE STRENGTH OF EMBANKMENT SLOPES 39
3.1 INTRODUCTION 39
3.2 NEAR-SURFACE ZONE AND ITS FORMATION MECHANISM 39
3.3 STRENGTH DETERIORATION IN NEAR-SURFACE ZONE 40
3.4 CLIMATE CHANGE AND ITS IMPACT ON SHALLOW SLOPE INSTABILITY 42
3.5 HYDRO-MECHANICAL BEHAVIOUR OF COMPACTED SOIL 43

3.6 COMPACTION VS OVERCONSOLIDATION 44
3.7 COMPACTION OF EMBANKMENTS AND STRESS-STRAIN BEHAVIOUR OF COMPACTED SOIL 45
3.8 CRITICAL STATE FRAMEWORK FOR STATE NORMALIZATION 46
3.9 TRANSITIONAL SOIL AND ITS STRENGTH BEHAVIOUR 49
3.10 IN-SITU STRENGTH TESTING AND FIELD MONITORING IN SHALLOW VEGETATED SLOPES 50
CHAPTER 4 FUNDAMENTAL INVESTIGATION ON FINE-GRAINED SOIL STRENGTH AT LOW STRESSES: MATERIALS AND METHODS 52
4.1 INTRODUCTION 52
4.2 MATERIALS 52
4.2.1 SELECTION OF MATERIALS 52
4.2.2 PHYSICAL PROPERTIES OF TESTED SOILS 54
4.3 METHODS 56
4.3.1 CONSTANT-VOLUME DIRECT SHEAR TEST 57
4.3.2 MERITS AND DEMERITS OF DIRECT SHEAR TEST OVER TRIAXIAL TEST 57
4.3.3 HOLLOW CYLINDER SIMPLE SHEAR TEST 59
4.3.4 ADVANTAGES OF HOLLOW CYLINDER TEST 59
4.4 EXPERIMENTAL PROCEDURES 60
4.4.1 CONSTANT-VOLUME DIRECT SHEAR TEST 60
4.4.2 HOLLOW CYLINDER SIMPLE SHEAR TEST 63
4.5 EXPERIMENTAL PROGRAMMES 69
CHAPTER 5 EXPLORATION OF NEAR-SURFACE STRENGTH OF RIVER DYKE SLOPES: MATERIALS AND METHODS 71
5.1 INTRODUCTION 71
5.2 EMBANKMENT AND FIELD MONITORING 73
5.3 MATERIALS 76
5.4 PREPARATION OF COMPACTED SAMPLES 77
5.5 TESTING METHODS 80
5.5.1 TRIAXIAL COMPRESSION TESTS 80
5.5.2 PORTABLE CONE PENETROMETER TESTS 81
5.5.3 NUMERICAL SIMULATION OF PORE WATER PRESSURE 82
5.6 EXPERIMENTAL PROCEDURES 83
5.6.1 TRIAXIAL COMPRESSION TESTS 83

5.6.2 PORTABLE CONE PENETROMETER TESTS 86
5.7 EXPERIMENTAL PROGRAMMES 89
5.7.1 TRIAXIAL COMPRESSION TESTS 89
5.7.2 PORTABLE CONE PENETROMETER TESTS 91
CHAPTER 6 CHARACTERIZATION OF UNDRAINED STRENGTH OF FINE-GRAINED SOILS AT LOW STRESSES: RESULTS AND DISCUSSIONS 92
6.1 INTRODUCTION 92
6.2 CONSTANT-VOLUME DIRECT SHEAR TEST RESULTS 93
6.2.1 UNDRAINED EFFECTIVE STRESS PATHS AND STRENGTH ENVELOPES 93
6.2.2 NORMALIZED EFFECTIVE STRESS PATHS AND STATE BOUNDING SURFACES 105
6.3 OBSERVATION OF MESO-FABRIC FROM X-RAY MICRO CT-IMAGES 112
6.4 REAPPRAISAL OF DIFFERENT STRENGTH CRITERIA 116
6.5 HOLLOW CYLINDER SIMPLE SHEAR TEST RESULTS 121
6.5.1 UDRAINED EFFECTIVE STRESS PATHS AND PRINCIPAL STRESS STATES 122
6.5.2 CONSTANT-VOLUME DIRECT SHEAR VS HOLLOW CYLINDER SIMPLE SHEAR 127
6.5.3 EXPLORATION OF TRUE COHESION 130
CHAPTER 7 CHARACTERIZATION OF NEAR-SURFACE STRENGTH OF RIVER DYKE SLOPES: RESULTS AND DISCUSSIONS 131
7.1 INTRODUCTION 131
7.2 IN-SITU STRENGTH VARIATIONS FROM PENETROMETER TESTING 132
7.2.1 PORTABLE STATIC CONE PENETROMETER TESTS 132
7.2.2 PORTABLE DYNAMIC CONE PENETROMETER TESTS 135
7.3 UNDISTURBED SOIL SAMPLING, MEASUREMENTS OF IN-SITU WATER CONTENTS AND PARTICLE SIZE DISTRIBUTIONS 138
7.4 RESULTS FROM CONSOLIDATED-UNDRAINED TRIAXIAL COMPRESSION TESTS 140
7.4.1 UNDRAINED EFFECTIVE STRESS PATHS AND STRESS-STRAIN BEHAVIOUR 141
7.4.2 UNDISTURBED VS AS-COMPACTED STATES 148
7.4.3 CONSOLIDATED-UNDRAINED STRENGTH ENVELOPES 152
7.5 PEAK AND CRITICAL STATES 154
7.5.1 NORMALIZING TO TAKE ACCOUNT OF DIFFERENT OCR AND SPECIFIC VOLUMES 158

7.5.2 PEAK STRENGTH AND STRENGTH IN FIELD 160
7.6 FIELD MONITORING 161
7.6.1 MEASUREMENTS OF PRECIPITATION AND SNOW COVER 162
7.6.2 MEASUREMENT OF PORE WATER PRESSURE 163
7.7 NUMERICAL SIMULATION OF PORE WATER PRESSURE 165
7.8 CHARACTERISTICS OF LONG-TERM IN-SITU SURFACE STRENGTH VARIATION 167
CHAPTER 8 CONCLUSIONS, IMPLICATIONS OF RESEARCH FINDINGS AND RECOMMENDATIONS 171
8.1 CONCLUSIONS 171
8.2 MPLICATIONS OF REAEARCH FINDINGS 175
8.3 RECOMMENDATIONS 176
REFERENCES 178

LIST OF FIGURES

Figure 1.1. Schematic diagram of river dyke embankment and shallow slope instability along a near-surface zone 17
Figure 2.1. Schematic illustration of shallow slope failure due to rainfall 27
Figure 2.2. Photographs showing shallow slope failure in Kushiro River dyke due to heavy rainfall in August 2016 (Source: Final investigation report Japanese Geotechnical Society Hokkaido Branch) 28
Figure 2.3. Non-linear failure envelope for compacted London clay (Maksimovic, 1989) 30
Figure 2.4. Illustration of linear Mohr-Coulomb strength envelope of curved failure envelope 33
Figure 2.5. Illustration of power-law strength envelope of non-linear failure envelope 33
Figure 2.6. Illustration of variation of undrained shear strength with pre-shear vertical effective stress for saturated clay (basis of the expression) 34
Figure 2.7. Undrained effective stress paths and state boundary surfaces for overconsolidated and normally consolidated samples 36
Figure 2.8. Comparison of natural and intrinsic state boundary surfaces after normalization with respect to intrinsic equivalent pressure 37
Figure 3.1. Photographs showing shallow slope failure in Kushiro River dyke due to heavy rainfall in August 2016 (Source: Final investigation report by the Japanese Geotechnical Society Hokkaido Branch) 42
Figure 3.2. Comparison of strength behavior between compacted and overconsolidated samples of carbonate sand (Coop, 1990) 45
Figure 3.3. State diagram and definition of variables for critical state normalization 48
Figure 4.1. Preparation of reconstituted samples in a laboratory consolidometer 53
Figure 4.2. Standard proctor compaction curves for tested soils 56
Figure 4.3. Grain size distribution curves for tested soils 56
Figure 4.4. Stress and strain non-uniformities in direct shear test simulated by numerical analysis (Potts et al., 1987) 58
Figure 4.5. Test specimens and stress states (a) Direct shear test (b) Hollow cylinder simple shear test 59
Figure 4.6. Schematic diagram of direct shear apparatus employed in this study 61

Figure 4.7. Constant volume direct shear test (a) Initial preparation of shear box (b) Shear box with specimen before consolidation stage 62
Figure 4.8. Hollow cylinder simple shear test (a) Specimen preparation (b) Specimen set up 66
Figure 4.9. Experimental procedure and soil specimen states for hollow cylinder simple shear tests 67
Figure 4.10. Hollow cylinder simple shear tests (a) Problem of interface slippage during shearing in intact Izumi clay (b) Simple shear deformation during simple shearing 68
Figure 5.1. Photograph showing locations of Maizuru, Higashinosato and Ebetsubuto river dykes 72
Figure 5.2. Cross-section of embankment, field monitoring instrumentation and testing locations for static/dynamic cone penetrometer tests in Maizuru site 74
Figure 5.3. Photographs showing surface conditions in Maizuru river dyke (a) overall view of dyke surrounding (b) 02-Feb-2016(c) 10-March-2016 (d) 13-May-2016(e) 05-Sep-2016 (f) 12-Nov-2016 76
Figure5.4. Standard proctor compaction curves for tested soils 78
Figure 5.5. Particle size distribution curves for tested soils 78
Figure 5.6. Sample preparation (a) Clay-sand mixed soils from Maizuru embankment (b) Standard proctor mould and hammer used for soil compaction 79
Figure 5.7. Schematic diagram of cone penetrometer apparatus (a) static (b) dynamic 82
Figure 5.8. Photograph of mega-torque triaxial apparatus used in this study and stress states in triaxial specimen 84
Figure 5.9. Calibration of cone penetrometer in laboratory-compacted model ground 87
Figure 5.10. Depth profiles of penetration resistance from static cone penetrometer tests performed in laboratory-compacted model ground (a) container with different diameters but same water content (b) container with same diameter but different water contents 88
Figure 5.11. Depth profiles of penetration resistance from dynamic cone penetrometer tests performed in laboratory-compacted model ground 88
Figure 5.12. Depth profiles of suction and water content measured in laboratory-compacted model ground 89
Figure 5.13. Plans and dates of cone penetrometer testing in Maizuru river dyke slope 91

Figure 6.1. Undrained effective stress paths and strength envelopes for Izumi clay (a) Intact state (b) Reconstituted state (c) Compacted state (d) Effective strength envelopes (e) Consolidated-undrained strength envelopes 97
Figure 6.2. Undrained effective stress paths and strength envelopes for Atsuma clay (a) Intact state (b) Reconstituted state (c) Compacted state (d) Effective strength envelopes (e) Consolidated-undrained strength envelopes 102
Figure 6.3. Undrained effective stress paths and strength envelopes for clay-sand mixed soil (a) Reconstituted state (b) Compacted state (c) Effective strength envelopes (d) Consolidated-undrained strength envelopes 104
Figure 6.4. (a) Normalized stress paths and state bounding surfaces (b) Compression curves and volume-effective stress states before undrained shearing 108
Figure 6.5. (a) Normalized stress paths and state bounding surfaces (b) Compression curves and volume-effective stress states before undrained shearing 109
Figure 6.6. (a) Normalized stress paths and state bounding surface (b) Compression curves and volume-effective stress states before undrained shearing 111
Figure 6.7. X-ray micro-CT images for Izumi clay (a) reconstituted state (b) compacted state 114
Figure 6.8. X-ray micro-CT images for Atsuma clay (a) reconstituted state (b) compacted state 115
Figure 6.9. X-ray micro-CT images for clay-sand mixed soil (a) reconstituted state (b) compacted state 116
Figure 6.10. Variation of undrained strength ratio (τ/σ'_0) with OCR for different states of (a) Izumi clay (b) Atsuma clay (c) Clay-sand mixed soils 121
Figure 6.11. Mohr's stress circles and stress-strain curves for Izumi clay (a) Intact state (b) Reconstituted state (c) Compacted state 123
Figure 6.12. Mohr's stress circles and stress-strain curves for Atsuma clay (a) Intact state (b) Reconstituted state (c) Compacted state 125
Figure 6.13. Mohr's stress circles and stress-strain curves for clay-sand mixed soil (a) Reconstituted state (b) Compacted state 126
Figure 6.14. Comparison of undrained effective stress paths between direct shear and hollow cylinder simple shear for Izumi clay (a) Intact state (b) Reconstituted state (c) Compacted state 128

Figure 6.15. Comparison of undrained effective stress paths between direct shear and hollow cylinder simple shear for Atsuma clay (a) Intact state (b) Reconstituted state (c) Compacted state 129
Figure 6.16. Comparison of undrained effective stress paths between direct shear and hollow cylinder simple shear for clay-sand mixed soil (a) Reconstituted state (b) Compacted state 129
Figure 6.17. Evolution of Mohr's stress circle and strength envelopes for intact Izumi clay 130
Figure 7.1. Results from static cone penetrometer tests in different regions along the slope in Maizuru embankment slope 134
Figure 7.2. Depth profiles of penetration resistance in Maizuru embankment slope, Higashinosato embankment slope and lab-compacted Ebetsubuto soil 135
Figure 7.3. Depth profiles of penetration resistance from dynamic cone penetrometer tests (a) Maizuru embankment (b) Higashinosato embankment 137
Figure 7.4. Depth profiles of water content and penetration resistance during undisturbed sampling in Maizuru embankment slope on 21 October, 2017 139
Figure 7.5. Particle size distribution curves for near-surface soil at different depths in Maizuru embankment slope 140
Figure 7.6. Undrained effective stress paths and stress-strain curves for as-compacted Ebetsubuto soil (a) Stress paths (b) Deviatoric stress-axial strain curves (c) Excess pore water pressure-axial strain curves 144
Figure 7.7. Undrained effective stress paths and stress-strain curves for as-compacted Higashinosato soil (a) Stress paths (b) Deviatoric stress-axial strain curves (c) Excess pore water pressure-axial strain curves 146
Figure 7.8. Undrained effective stress paths and stress-strain curves for Maizuru soil (a) Stress paths (b) Deviatoric stress-axial strain curves (c) Excess pore water pressure-axial strain curves 148
Figure 7.9. Comparison of undrained effective stress paths between as-compacted Ebetsubuto and Higashinosato soils, and undisturbed Maizuru soil 150
Figure 7.10. Comparison of stress-strain behaviour between undisturbed samples and as-compacted samples (a) Undrained effective stress paths (b) Stress ratio 152
Figure 7.11. Consolidated-undrained strength envelopes for as-compacted Ebetsubuto and Higashinosato soils, and undisturbed Maizuru soil 153
Figure 7.12. Critical state lines for as-compacted Ebetsubuto and Higashinosato soils, and undisturbed Maizuru soil in *q-p'* space 156

Figure 7.13. Critical state lines for as-compacted Ebetsubuto and Higashinosato soils, and undisturbed Maizuru soil in *v*-log*p'* space 156
Figure 7.14. Non-linear peak strength envelopes for as-compacted Ebetsubuto and Higashinosato soils, and undisturbed Maizuru soil in *q*-*p'* space 157
Figure 7.15. Normalized peak strength envelopes for as-compacted Ebetsubuto and Higashinosato soils, and undisturbed Maizuru soil 160
Figure 7.16. Records of daily and hourly rainfall from 1-Jan-2016 to 8-May-2017 163
Figure 7.17. Time series of field measured pore water pressure at different depths from 1-Jan-2016 to 8-May-2017 164
Figure 7.18. Depth profiles of pore water pressure measured on the day of cone penetrometer tests 165
Figure 7.19. Time series of field measured PWP and simulated PWP at 0.4m depth 166
Figure 7.20. Comparison of the field measured and simulated pore water pressure on the day of cone penetrometer testing 167
Figure 7.21. Flow chart showing steps followed to make correlations between penetration resistance and undrained strength in the field and laboratory 168
Figure 7.22. Correlations of static cone penetration resistance and undrained strength 170
Figure 7.23. Correlations of dynamic cone penetration resistance and undrained strength 170

LIST OF TABLES

Table 4.1. Summary of physical properties of Izumi clay, Atsuma clay and clay-sand mixed (C-S) soil 55
Table 4.2. Summary of constant-volume direct shear tests on Izumi clay, Atsuma clay, and clay-sand mixed soil 70
Table 4.3. Summary of hollow cylinder simple shear tests on Izumi clay, Atsuma clay, and clay-sand mixed soil 70
Table 5.1. Physical properties of tested materials 80
Table 5.2. Experimental programme for Isotropic triaxial compression tests 90
Table 6.1. Summary of Mohr-Coulomb effective and total stress strength parameters for different states of tested soils 118
Table 6.2. Summary of power law strength parameters in un-normalized and normalized form for different states of tested soils 119
Table 6.3. Summary of parameter (1-*m*) for intact and reconstituted states of tested soils 120
Table 6.4. Summary of rotation of principal stresses (α) at the ultimate state during simple shearing for different states of tested soils 127
Table 7.1. Peak and critical state parameters for as-compacted Ebetsubuto and Higashinosato soils, and undisturbed Maizuru soil 157

LIST OF SYMBOLS

σ'	Vertical effective stress
c', φ'	Mohr-Coulomb effective strength parameters
φ'_{crit}	Effective critical friction angle
σ'_0	Initial vertical consolidation pressure
σ'_p	Pre-shear vertical effective stress in normally consolidated sample
τ_1	Undrained shear strength in normally consolidated sample
C_c	Compressibility index
C_s	Swelling index
Δu	Excess pore water pressure
A, b	Power law strength parameter in equation 2.3
τ^*	Normalized shear strength
σ'^*	Normalized vertical effective stress
v	Specific volume
v_Γ	Specific volume intercept at unit pressure (p'=1kPa)
λ	Compression index
C_c^*	Intrinsic compressibility index
c_u	Undrained shear strength
e	Void ratio
e_0	Void ratio before undrained shearing
G_s	Specific gravity
K_0	Coefficient of earth pressure at rest
N	Intercept of intrinsic compression line at 1kPa
R	Correlation coefficient
S_r	Degree of saturation
v_0	Specific volume before undrained shearing
w	Water content
w_L	Liquid limit

w_n	Natural water content
w_{opt}	Optimum water content
w_p	Plastic limit
$\alpha,\ \beta$	Power law strength parameter in equation 2.6
ε	Normal strain
γ_d	Dry unit weight
$\gamma_{z\theta}$	Torsional shear strain as calculated from to cap rotation
σ_v', σ_z'	Effective normal stress
$\sigma_1, \sigma_2, \sigma_3$	Principal stresses
σ_{ve} *	Intrinsic vertical equivalent pressure
σ_{vy}'	Vertical effective yield stress
τ	Shear stress
$\tau_{z\theta}$	Torsional shear stress
θ	Torsional rotation of soil specimen
q	Deviatoric stress
M	Gradient of critical state line
p'	Mean effective stress
q_c	Penetration resistance from static cone penetrometer tests
c_u	Undrained strength as defined by maximum shear stress
γ_d	Dry unit weight
φ_{cu}	Consolidated undrained angle of internal friction
c_{cu}	Consolidated undrained cohesion intercept
μ, η	Power law strength parameters in equation 3.6
m, n	Power law strength parameters in equation 3.5
p_c'	Critical equivalent pressure
ε_a	Axial strain
w_{opt}	Optimum water content

CHAPTER 1 INTRODUCTION

1.1 GENERAL BACKGROUND

Shallow slope instability due to heavy or incessant rainfall events poses challenges to the maintenance of earth structures such as natural slopes and embankments. The embankments such as highway embankments and river dykes etc. require attention in terms of saving huge loss of lives and economy every year around the world. In this study, river dykes which are under construction in Hokkaido are chosen to characterize the strength of their material in both laboratory and field considering the impact of climate and vegetation, as illustrated in **Figure 1.1**. The materials used for the construction of these river dykes, which are the mixture of locally available Holocene clay and sand in compacted states, still remain less studied in contrast to clays with regard to hydraulic and mechanical behavior require for the slope design and stability analysis. The soil models under a critical state soil mechanics framework to describe the mechanical behavior of natural soils have been developed based on reconstituted soil such as cam clay model, modified cam clay model, etc. As the shallow slope failure in the river dyke slope triggers due to rain-water infiltration at a nearly-saturated condition, to describe the mechanical behavior of compacted soils under the critical state soil mechanics framework simulating such condition, and to extend the scope to describe an unsaturated soil behavior, it is important to understand the compacted strength characteristics in comparison to reconstituted soils. The peculiar strength characteristics of clay-sand mixed soil showing an intermediate behavior between clay and sand and non-unique intrinsic properties have always received attention of researchers, particularly in identifying the influence of soil structure on the strength behavior. After the construction of river dykes, the compacted soil near the surface of the slope receives loading processes due to drying-wetting

cycles and may develop complex soil structures significantly different than the initial as-compacted state. In this research, a comprehensive laboratory and field characterization of compacted clay-sand mixed soils involved in the river dyke construction in comparison to conventionally investigated clays at low effective stresses has been carried out by dividing the research into two parts as describe in the following sections.

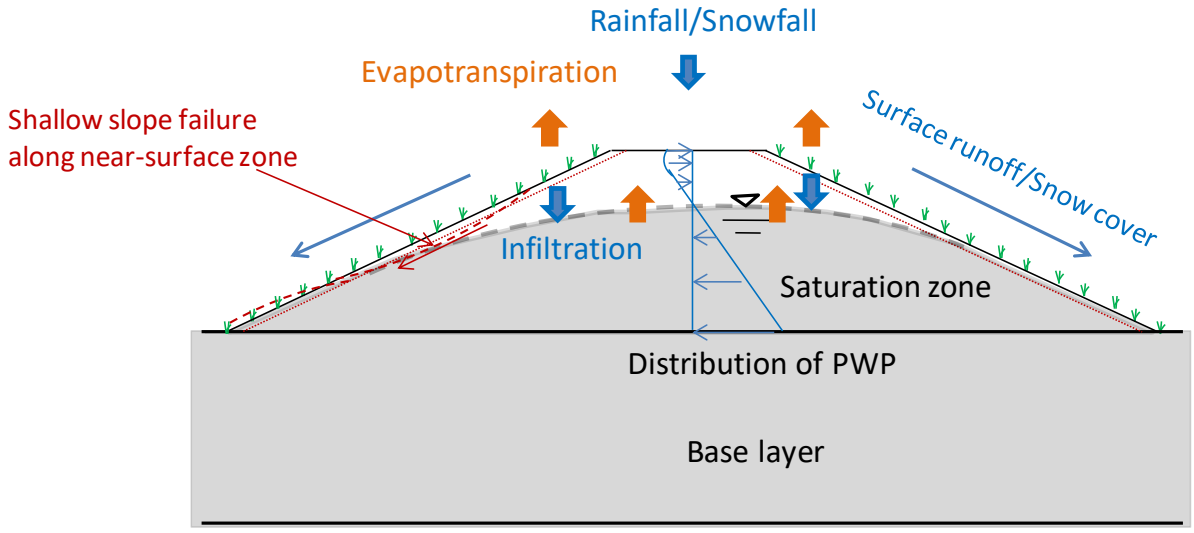

Figure 1.1. Schematic diagram of river dyke embankment and shallow slope instability along a near-surface zone

1.1.1 CHARACTERIZATION OF UNDRAINED STRENGTH OF FINE-GRAINED SOILS AT LOW EFFECTIVE STRESSES

Dykes are natural or man-made geostructures, which are found along the floodplain of river and the coastline of sea to prevent flooding in low lying areas, encounter some of the challenging problem of shallow slope instability during heavy rainfall events. The current global issue of climate change, which predicts to increase the frequency of heavy rainfall events, makes this problem more challenging. It is evident that the shallow slope failure in fine-grained soils is occurred at near-saturation conditions due to the reduction in effective stress and the swelling caused by water infiltration (Gamez and Stark, 2014). The shallow

slope failure in densely compacted fine-grained soils can be governed by an undrained failure mechanism, although the pore water pressure due to rain-water infiltration could develop initially under a drained condition, but the eventual failure is quick and undrained. The effective stress involved in such a shallow failure surface lies in a range of 5-20kPa corresponding to a failure mechanism at 1-2m depth. Hence the appropriate choice of shear strength parameters at this low stress range is vital for the purpose of slope design and stability analysis. However, a number of studies have revealed that determining the appropriate strength parameters at the low stress range can be a difficult task, as a linear extrapolation of the Mohr-Coulomb failure envelope from higher to lower stress ranges greatly over-estimates the shear strength and eventually the factor of safety (Maksimovic, 1989; Day, 1992; Mesri, 1993; Baker, 2004; Atkinson, 2007). Therefore it is very important to consider the non-linearity of shear strength envelope to assess a true state of soil in a slope and render an acceptable analysis result. A power-law failure criterion, similar to that familiar in rock mechanics, is a widely used non-linear failure criterion at low stresses to represent the non-linear strength envelope of soils (de Mello, 1977; Charles, 1982).

Several previous researches (e.g. Seed and Chan, 1959; Barden and Sides, 1970; Burland 1990; Leroueil and Vaughan, 1990; Gens, 1996; Cotecchia and Chandler, 2000) have reported that the strength parameters, whatever failure criterion is employed, are never inherent properties and are strongly dependent on the soil state and structure. Many of these studies were conducted at relatively large stress ranges (>50kPa), especially in the natural and reconstituted clays, in which the reconstituted clay was chosen as a reference to identify the effect of soil structure on the strength behaviour of natural soils under the critical state soil mechanics framework (e.g. Burland, 1990; Leroueil and Vaughan 1990; Cotecchia and Chandler, 2000). The role of natural structures enhancing the strength of soil has been

highlighted. The term structure in soil is defined as a combination of 'fabric', the arrangement of soil particles, and 'bonding', the inter-particle resistance, other than purely frictional nature (Mitchell, 1976). The dykes of interest in this study were constructed with compacting the fine-grained soils, particularly the intermediate clay-sand mixed soils. Therefore, the first part of this study experimentally investigated the undrained strength characteristic of intermediate clay-sand mixed soils in comparison with plastic clays in three different states (intact, reconstituted, and compacted) in terms of state bounding surfaces by using the reconstituted soil as a reference.

1.1.2 CHARACTERIZATION OF NEAR-SURFACE STRENGTH OF RIVER DYKE SLOPES UNDER CHANGING CLIMATES

Geotechnical earth structures such as natural or artificial river dyke embankments are considered to be susceptible to deterioration of its near-surface strength due to the action of climate such as a range of extreme events of heavy rainfall and prolonged drying. The frequency of such extreme events is projected to increase due to the global problem of climate change, as mentioned in the earlier section, which has the potential to pose a challenging problem to exacerbate such deterioration process. As a result, a region near the surface of the slope, with significantly different soil properties, which is defined as a 'near-surface zone', develops with time after the construction of the embankments (Glendening et al., 2014). However, its development mechanism has yet to be well understood.

In the embankments constructed with fine-grained soils, the changes in pore water pressure owing to the climatic variation and associated vegetation cause repeated changes in stress and volumetric strain in the near-surface zone. This may subsequently result in plastic strain and eventually the degradation in strength of soil (O'Brien et al., 2004; Smethurst et al., 2012; Stirling et al., 2017). Loveridge et al. (2010) reported that the increase in pore water pressure

leading to a state of instability in the near-surface soil depends on the permeability of soils, which governs the pattern of infiltration in association with evapo-transpiration by the vegetation, with regards to the antecedent rainfall. Glendening et al. (2014) reported that the permeability of soil in the near-surface zone of the embankment slope increased up to four orders of magnitude and the pore water pressure changed significantly. This could be attributed to the climate-induced changes in soil fabric in the near-surface zone, probably as a result of desiccation-induced cracking and the swelling caused by rainwater infiltration.

A desiccated crust can develop in the near-surface soil owing to the desiccation-induced volume shrinkage and cracking during drying period. Stirling et al. (2017) reported that the desiccated crust was characterized by disintegrated texture, and highly negative pore water pressure and extremely low permeability. Mitchell and Soga (2005) explained that the desiccation-induced volume shrinkage and cracking can cause overconsolidation in the near-surface soil. As a result, during heavy or incessant rainfall events, a perched water table with positive pore water pressure may develop, which further decreases the shear strength of soil and makes the slope susceptible to failure (Ng et al., 2003; Lee et al, 2009).

The hydro-mechanical behaviour of soil in the near-surface zone governing the shallow slope instability can be significantly influenced by the swelling of soil during rainfall period, and desiccation and subsequent development of shrinkage and cracking during drying period. This shallow slope instability usually triggers along the near-surface zone, when the pore water pressure rises closer to the hydrostatic levels, due to the enhanced rainwater infiltration after drying period (Day and Axten, 1989; Rahardjo et al., 1995; Fourie et al., 1999; Gamez and Stark, 2014). Therefore, a long-term comprehensive field monitoring of climatic and hydraulic changes (Rahardjo et al., 2008; Springman et al., 2013) and associated in-situ strength testing are crucial for the sound slope stability analysis.

In this study, as the studied embankments in Hokkaido, Japan, were being constructed with the compacted clay-sand mixed soils, which are also called as intermediate or transitional soils. The compression and shearing behaviour of such soils are strongly dependent on the initial compaction soil density or specific volume. Several past studies were conducted in laboratory to know the compression and shearing behaviour of varieties of clay-sand mixed soils (Ferreira and Bica, 2006; Shipton and Coop, 2012; Coop, 2015; Xu and Coop, 2016). They reported that it was difficult to obtain unique normal compression and critical state lines based on initial densities for such soils, and hence to assess the effect of soil structure in the strength behaviour of natural soil without the unique intrinsic strength properties under the critical state framework, unlike in clays. However, they eventually concluded that the critical state framework can be applicable to the transitional soils by using a family of separate critical state lines based on the initial densities. In the second part of this study, to understand the strength behaviour of field and laboratory-compacted clay-sand mixed soils under the similar framework, a comprehensive laboratory and field strength characterisation with reference to laboratory-compacted soils was made.

1.2 OBJECTIVES OF THE RESEARCH

The key objectives of the first part of this research are summarized as follows:

1. To understand the strength characteristics of compacted intermediate soils typically used for dykes at low stresses, with reconstituted state as reference. To gain deeper understanding on the influence of micro/meso soil structure on the strength, the naturally structured clays will be included in the study.

2. To identify and highlight important features of the strength characteristics peculiar to sand-clay mixed intermediate soils, through broader comparison with more conventionally investigated soils such as plastic clays.

The key objectives of the second part of this research are summarised as follows:

1. To characterize the temporal and spatial variations in strength of river dykes, in particular along the near-surface zone, by investigating recently built river dykes, and interpreting them with the laboratory-compacted soil strength as reference.

2. To understand the stress-strain behaviour of the near-surface soil of river dyke slope with reference to the laboratory-compacted soils under the critical state framework.

3. To explain any deviation of the observed field strength from laboratory strength, noting differences in the conditions after compaction.

1.3 OUTLINES OF THESIS

This thesis consists of eight chapters in total. The introduction and objectives of this research have been presented in the present **Chapter 1**.

Chapter 2 presents a literature review on the shallow slope failure and its stability analysis issues. This includes the mechanism of shallow slope failure, strength parameters at low effective stresses, and various linear and non-linear strength criteria. In this chapter, the critical state soil mechanics framework and its application to assess the state boundary surfaces of different states of soil after normalizing by the equivalent pressure on the normal compression line are also introduced. Finally, the role of soil structure and its influence on the strength behaviour of structured soil is discussed.

Chapter 3 presents a literature review on the strength of near-surface soil in embankment slopes and its variation with time as a result of climate and vegetation. The current global issue of climate change, which has the potential to increase the frequency of heavy rainfall and eventually trigger the shallow slope failure along the near-surface zone, is also discussed briefly. In this chapter, the hydro-mechanical behaviour of soil, focusing on soil structures induced by wet and dry compaction and overconsolidation, is then presented. The strength behaviour of clay-sand mixed intermediate soil under the critical state soil mechanics framework is also reviewed. Finally, the field monitoring and in-situ strength testing to explore the in-situ strength of shallow vegetated slope are presented briefly.

Chapter 4 introduces the materials and methods employed in the first part of this research. This chapter discusses the criteria for selection of suitable materials, and the preparation of specimens for shear tests. Selection of the suitable experimental methods is also described with their merit and demerit over other methods. The methods include the constant-volume direct shear test supplemented by the hollow cylinder simple shear test. The experimental procedures adopted for both the tests in this research are also discussed in this chapter.

Chapter 5 presents the embankments, field monitoring, materials and methods used in the second part of this research. The studied embankments include Maizuru river dyke with a field monitoring station, and Higashinosato river dyke. This chapter discusses the physical properties of materials used for the construction of these river dykes, particularly the clay-sand mixed intermediate soils, and the preparation of compacted specimens for the laboratory tests. The laboratory strength tests include consolidated-undrained triaxial tests and in-situ strength tests include portable static/dynamic cone penetrometers tests which are then described. The simulation of pore water pressure by using a finite element seepage flow

model is also described. Finally, the details of experimental procedure and programme adopted for each test are presented.

Chapter 6 presents the experimental results obtained from both the constant-volume direct shear and hollow cylinder simple shear tests in the first part of this research. The results are analysed and interpreted based on undrained effective stress paths, and linear and non-linear failure envelopes. The corresponding strength parameters are derived and compared with the different states of soils. In this chapter, the state bounding surfaces for intact, reconstituted and compacted states of all the tested soils are analysed and compared in a single framework by using the state normalization based on the intrinsic equivalent pressure. The evolution of principal stresses during hollow cylinder simple shearing is analysed by drawing Mohr's stress circles, and the presence of true cohesion in the structured soil is explored.

Chapter 7 presents the results obtained from the in-situ strength tests, laboratory tests, field monitoring and numerical simulation in the second part of this study. The results of in-situ strength tests in terms of penetration resistance in the river dykes are interpreted and discussed by considering spatial and temporal variations. The results of consolidated-undrained strength tests on different states of clay-sand mixed soils are presented in terms of stress-strain curves, undrained effective stress paths and undrained strength envelopes. All normalized peak strength envelopes (normalized for different densities and apparent OCR with respect to equivalent critical pressure on the critical state line) constituting state boundary surfaces at the dry side of the critical for different states of compacted soils are presented in a single framework. Finally, correlations of the penetration resistance obtained in the field and laboratory at different depths with the undrained strength obtained from the triaxial tests are discussed.

Chapter 8 presents the conclusions drawn on different parts of this thesis. The implications of research findings and recommendations for further work are also presented.

CHAPTER 2 LITERATURE REVIEW ON SHALLOW SLOPE FAILURE AND ITS STABILITY ANALYSIS

2.1 INTRODUCTION

In this chapter, a literature review is made on the shallow slope instability, which forms background information for the first part of this research. The literature review particularly focuses on the mechanism of slope failure, the strength parameters require for the stability analysis, and the critical state soil mechanics framework to understand the effect of soil structure on the strength behaviour of different states of soils. As mentioned in Chapter 1, this instability problem is triggered especially after the heavy or prolonged rainfall events and sometimes after the snow melting events in natural and constructed slopes at a nearly-saturated condition. The failure surface is shallow and often parallel to the slope surface. Therefore, the strength parameters at a low stress range are necessary. However, the non-linearity of strength envelopes at the low stress range always creates a problem of getting the appropriate strength parameters, which makes the stability analysis result more divergent. Several non-linear strength functions have been proposed by researchers to approximate the strength parameters, such as bilinear functions, trilinear functions etc.; a simple power-law strength criterion is a widely used strength criterion at low stress ranges.

2.2 MECHANISM OF SHALLOW SLOPE FAILURE

It is revealed that the soil failure mechanism involved in the shallow slope failure is typically owing to the infiltration of rain water and the subsequent rise in pore water pressure, which reduces the soil shear strength and increases the instability driving force as the soil becomes heavier when wet on the potential failure surface (Rahardjo et al., 1995; Fourie et al., 1999). Most of such failures are triggered during rainfall or snowmelt events when the soil reaches a

near-saturated condition. In the shallow slope failure, the failure surface develops normally at a shallow depth and extends parallel to the slope surface, as illustrated in the **Figure 2.1**. The photographs in **Figure 2.2** show an example of shallow slope failure in Kushiro River dyke in August 2016 due to heavy rainfall demonstrating the similar mechanism of slope failure. The study carried out by Day and Axten (1989) on the embankment slope made up of compacted clay observed the similar mechanism of shallow slope failure; the failure was triggered when the slope exposed to seasonal rainfall events. They mentioned that in dry or hot season the soil becomes desiccated and shrunken, whereas in the wet or rainy season the rain-water infiltrates into the fissures which eventually causes the soil to swell, and thus enhances the saturation; which subsequently lead to the reduction in soil shear strength and causes the shallow slope failure.

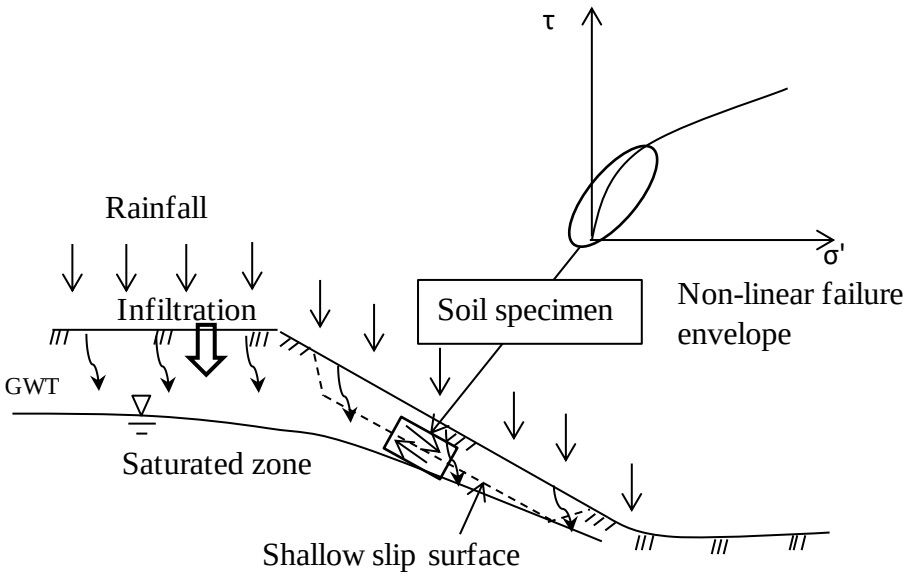

Figure 2.1. Schematic illustration of shallow slope failure due to rainfall

Figure 2.2. Photographs showing shallow slope failure in Kushiro River dyke due to heavy rainfall in August 2016 (Source: Final investigation report Japanese Geotechnical Society Hokkaido Branch)

2.3 STABILITY ANALYSIS FOR SHALLOW SLOPE FAILURE

Assigning the appropriate strength parameters of soil reflecting the failure mechanism in the field are essential for the stability analysis models, which is usually done in two basic approaches, i.e total stress analysis and effective stress analysis. The strength parameters in these analyses are usually determined by drained and undrained strength tests. The right choice of the drained or undrained strength parameters for a particular slope is governed by soil types, drainage conditions, time duration of failure and corresponding generation of excess pore water pressure. The drainage of soil is dependent upon the permeability. Most of the shallow slope failures in the low-permeability dense fine-grained soils involve the mechanism governed by the reduction in soil strength owing to the generation of high pore water pressure, in which the pore water pressure starts increasing from initial suction to positive pressure with slow initial deformation, and the mass of soil fails suddenly and turn into flow like slides (Chen et al, 2004). In such failure condition, total stress strength

parameters obtained from the consolidated-undrained strength tests in terms of initial consolidation stress and undrained shear strength could be used. Undrained effective stress strength parameters could be used for some soils if the volumetric deformation and pore water pressure generation can predict during the failure, which is possible in the modern stability analysis model. Otherwise, effective strength parameters from the drained strength tests could be used.

2.4 STRENGTH PARAMETERS FOR SHALLOW SLOPE STABILITY ANALYSIS

For the shallow slope stability analysis, the strength parameters at low stress ranges are necessary. Several past studies have highlighted that the failure envelopes at the low effective stress range are significantly non-linear and the Mohr-Coulomb failure criterion does not represent such non-linearity (Maksimovic, 1989; Day, 1992; Mesri, 1993; Baker, 2004; Atkinson, 2007). Maksimovic (1989) reported examples of strength envelopes for the compacted London clay by using both the linear and non-linear strength criteria, as shown in **Figure 2.3.** The strength envelopes at a higher stress range of 150-300kPa fitted well with the linear strength criterion, whereas the envelope at a lower stress range of 5-25kPa showed significant degree of non-linearity, which was expressed by a power function. It is highlighted that the linear approximation from higher stress range greatly over-estimates the strength parameters and eventually the factor of safety.

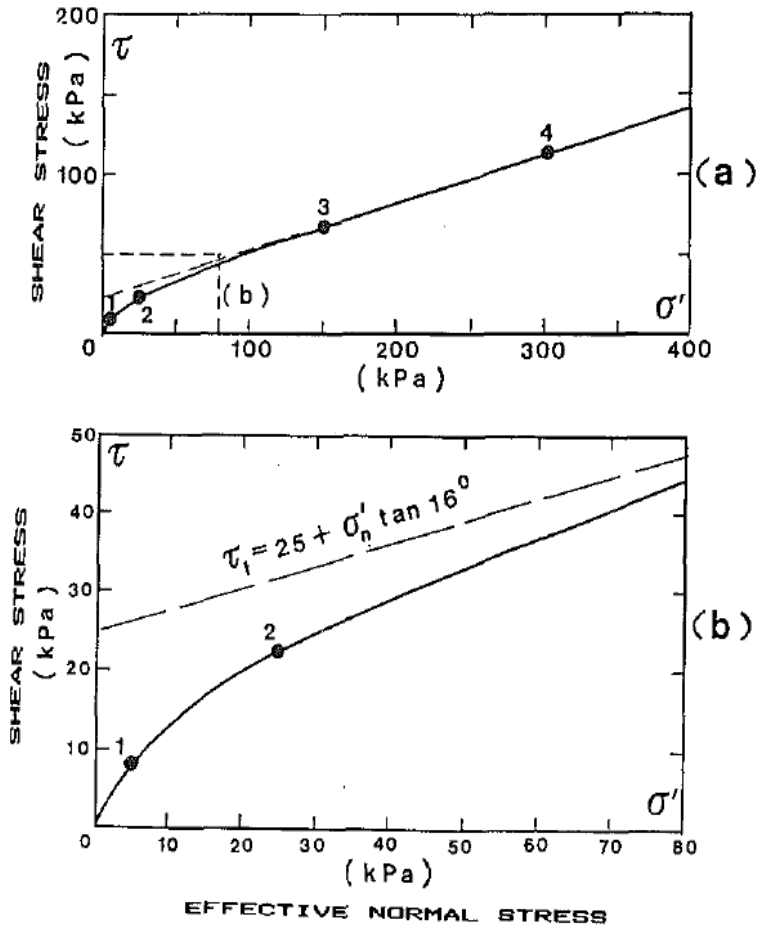

Figure 2.3. Non-linear failure envelope for compacted London clay (Maksimovic, 1989)

The early research conducted by Bishop et al. (1965) on undisturbed London clay by performing several consolidated-undrained triaxial tests at low effective confining stresses noted a marked curvature on the failure envelope. Day and Axten (1989) emphasized that the cohesion at low normal stresses was very small approaching zero for clay soil suggesting the curvature of the failure envelope. They concluded that, as the cohesion intercept decreased with reducing normal stress following the non-linear envelope, the factor of safety was therefore found to be strongly dependent on the normal stress range in which the shear strength parameters were derived. Furthermore, the shear strength parameters derived linearly

from the higher effective stress range and applied in the stability analysis model greatly over-estimate the factor of safety by more than 100% than that from the low stress range.

The research carried out by Atkinson (2007) on overconsolidated clays by performing several drained and undrained triaxial tests observed that the curvature of peak strength envelopes became significant at the overconsolidation ratio greater than four. The research highlighted that the Mohr-Coulomb failure criterion is potentially unsafe to represent the peak strength of overconsolidated clay, and the non-linear power-law failure criterion works satisfactorily at a low stress range or very high overconsolidation ratio. Parry (1968, 1970) investigated the failure of a river dyke constructed on a base of lightly overconsolidated clay during construction, by deriving undrained strength parameters from laboratory tests on such clay, demonstrated that even small degree of overconsolidation can have a pronounced effect on the stability in the field.

2.5 LINEAR AND NON-LINEAR STRENGTH CRITERIA

Various shear strength criteria have been in use to represent the shear strength of soil in a recent geotechnical practice. Among them, the Mohr-Coulomb failure criterion is a widely adopted linear failure criterion, which can be used for a wide variety of soils. As explained in the previous section, for the stability analysis of shallow slope failure, non-linear failure criteria are inevitable to derive the appropriate strength parameters at low stresses. The power-law failure criterion is a widely used non-linear failure criterion to represent the strength envelopes at low stress ranges, as reported by Atkinson (2007). In addition, several undrained strength expressions can also be found in the literatures to express the undrained strength relating with OCR, such as the expression proposed by Mitachi and Kitago (1976).

2.4.1 MOHR-COULOMB FAILURE CRITERION

Although it is very easy and can be found in the soil mechanics text books, the Mohr-Coulomb failure criterion is discussed briefly in terms of illustrating a controversial estimation of the apparent cohesion at a low stress range. It is simple to fit a straight line Mohr-Coulomb failure envelope to the curved envelope, but this has a disadvantage of over-predicting the apparent cohesion and hence the soil strength at low stress ranges, as mentioned earlier. For soils that have very small or zero inter-particle bonding, the failure envelope must pass through origin (τ=0 and σ'=0) and meet the critical state line, as shown in **Figure 2.4**. Using this criterion, the shear strength of soil can be expressed as follows:

$$\tau = c' + \sigma' tan\varphi' \qquad \text{Equation 2.1}$$

and for critical state strength, c'=0,

$$\tau = \sigma' tan\varphi'_{crit} \qquad \text{Equation 2.2}$$

where, c' is the effective apparent cohesion, φ' is the effective friction angle and φ'_{crit} is the effective critical friction angle. The effective stress strength parameters c' and φ' are strongly dependent on which stress range the strength envelopes are projected from the higher stress range, as shown in **Figure 2.4.**

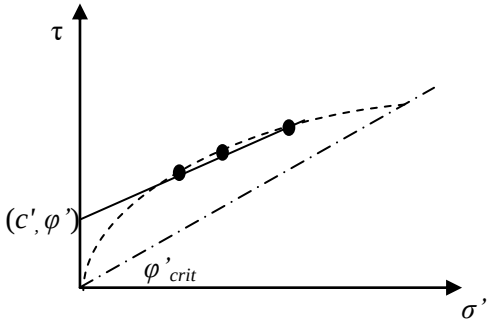

Figure 2.4. Illustration of linear Mohr-Coulomb strength envelope of curved failure envelope

2.4.2 POWER LAW FAILURE CRITERION (ATKINSON, 2007)

A non-linear power-law failure criterion can be used to represent the non-linear failure envelope at the low stress range (Atkinson, 2007; Charles, 1982; De melo, 1977). The non-linear strength envelope can be expressed in the form:

$$\tau = A\sigma'^{b} \qquad \text{Equation 2.3}$$

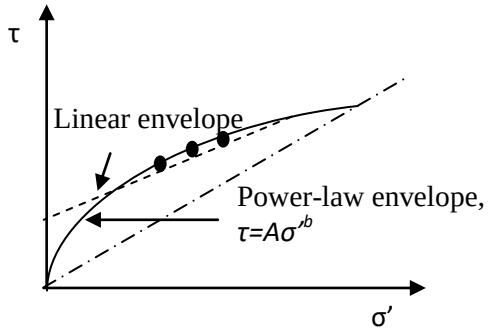

Figure 2.5. Illustration of power-law strength envelope of non-linear failure envelope

where, the parameters *A* and *b* are power-law strength parameters. In which, the parameter *b* gives the degree of non-linearity of failure envelope i.e. smaller the value of *b* greater the curvature and *b*=1 represents the linear failure envelope, as shown in **Figure 2.5**. The parameter *A* is equivalent to the friction coefficient.

2.4.3 UNDRAINED STRENGTH EXPRESSION (MITACHI & KITAGO, 1976)

Mitachi and Kitago (1976) proposed an expression to express the undrained strength of overconsolidated clays, in which the relationship between the ratio of undrained shear strength (τ) and vertical effective stress before shearing (σ'_0) and the overconsolidation ratio in a logarithmic plot is linear. The expression is in the form:

$$(\frac{\tau}{\sigma_0'})_{OC} = (\frac{\tau_1}{\sigma_p'})_{NC} OCR^{1-m} \qquad \text{Equation 2.4}$$

Where, $m = \frac{C_s}{C_c}$ in which C_s is the swelling index and C_c is the compression index; m depends on the soil and type of shear test. τ, τ_1, σ_0' and σ_p' are defined as shown in **Figure 2.6**.

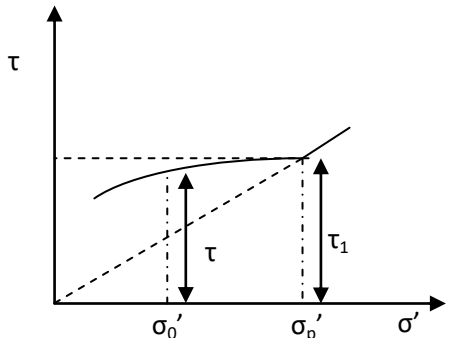

Figure 2.6. Illustration of variation of undrained shear strength with pre-shear vertical effective stress for saturated clay (basis of the expression)

2.6 STATE NORMALIZATION AND BOUNDARY SURFACES

The state boundary surface provides a boundary between the possible and impossible states and defines a locus of all the possible state of a soil element undergoing plastic deformation, which is constant for each specific volume and proportional to the equivalent stress on the normal compression line corresponding to that specific volume (Amorosi and Rampello, 2007; Atkinson and Bransby, 1977; Schofield and Wroth, 1968). The undrained effective

stress paths for normally consolidated and overconsolidated samples sheared at constant specific volume, and associated state boundary surfaces at the dry side of the critical and the wet side of the critical, are illustrated in **Figure 2.7**. If the samples shear at different specific volumes, the differences in specific volume can be scaled or normalized by the equivalent pressure; the failure states of the specimens form the state boundary surfaces. This normalization procedure was first adopted by Hvorslev (1937); and the state boundary surface at the dry side of the critical is termed as Hvorslev surface and at the wet side of the critical is termed as Roscoe-Rendulic surface.

Burland (1990 and 1996) used an intrinsic equivalent pressure (σ_{ve}*) as the normalizing pressure with respect to the intrinsic compression line to assess the effect of soil microstructure on the strength of natural clay by comparing the state boundary surfaces of intact and reconstituted clays, as shown in **Figure 2.8**. The reconstituted clay was prepared by mixing slurry of parent clay thoroughly at moisture content between 1 to 1.5 times the liquid limit and then compressed one-dimensionally in a consolidometer. The mechanical properties of such clay are termed as intrinsic properties since they are inherent to the parent material and are independent of its natural state. The intrinsic state boundary surface is usually taken as a reference surface to evaluate the influence of soil structure on the strength of natural clay, as illustrated in **Figure 2.8**.

Burland (1990) and Burland et al. (1996) highlighted that the difference between natural and intrinsic state boundary surfaces is due to the effect of soil structure. The study investigated four stiff clays in both natural and reconstituted states by performing several drained and undrained triaxial tests. The study reported that the intact strength is greater than the corresponding intrinsic strength due to the presence of natural microstructure enhancing the

strength of intact samples, as observed in the difference between intrinsic and intact state boundary surfaces.

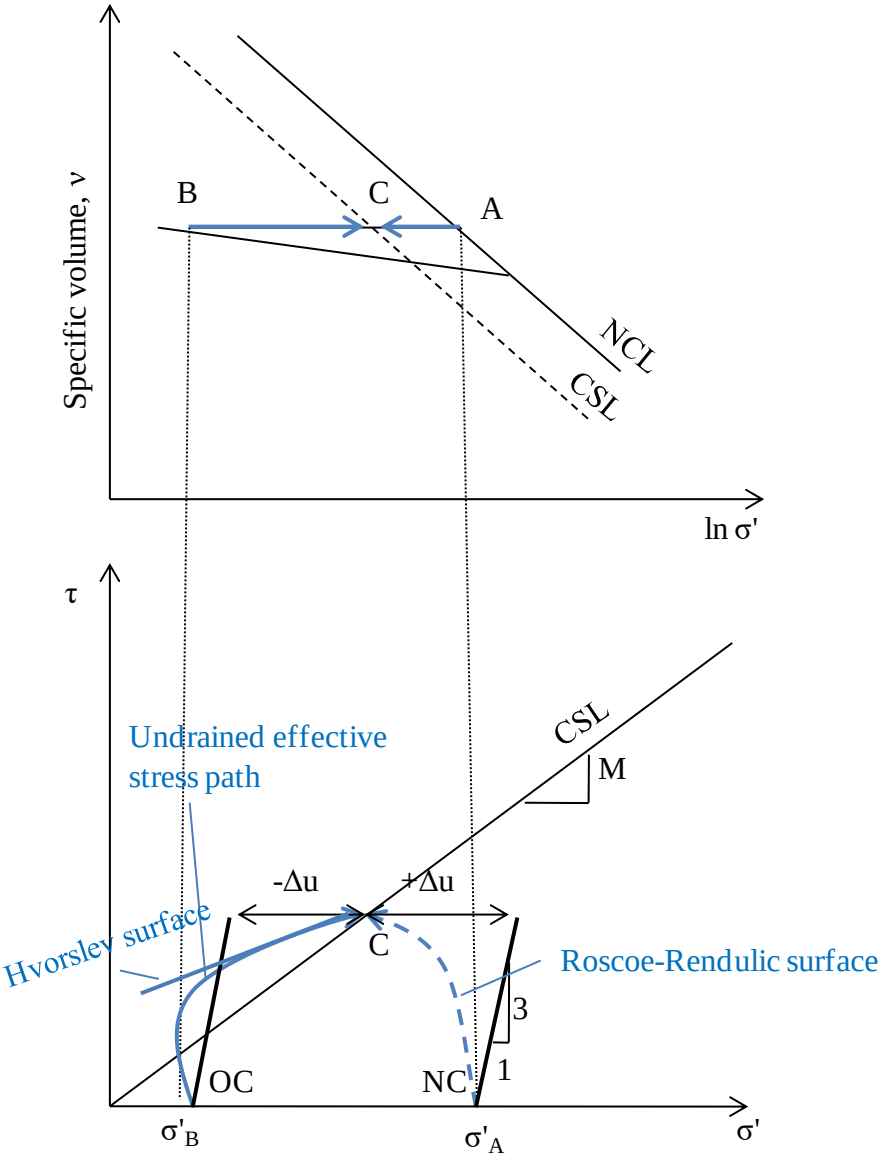

Figure 2.7. Undrained effective stress paths and state boundary surfaces for overconsolidated and normally consolidated samples

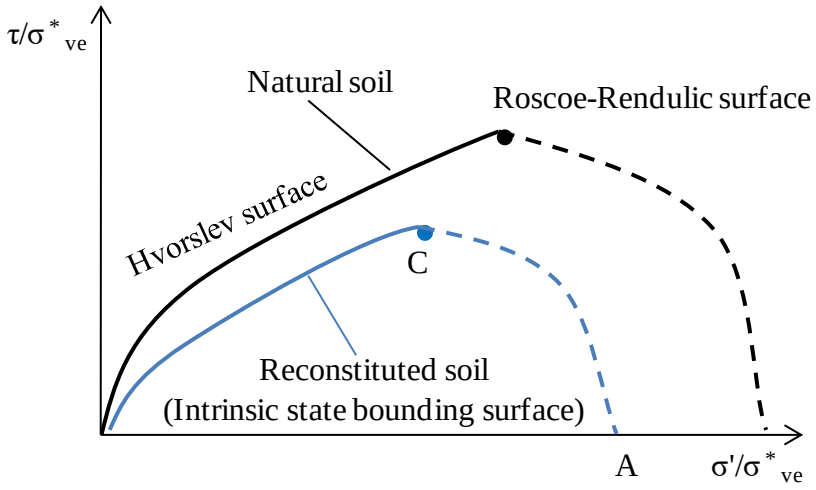

Figure 2.8. Comparison of natural and intrinsic state boundary surfaces after normalization with respect to intrinsic equivalent pressure

After the normalization with respect to the intrinsic equivalent pressure (σ_{ve}*), the Mohr-Coulomb and power-law strength envelopes can be expressed as:

$$\frac{\tau}{\sigma_{ve}^*} = c^* + \left(\frac{\sigma'}{\sigma_{ve}^*}\right) tan\varphi^* \qquad \text{Equation 2.5}$$

$$\frac{\tau}{\sigma_{ve}^*} = \alpha \left(\frac{\sigma'}{\sigma_{ve}^*}\right)^{\beta} \qquad or \quad \tau^* = \alpha\,(\sigma'^*)^{\beta} \qquad \text{Equation 2.6}$$

where, the parameter β represents the degree of curvature, and α is equivalent to the friction coefficient.

2.7 STRUCTURED SOIL AND ITS TRUE COHESION

There are several past researches which have highlighted the role of natural structure enhancing the strength of soils (e.g. Burland, 1990; Leroueil and Vaughan 1990; Cotecchia and Chandler, 2000). Abrahm et al. (2010) mentioned that the soil structure is as important as the void ratio and stress state in controlling the mechanical behaviour of natural and

compacted soils. The structure of soil includes the combination of fabric and bonding (Mitchell, 1976). Fabric is the arrangement of soil particles, while bonding is the inter-particle forces which are not of a purely frictional in nature. The inter-particle bonding in the soil develops after the construction of earth structures, probably due to physico-chemical processes including cycles of wetting and drying. This bonding can result in small tensile strength and true cohesion in the structured soil elements.

CHAPTER 3 LITERATURE REVIEW ON NEAR-SURFACE STRENGTH OF EMBANKMENT SLOPES

3.1 INTRODUCTION

In this chapter, a literature review is made to summarize a current understanding on the strength of near-surface soil and its variation in embankment slopes, which forms background information for the second part of this study. The strength of near-surface soil is considered to be changed after the construction of embankments in response to climatic variations. As the shallow slope failure triggers along the near-surface soil, it is important to understand the current strength of such soil with respect to its initial as-compacted strength to ensure the safety and serviceability of the embankments. Most of the embankments are constructed with compacted soils available locally around the construction sites. In this study, the studied embankments were constructed with the compacted locally available artificial mixture of alluvial clay and sand. The strength behavior of clay-sand mixed soils under a critical state framework is also reviewed in this chapter.

3.2 NEAR-SURFACE ZONE AND ITS FORMATION MECHANISM

The near-surface zone in embankment slopes develops with time after the construction of embankments primarily due to the effect of vegetation and shrink-swell cycle of soil in response to the climatic variation. The repeated cycles of shrink and swell of soil with time due to the climatic variations change the properties of soil in this zone from its initial as-compacted states. As a result, the permeability of soil enhances so that the hydraulic and mechanical responses react sharply with climatic events. The study conducted by Glendening et al. (2014) reported that the permeability of soil changed up to four orders of magnitude within 0-1.4m depth in the aged embankment slope, and the soil in this depth showed the most significant variations in pore water pressure. The transient nature of such permeability

and pore water pressure can lead to significant variation in shear strength of soil in the near-surface zone with time. However, the science underpinning the development of the near-surface zone and the variation in soil strength with time are yet to be clearly understood.

3.3 STRENGTH DETERIORATION IN NEAR-SURFACE ZONE

The strength of soil in the near-surface zone can be reduced over time due to the transient nature of pore water pressures and permeability. The actual process involves in deteriorating the strength of soil in the near-surface zone is yet to be well understood. It is believed that a weather-driven process, which includes desiccation of the near-surface soil and the subsequent development of volume shrinkage and cracking during drying period, can be the major governing process for such deterioration (Stirling et al., 2017). After the drying period, the desiccated soil receives swelling during rain-water infiltration and the subsequent strength softening. Prolonged drying and a greater number of short-duration and high-intensity rainfall events due to the global climate change, which are likely to cause increased run-off and crack infiltration, may exacerbate the climate-driven deterioration process and hence attract the interest of researchers. The more familiar topic found in the literature explaining this strength deterioration process is termed as 'weathering' in the near-surface soil as a result of climatic variations (Mandaglio et al., 2016).

The desiccation, a widely observed phenomenon on the embankments, is usually accompanied by the change in volume of the surface soil due to drying. As a result of desiccation in the surface soil, overconsolidation occurs at shallow depths (Mitchell and Soga, 2005). Stirling et al., (2017) mentioned that a desiccated crust, which is characterised by the highly negative pore water pressure and extremely low permeability, can develop as a result of desiccation in the near-surface zone. Allam and Sridharan (1981) reported that as a result of desiccation cracks and subsequent enhanced infiltration can move finer soil particles in the

direction of rain-water infiltration. Consequently, the enhanced permeability and the desiccated crust at a shallow depth in the near-surface zone during precipitation events can rapidly develop a perched water table, elevate pore water pressure, and reduce the shear strength leading to the shallow slope failure.

The perched water table and the subsequent development of positive pore water pressure in the near-surface zone can be the main cause of the rainfall-induced landslide or shallow slope failure. In the past research, the in-situ measurement conducted by Ng et al., (2003) on an un-saturated expansive slope found that the perched water table was developed at a depth of about 1.5m below the ground surface indicating a dense soil layer without open cracks. Similarly, a long-term field monitoring experiment conducted by Springman et al. (2014) on a slope with shallow weathered soils overlying sandstone bedrock observed the development of perched water table due to the enhanced permeability in the shallow soil layers. They mentioned that the formation of perched water table, including artesian pressure, could cause the instability along the interface between two layers.

The photographs in **Figure 3.1** show an example of shallow slope failure in Kushiro River dyke due to heavy rainfall observed over wide areas of Hokkaido in August 2016 (from the final investigation report by the Japanese Geotechnical Society Hokkaido Branch). The mechanism supposedly involved accumulation of infiltrated water to the toe and reduced effective stress as well as increased soil weight.

Figure 3.1. Photographs showing shallow slope failure in Kushiro River dyke due to heavy rainfall in August 2016 (Source: Final investigation report by the Japanese Geotechnical Society Hokkaido Branch)

3.4 CLIMATE CHANGE AND ITS IMPACT ON SHALLOW SLOPE INSTABILITY

It is predicted that the climate is changing significantly over this century. As a result of the climate change, the slopes may experience changes in precipitation pattern including extreme events, higher temperature and changes in sea level (Dijkstra and Dixon, 2010; Glendinning

et al., 2008). The climate interacts with natural and constructed slopes and their associated vegetation through the surface leading to significant change in pore water pressure and shear strength with time, as mentioned earlier. Therefore the significant impact could be on the shallow slope instability owing to the rapidly increasing positive pore water pressure in the context of likelihood of prolong hotter drier summer followed by more intense periods of precipitation. Dijkstra and Dixon (2010) reported the potentially adverse impacts of climate change on the stability of natural and constructed slopes focusing on quantifying the effects of climate change on pore water pressure responses and the resultant rate of deformation. They argued that the slope stability forecasting simulation model always suffer from poor parameter specification generally owing to the results of limited measurement of spatio-temporal variations in model parameters.

3.5 HYDRO-MECHANICAL BEHAVIOUR OF COMPACTED SOIL

In early studies, microstructure of soil is recognized as a key feature in explaining the behavior of compacted soil, in which the soil compacted wetter than optimum showed dispersed microstructure, while flocculated microstructure was observed in the soil compacted drier than optimum (Lambe, 1958; Lambe and Whitman, 1969). The studies conducted later have interpreted this feature differently in the clay soil compacted drier than optimum by means of scanning electron microscopy and mercury intrusion porosimetry, in which the aggregated structure that behaved as larger particles were observed (Shridharan et. al, 1971). Cuisinier and Laloui (2004) conducted a study to investigate the link between fabric and hydro-mechanical behavior of compacted silt in both saturated and unsaturated states by performing suction controlled oedometer tests and mercury intrusion porosimetry. The initial fabric of compacted samples consisted of macro- and micro-pores, which was strongly affected by suction and vertical effective stress change in unsaturated and saturated

samples, respectively. The study concluded that the hydro-mechanical behavior of compacted soil is directly related to its fabric. Moreover, after receiving the seasonal cycles (drying and wetting), the fabric of the compacted soil in the near-surface zone changes significantly with time leading to the degradation in soil strength (Mandaglio et al., 2016). It is therefore important to note that the strength behavior of compacted fine-grained soils is strongly dependent on the fabric based on the compaction water content whether it is drier than optimum or wetter than optimum.

3.6 COMPACTION VS OVERCONSOLIDATION

The stress-strain behavior and stress paths during shearing of compacted samples and overconsolidated samples at the same void ratio are different due to different fabrics (Coop, 1990). The research was carried out by performing undrained triaxial compression tests on compacted and overconsolidated samples of carbonate sand specimens, which were prepared at the same initial void ratio for a given initial isotropic confining pressure, as shown in **Figure. 3.2**. The undrained stress path for the overconsolidated sample was initially stiffer than the compacted sample. This difference can be explained by the different soil fabrics developed by different stress paths and degrees of particle crushing prior to shearing. Therefore, overconsolidation and compaction, even at the same initial void ratio and confining pressure, cannot be treated equally as both the materials exhibit different mechanical properties. However, both samples showed similar strength at large deformations owing to the destruction of initial fabrics.

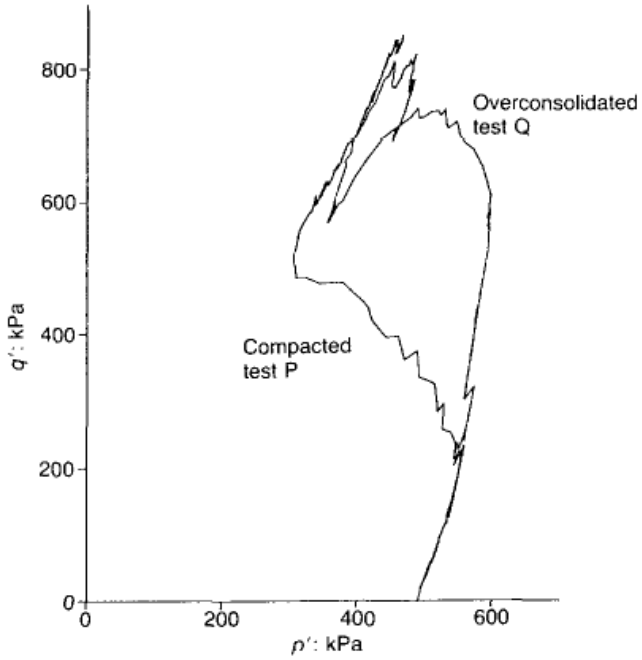

Figure 3.2. Comparison of strength behavior between compacted and overconsolidated samples of carbonate sand (Coop, 1990)

3.7 COMPACTION OF EMBANKMENTS AND STRESS-STRAIN BEHAVIOUR OF COMPACTED SOIL

The compaction of embankments requires accurate compaction control to achieve desired mechanical properties of soil such as strength and stiffness, and hydraulic conductivities. The mechanical properties of compacted soils are strongly dependent on the compaction method, compaction energy and initial compaction water contents. For the particular compaction energy, the dry density can be achieved higher closer to the optimum water content, but adopting the compaction water content too drier and wetter than optimum need careful consideration with respect to the climatic events. At the same density, adopting the compaction water content too dry may create a problem of collapse of the soil strength during precipitation events, whereas adopting too wet may create a problem of excessive volume shrinkage and cracking during drying period, which can eventually lead to deterioration of the embankment surface. However, in a large earthwork project, it is very difficult to

accurately estimate the field compaction energy and actual soil type, and so as to evaluate the actual values of maximum dry density and optimum water content in the field.

In the previous study, Tatsuoka (2011) presented the strength and pre-failure stiffness behavior of compacted soil in relation with field compaction control and design values of strength and stiffness by performing a series of drained triaxial compression tests and plane strain compression tests on a wide variety of sandy and gravelly soil sampled from the embankment construction site. The paper reported that the degree of compaction is an easy term to be used in the field compaction control and design practice, and to correlate with the strength and stiffness of compacted fill, rather than a widely used term in the geotechnical investigation, the relative density. The degree of compaction is defined as 'the ratio of in situ dry density to maximum dry density from the laboratory compaction tests'. The study reported that the peak strength increased significantly as the degree of compaction increased beyond the allowable lower limit used in field compaction control. Under a saturated condition, the drained strength and stiffness increased with an increase in degree of compaction. Miura et al. (2011) conducted a laboratory study on investigating the effects of dry density as well as the degree of compaction on stress deformation characteristics of silty sand over a wide strain range by performing a series of triaxial compression tests under saturated undrained conditions. The results showed that the stress-strain relationship and its non-linearity were strongly affected by the degree of compaction and confining pressure, and the undrained shear strength as well as the shear strength ratio increased significantly with the increasing degree of compaction.

3.8 CRITICAL STATE FRAMEWORK FOR STATE NORMALIZATION

To understand the strength behavior of soil samples sheared with different specific volumes and OCR under the critical state framework, the difference in specific volume and OCR can

be normalized by the critical equivalent pressure (p'_c) on the critical state line with respect to that specific volume. In a normalized scale, after plotting the stress paths of samples consolidated with different effective stresses, their peak strength fall close to a unique peak strength envelope, which is known as the Hvorslev surface on the dry side of the critical, as explained in Chapter 2.

The critical state line in a *q*-*p'* space can be expressed as:

$$q = Mp' \qquad \text{Equation 3.1}$$

where, $q = \frac{(\sigma'_1 - \sigma'_3)}{2}$, $p' = \frac{(\sigma'_1 + 2\sigma'_3)}{3}$ and *M* is the gradient of critical state line.

For triaxial compression:

$$M = \frac{6sin\emptyset'_{crit}}{3 - sin\emptyset'_{crit}} \qquad \text{Equation 3.2}$$

For triaxial extension:

$$M = \frac{6sin\emptyset'_{crit}}{3 + sin\emptyset'_{crit}} \qquad \text{Equation 3.3}$$

where, $\emptyset'_{crit}$ is the critical state friction angle.

In a *v*-ln*p'* space:

$$v = v_\Gamma - \lambda \, lnp' \qquad \text{Equation 3.4}$$

v_Γ=the specific volume intercept at unit pressure (*p'*=1 kPa), λ= compression index.

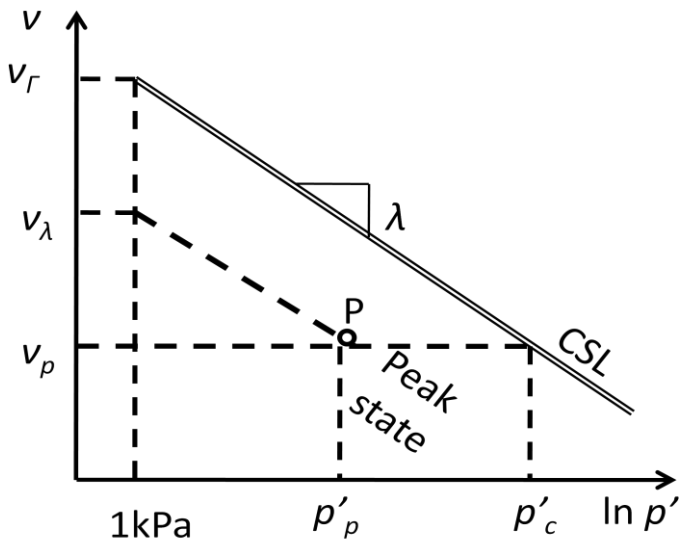

Figure 3.3. State diagram and definition of variables for critical state normalization

As the shallow slope failure requires the strength parameters at low effective stresses, as explained in Chapter 2, the peak strength envelope in the *q-p'* space can be expressed by the power law function:

$$q = mp'^{n} \qquad \text{Equation 3.5}$$

where, *m* and *n* are peak strength parameters. The parameter *m* is similar to the friction coefficient and the parameter *n* represents the degree of non-linearity of the failure envelope.

Applying the critical state normalization procedure, the mean effective stress (*p'*) is normalized with respect to critical equivalent pressure (p_c') and the deviatoric stress is normalized with respect to Mp_c'. In which, p_c' is calculated based on the specific volume before undrained shearing on the critical state line, as shown in **Figure 3.3**.

The normalized peak strength envelope can be written as:

$$\frac{q}{Mp'_c} = \mu\left(\frac{p'}{p'_c}\right)^{\eta} \qquad \text{Equation 3.6}$$

The normalized peak strength envelope meets the critical state at p'/p_c'=1.0 and q/Mp_c'=1; and hence, μ=1.

3.9 TRANSITIONAL SOIL AND ITS STRENGTH BEHAVIOUR

Transitional soils are soils with grading intermediate to clays and sands, in which the initial soil density or specific volume plays a major role in its compression as well as shearing behavior to large strains, so that it is difficult to obtain a unique normal compression lines as well as critical state lines by performing a conventional laboratory test (Coop, 2015; Shipton and Coop, 2012; Xu and Coop, 2016). For such soils, it is difficult to identify the effect of soil structure on the strength behavior due to non-unique intrinsic behavior as they have non-unique normal compression lines and critical state lines, in contrast to clays, but the critical state framework can be applicable by assuming separate critical state lines based on initial specific volumes. Xu and Coop (2016) carried out an experimental study to examine the potential transitional behavior in loess by performing a series of carefully controlled oedometer tests and triaxial tests on intact and reconstituted samples. The study highlighted the features of transitional behavior in both intact and reconstituted loess by investigating the influence of initial density on normal compression lines and critical state lines. They eventually noted the difficulty in identifying the effect of soil structure on the strength behavior by comparing the state bounding surface between the intact and the reconstituted soils due to non-unique intrinsic behavior.

Ferreira and Bica (2006) investigated the residual soil of Botucatu Sandstone in its natural and compacted states by performing a series of isotropic and one-dimensional compression tests, and drained and undrained triaxial tests. The study reported that the behavior of natural samples conformed well to the critical state soil mechanics framework with a unique normal compression line and critical state line. The behavior of compacted samples indicated the

transitional mode with non-unique both normal compression lines and critical state lines, which were dependent on the initial void ratios. They reported that the critical state framework can be applied to transitional soils by using a family of parallel critical state lines depending on the initial specific volumes, but they found a difficulty in quantifying the effect of soil structure on the strength behavior due to non-unique intrinsic properties.

3.10 IN-SITU STRENGTH TESTING AND FIELD MONITORING IN SHALLOW VEGETATED SLOPES

To determine the in-situ strength of near-surface soil varying spatially and temporally along the slope, a long-term in situ strength testing, such as cone penetration tests, in association with field monitoring is required. The portable cone penetrometer test is simple to perform in a shallow vegetated slope in terms of installation of apparatus in comparison to presently available general cone penetration (Athapaththu et al., 2015).

To understand the variation of in-situ strength relating with the shear strength parameters, the in-situ strength, such as cone penetration resistance, can be correlated with the shear strength of the same material. In a clayey soil, the cone penetration involves essentially undrained soil deformation, and hence its tip resistance is strongly governed by the undrained shear strength. A reasonable correlation between the cone penetration resistance and the corresponding undrained strength can therefore be achieved by performing the in-situ undrained strength tests, such as vane shear tests, at locations close to the cone penetration path or the laboratory undrained strength tests on undisturbed samples taken from the same location. However, both are considered practically challenging tasks either to perform the in-situ undrained strength tests or to obtain the undisturbed samples at different depths along the shallow vegetated slope repeatedly with time. To overcome such practical inadequacies, laboratory-controlled cone penetration tests in a calibration chamber on similar soils having densities closer to the

field compaction can be performed, although it is common for coarse sands (Pournaghiazar, et al., 2013; Yang and Russel, 2015). The comparison of correlations between the penetration resistance obtained in the field and laboratory and the laboratory undrained strength can be made to interpret strength variations in the field.

CHAPTER 4 FUNDAMENTAL INVESTIGATION ON FINE-GRAINED SOIL STRENGTH AT LOW STRESSES: MATERIALS AND METHODS

4.1 INTRODUCTION

This chapter describes the materials and methods employed in the first part of this study. The selection of suitable materials that typify the embankment slopes in the author's locality was one of the crucial steps in this research project. At the time of this research, many river dykes were being constructed with compacted clay-sand mixed soils. One of the materials was therefore decided to be extracted from the river dyke construction site in Maizuru as representative of locally available embankment soils. In addition, two natural clays were selected, which had different origins, ages and stress histories, to make this study complete and extending the scope to natural slopes.

On the other hand, the selection of suitable laboratory methods to measure the shear strength of fine-grained soils reflecting the failure mechanism relevant to the shallow slope instability problem was another important step in this research. Some field evidence and previous research were taken into consideration to choose relevant experimental methods. Consequently, the constant-volume direct shear test supplemented by hollow cylinder simple shear test, among the available methods in the author's laboratory, was found to be appropriate in this study.

4.2 MATERIALS

4.2.1 SELECTION OF MATERIALS

Since the main objective of this research has been to investigate the undrained strength behaviour of fine-grained soils with particular reference to shallow slope failure in

embankment slopes, the fine-grained soils such as a clay-sand mixed soil sampled from the river dyke construction site and two natural clays were investigated. These three soils were chosen as they represent very different soil characteristics and geotechnical settings, in which the two natural clays represent both aged and young natural outcrops and the clay-sand mixed soil represents the man-made geostructures with artificial gradation characteristics.

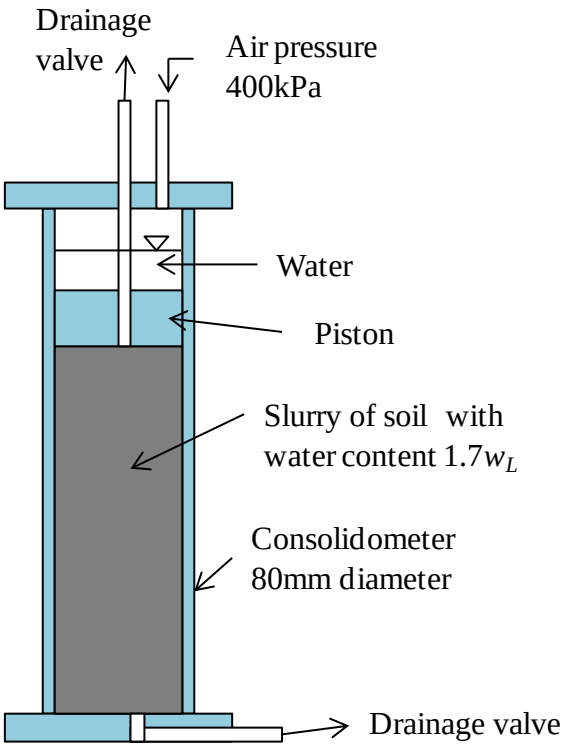

Figure 4.1. Preparation of reconstituted samples in a laboratory consolidometer

All the soils were tested in different states such as natural, reconstituted, and compacted. Reconstituted samples were prepared in a laboratory consolidometer from slurry of water content of about 1.7 times the liquid limit by initial one-dimensional consolidation to an effective vertical stress of about 400kPa, as shown in **Figure 4.1.** This stress was chosen to attain sufficiently overconsolidated states at low stresses in shear tests. Although the clay-sand mixed soil contained non-uniform soil particles, the reconstituted samples were prepared

without obvious segregation or inhomogenisation, as observed in X-ray micro CT images, which will present in a later section. The compacted samples were prepared in a standard proctor mould by compacting with the standard compaction energy (598kJ/m^3) in five different layers in which each layer received 16 numbers of blows. Each layer gave a direct shear specimen with little inter-specimen variability. The water content adopted in the field compaction for the clay-sand mixed soil was slightly wet of optimum, close to 1.15w_{opt}; therefore the compacted specimens of all the soils were prepared at the wet of optimum, with the initial compaction water content of 1.15w_{opt}. This compaction condition eventually led to well-compacted state, with the degree of compaction of about 95%, and the degree of saturation (S_r) of about 90%. The compacted state was of main interest in this study.

4.2.2 PHYSICAL PROPERTIES OF TESTED SOILS

The physical properties of the tested soils were determined by performing different laboratory tests following testing standards published by the Japanese Geotechnical Society. Among them, pyconometer tests for specific gravity (JGS 0111), standard proctor tests for compaction properties (JGS 0711), gradation tests (both Sieve and Hydrometer tests) for grain size distribution (JGS 0131), Atterberg limit tests for liquid and plastic limits (JGS 0141), and CRS oedometer tests for compression properties (JGS 0412) were performed. The standard proctor compaction curves and gradation curves for Izumi clay, Atsuma clay and clay-sand mixed soil are presented in **Figures 4.2** and **4.3**. Although Izumi clay is slightly more uniform than Atsuma clay, the two gradations are comparable. This clay-sand mixed soil has non-uniform gradation ranging from finer clay to coarser gravel particles. The physical properties are listed in **Table 4.1**.

Izumi clay

Izumi clay is a heavily overconsolidated Pleistocene clay (σ_{vy}'=1690kPa) with medium plasticity, which was block-sampled from an onshore excavation site in Izumi city, Japan. The sampling depth was 2 m, and the clay was estimated to have experienced a maximum 90-m burial in the past which made it heavily overconsolidated and slightly fissured (Nishimura, 2014).

Atsuma clay

Atsuma clay is a soft normally consolidated Holocene clay (σ_{vy}'=96kPa) with high-plasticity, which was sampled undisturbed at a depth of about 10.01-10.61m below ground level by using a pushed thin wall tube sampler in Atuma town, Japan.

Clay-sand mixed soil

The clay-sand mixed soil is an on-site artificial mixture of clay and sand sampled from a river dyke construction site in Maizuru along a floodplain of Chitose river, Naganuma Town, Japan. In this soil, a locally available high-plasticity alluvial clay was mixed with a volcanic sand excavated at another flood control site to reduce the overall water content and make it a suitable material for the dyke construction.

Table 4.1. Summary of physical properties of Izumi clay, Atsuma clay and clay-sand mixed (C-S) soil

Name of soils	w_n (%)	w_P (%)[(1)]	w_L (%)[(1)]	Clay fraction (%)[(2)]	Sand / Gravel (%)	G_s	σ_{vy}' (kPa)[(3)]	γ_d (kN/m^3)[(4)]
Izumi	34.8	28	54	25/36	0/0	2.714	1690	15.51
Atsuma	39.7	22	58	4/12	0/0	2.701	96	15.79
Maizuru C-S	27.4	30	49	22/30	39/7	2.711	-	14.69

[(1)] Measured for constituents passing through a 425 micron sieve, [(2)] (Finer than 2μm)/(Finer than 5μm), [(3)] Effective vertical yield stress [(4)] Izumi, Atsuma and C-S soil in compacted state before tests

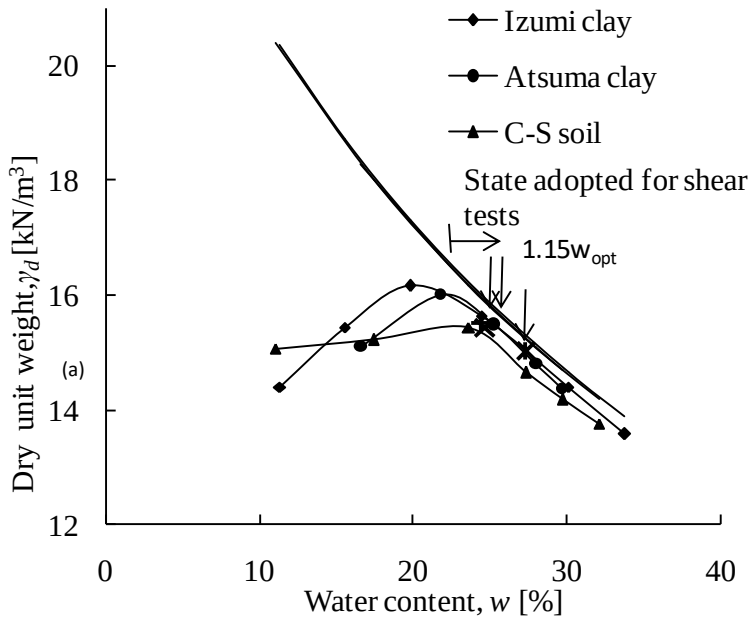

Figure 4.2. Standard proctor compaction curves for tested soils

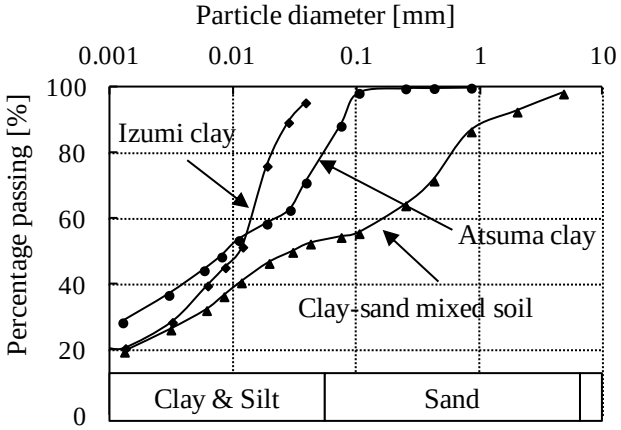

Figure 4.3. Grain size distribution curves for tested soils

4.3 METHODS

Establishing the state bounding surfaces and deriving the appropriate strength parameters of fine-grained soils having different structures corresponding to the failure mechanism of the shallow slope failure are one of the main sub-topics in this research. To achieve this objective, the constant-volume direct shear tests supplemented by hollow cylinder simple shear tests

were found to be relevant methods. Nevertheless, the investigation was also carried out by performing consolidated-undrained triaxial tests in order to understand the strength characteristics of soils in the near-surface zone of the Maizuru river dyke five years after the field compaction.

4.3.1 CONSTANT-VOLUME DIRECT SHEAR TEST

The direct shear test is a conventional shear test which can be performed under constant-pressure and constant-volume conditions in the laboratory. In the constant-volume direct shear test, height of a specimen is maintained constant during shearing and the evolution of vertical stress under slow shearing gives the effective vertical stress, equivalent to the saturated undrained shearing in triaxial tests. The undrained effective stress path of horizontal shear stress and vertical effective stress during shearing is measured.

In the constant-volume direct shear test, it is also conventionally assumed that the shearing in between two shear boxes is localised, but can form a nominal simple shear deformation before reaching a peak state during shearing. Such failure can be assumed to be relevant to the shallow slope failure, in which the critical slip surface is often envisaged to be parallel to the slope surface, and localized failure usually occurs along such a pre-defined shallow surface due to the rise in pore water pressure during heavy or incessant rainfall events.

4.3.2 MERITS AND DEMERITS OF DIRECT SHEAR TEST OVER TRIAXIAL TEST

In the direct shear test, shearing is carried out by applying the force directly to a K_0 consolidated soil sample in a horizontal plane, unlike in the triaxial test in which the difference in applied principal stresses develops the shear and it is not generally possible to control the direction of localized shear and to measure accurately the stresses along it. The

direct application of force along the failure plane under the constant-volume shearing condition in the direct shear apparatus can be considered as more relevant to the shallow slope failure, due to its failure surface pre-defined and parallel to the slope surface, over the triaxial shearing, as explained earlier.

Although the direct application of shear stress closely resembles the in-situ shearing of shallow slope failure, the direct shearing in particular is known to suffer from a problem of non-uniformities of stresses and strains during shearing (Roscoe, 1953; Saada and Townsend, 1981). This could be as a result of rigid boundaries, which are used to confine a specimen. On the other hand, the concentrations of stress at the front and rear edges of lower and upper shear boxes facilitate progressive failure along the plane of shearing; the full shearing strength of the specimen might not be mobilised simultaneously across it. Potts et al., (1987) also showed the stress and strain non-uniformities in the specimen of direct shear by plotting contours numerically, as shown in **Figure 4.4**. They demonstrated that the interpreted behaviour is representative of that in ideal simple shear.

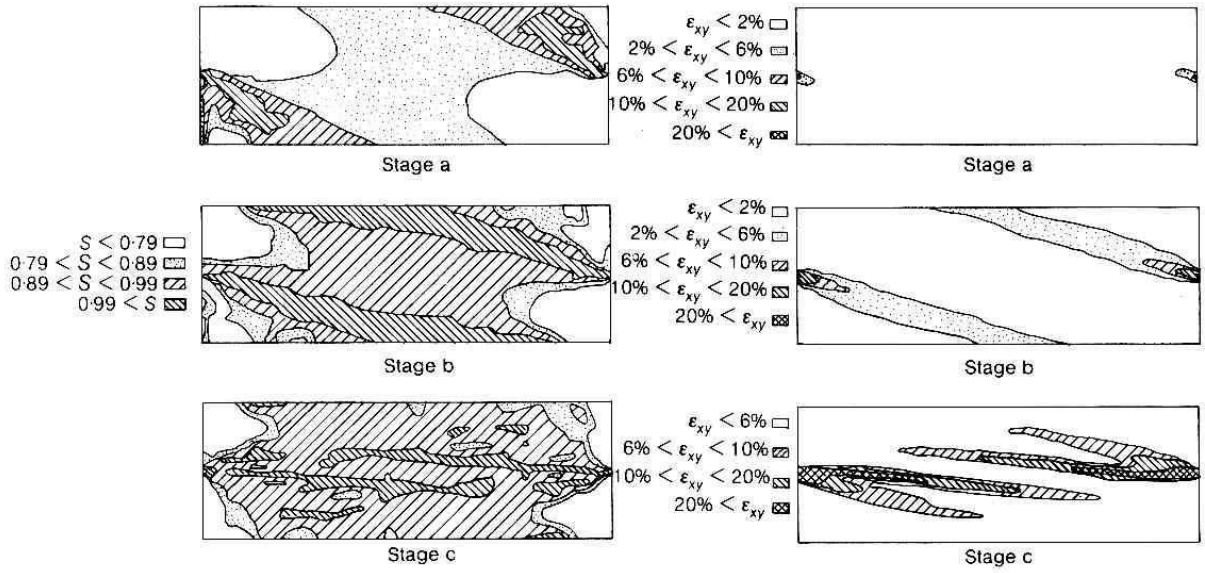

Figure 4.4. Stress and strain non-uniformities in direct shear test simulated by numerical analysis (Potts et al., 1987)

4.3.3 HOLLOW CYLINDER SIMPLE SHEAR TEST

In order to overcome the limitation of stress and strain non-uniformities in the specimen of direct shear tests and observe the true simple shear behaviour, supplementary more advanced simple shear tests, such as hollow cylinder simple shear tests, by applying the similar stress and strain boundary conditions, can be performed. In the hollow cylinder simple shear test, four sets of stress and strain (three linear directions and a radial direction) can be measured, in contrary to other simple shear tests. The detail description of this test can be found in (Nishimura, 2008). The illustration of stress and strain states in both the constant-volume direct shear and hollow cylinder simple shear are shown in **Figure 4.5**.

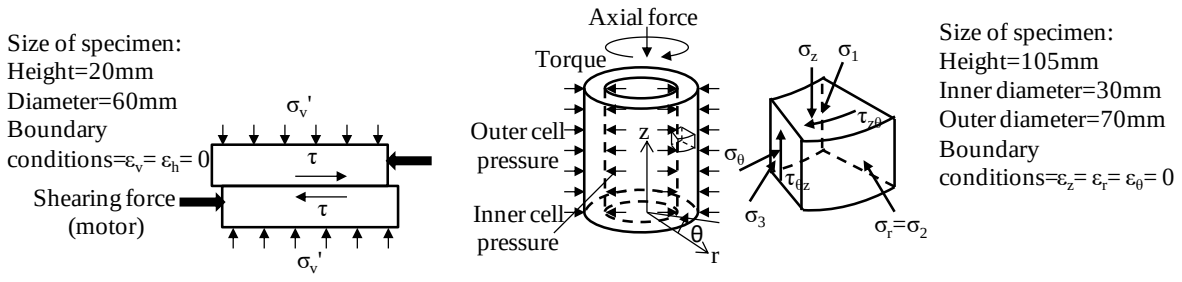

(a) (b)

Figure 4.5. Test specimens and stress states (a) Direct shear test (b) Hollow cylinder simple shear test

4.3.4 ADVANTAGES OF HOLLOW CYLINDER TEST

The hollow cylinder simple shear test is a more advanced simple shear test than the other conventional simple shear tests. One of the major advantages of this test is to reduce the stress and strain non-uniformities along the shear plane during shearing. The apparatus allows measuring three normal effective stresses and torsional shear stress during simple shearing,

which enable constructing evolution of Mohr's stress circles in the σ_1:σ_3 plane at any moment (e.g. Hight et al., 1983; Nishimura et al., 2007).

Therefore, with the help of these tests, it can be quantitatively analyzed that how the strength mobilized on three different planes when applying the boundary conditions (i.e. no normal strains in each direction) similar to those in the direct shear tests, as shown in **Figure 4.5**. Another important advantage of this test over the conventional simple shear test is a grid drawn on an outer membrane of the specimen can be used to observe a progressive development of the simple shear deformation by taking photographs.

4.4 EXPERIMENTAL PROCEDURES

4.4.1 CONSTANT-VOLUME DIRECT SHEAR TEST

In this section, the direct shear apparatus and the experimental procedures adopted to perform constant-volume direct shear tests are described. The direct shear apparatus employed in this research is illustrated schematically in **Figure 4.6**. This apparatus is a fully automated PC-controlled apparatus capable of performing tests in both constant-volume and constant-pressure conditions. The apparatus comprised of a bellofram cylinder for vertical loading and a direct-drive motor for horizontal shearing. To achieve a constant-volume condition during shearing, the loading ram was mechanically clamped with two clamping screws, as shown in **Figure 4.6**. The horizontal shearing rate on the motor was controlled automatically with the PC. The vertical and horizontal stresses during shearing were measured with high precision load sensors, while the vertical displacement was measured with a displacement sensor.

The calibrations of all the sensors were made at the beginning of a test series. To confirm the sensors' readings and the experimental procedures, few trial tests were performed.

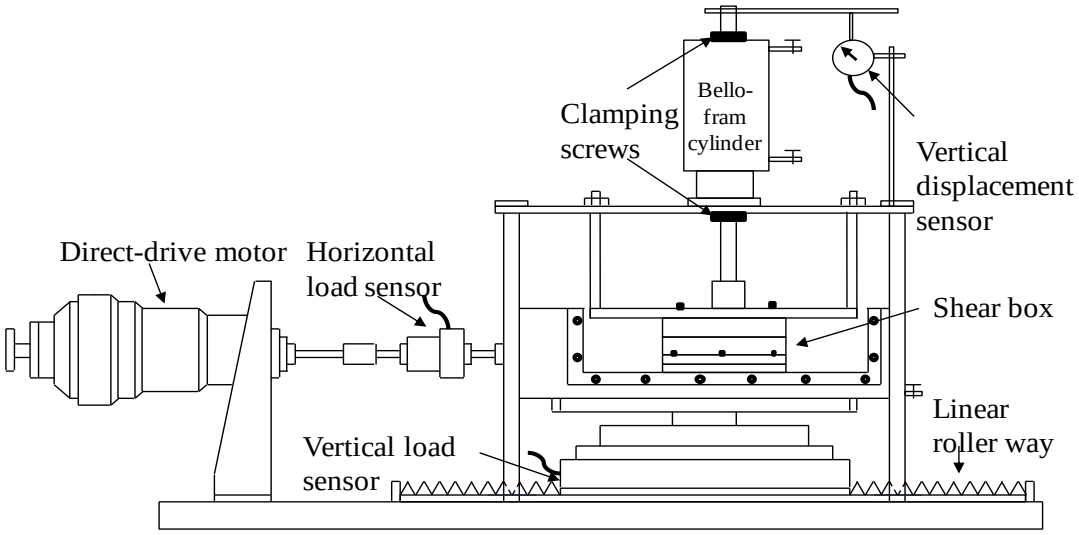

Figure 4.6. Schematic diagram of direct shear apparatus employed in this study

Sample Preparation

After removing the wax layer and cling film of a large cylindrical sample, the direct shear sample was trimmed with a sampling ring in a soil lathe. The size of the specimen was 20mm high and 60mm in diameter, same as the dimension of the sampling ring. In the meantime, the water content and the weight of the specimen were also measured. The trimmed sample was then wrapped in a cling film to prevent the loss of moisture content and transferred to the apparatus.

Experimental set up

The partial experimental set up was carried out before the specimen preparation to prevent moisture loss of the specimen, as shown in **Figure 4.7 (a)**. Initially, the lower shear box with a porous disc was attached with four screws. The porous disc together with drainage channels was then saturated with water and a wet filter paper was placed on it. The upper shear box was then attached to the lower shear box with two long screws. After fixing both the shear boxes, the sample was transferred into the box by using a sample extruder. The wet filter paper was then placed on the top of the specimen. The horizontal loading arm was then connected carefully with the driving motor monitoring with sensors' reading on the PC.

Finally, the upper shear box was connected vertically with three long screws to make a rigid connection with a vertical frame.

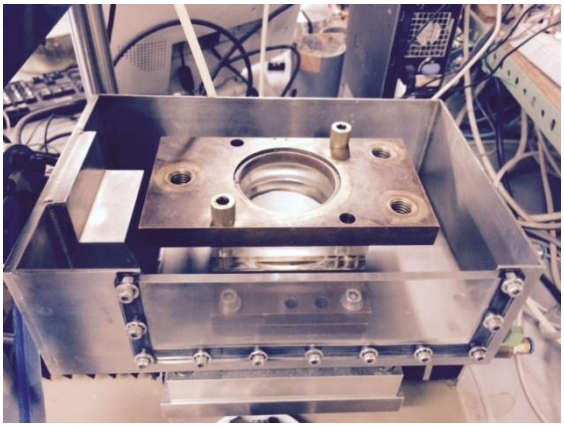

(a)

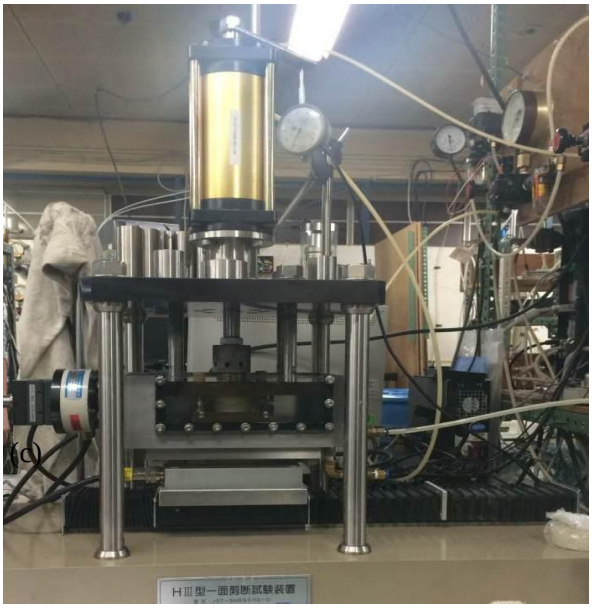

(b)

Figure 4.7. Constant-volume direct shear test (a) Initial preparation of shear box (b) Shear box with specimen before consolidation stage

In order to perform the tests under a near-saturated condition with zero suction, i.e. field saturated condition, the shear box was fully submerged with water before shear loading. The axial loading ram was touched to the specimen top through the double acting bellofram

cylinder. In the meantime, a vertical displacement transducer was attached to the axial loading ram to measure the axial displacement of the specimen, as shown in **Figure 4.7 (b)**.

Consolidation stage

After the specimen set up, the vertical consolidation pressure was applied to the specimen at a rate of 2kPa/min through the double acting bellofram cylinder. The pre-consolidated samples were first consolidated to the same vertical stress as in the pre-consolidation in the consolidometer and then swelled back to desired vertical consolidation pressure before shearing. After applying the desired vertical consolidation pressure, the consolidation of the specimen was allowed for at least 24 hrs.

Shearing stage

After the consolidation stage, the upper and lower shear boxes were released by removing two long screws and the upper shear box was then lifted vertically to maintain a clearance between two boxes of about 0.1mm vertically. In the meantime, the axial ram of the bellofram cylinder was clamped mechanically with two clamping screws so that it maintained a constant-volume condition throughout the shearing process. The horizontal shearing of the specimen was then carried out at a horizontal displacement rate of 0.01mm/min until reaching a maximum displacement of 6mm.

4.4.2 HOLLOW CYLINDER SIMPLE SHEAR TEST

The hollow cylinder apparatus used in this study has been used for characterizing the fine-grained soils in Soil Mechanics Laboratory, Hokkaido University. This apparatus was fully automated with PC control, and equipped with high precision load, displacement, rotation, and torque sensors. The local torsional shear strain along the sample mid-height was measured with two electromagnetic gap sensors, while the global torsional strain was

measured with a potentiometer. The axial stress and torque were measured with an in-cell two-component force-torque load cell. The specimen and inner cell volume changes were measured with double burette systems with a low-capacity differential pressure transducer. Torque was applied by a stepper motor in a strain controlled manner, while axial load was applied by a double-acting bellofram cylinder. The undrained simple shear conditions with stress and strain boundary conditions similar to that of the constant-volume direct shear test was achieved by clamping the axial ram of bellofram cylinder, and closing the specimen drainage and the inner cell drainage valves. The detail descriptions of principle and experimental procedure of a similar hollow cylinder apparatus can be found in Nishimura et al. (2007).

Sample preparation

After the removal of wax layer and cling film of a large cylindrical sample, the sample was trimmed down to a cylindrical specimen of diameter 70mm in a soil lathe. The cylindrical specimen was then encased within a two-part steel mould, as shown in **Figure 4.8 (a)**. The steel mould was then tied up by two different end caps screwing with four bolts for the excavation of inner cell cavity. The two end caps were with holes of diameters 10mm and 30mm, respectively. In order to maximize the friction between the steel mold and the outside of specimen, a thin plastic film was also used to cover the specimen.

The inner hole was excavated initially by using a drill of diameter 10mm in a similar way as Porovic (1995) and Albert et al. (2003). The end cap with a diameter of 10mm was then replaced by another end cap with a diameter of 30mm. The drill was substituted by a miniature straight edged knife and the cavity was increased to the inner cell diameter of 30 mm, as shown in **Figure 4.8 (a)**. In the meantime, the initial water content was measured. The dimension of the specimen was then measured at three different positions and the

measured values were averaged. The weight of the specimen was also measured. Immediately after trimming, the specimen was wrapped with a cling film and transferred to the apparatus.

Experimental set up

Before the sample preparation, the steps such as saturation of porous discs and water channels, resetting zero readings of sensors, installation of platens, preparation of membranes etc., were undertaken to minimize a time between unsealing of the sample and application of the cell pressures. As the intact Izumi clay was heavily overconsolidated and stiff, three specimens were tested by using two end discs with short vanes (2mm) and long vanes (5mm), and gypsum bonding along the specimen-platen interfaces, to prevent pre-failure slippage along interfaces. Unfortunately, none of the options were completely successful in preventing the specimen-platen slippage, which is presented later. For the tests using porous disc with long vanes, a set of grooves were prepared with a hack-saw blade at each end of the specimen in advance to embed the long vanes of porous discs. The specimen was then placed on the bottom porous discs. Damp strip filter papers of 1cm wide and six in numbers were attached to the outer specimen wall to facilitate the water drainage and the top cap was set in place. The outer and inner cell membranes were then placed over the specimen and four O-rings were used to seal the bottom and top caps. The top cap and load sensor were connected carefully by monitoring with sensors' readings. The potentiometer was then attached along the top cap, and in the meantime two gap sensors were also attached on the specimen to measure circumferential displacements at spacing of 60mm by making equal distances from the top and bottom specimen-platen interfaces. The detail explanation about the strain measurement procedure can be found in Fukutomi (2015). The air bubble trapped between the sample and the membranes was sucked out by applying a suction of about 20kPa through a water channel connected at the bottom of the specimen. The outer cell chamber was put into

the position and then screwed by three bolts on the top. Finally, the apparatus was connected with the loading ram of bellofram cylinder, and then it was fixed firmly by two screws at the bottom. In the meantime, a vertical displacement transducer was attached to the loading ram to measure axial displacement of the specimen.

After completing the apparatus set up, outer and inner cell chambers were filled by dividing into three levels. Initially, the outer cell chamber was filled with de-aired water to the first level and the water was then allowed to flow into the inner cell chamber by hydraulic head so as to make the same level of water. After that, similar procedure was carried out for the second and third levels, until the inner cell chamber was filled completely, as shown in **Figure 4.8 (b).**

(a)

(b)

Figure 4.8. Hollow cylinder simple shear test (a) Specimen preparation (b) Specimen set up

Saturation

The back pressure saturation method was applied to improve the saturation. In which, the back pressure of 200kPa was used. In the meantime, the specimens were loaded isotropically to an effective stress of *p'*=100kPa, except *p'*=20kPa for soft intact Atsuma clay. The Skempton B-value was then measured after keeping about 24 hours. The measured B-values were greater than 0.9 for all the tests, except 0.88 for intact Izumi clay.

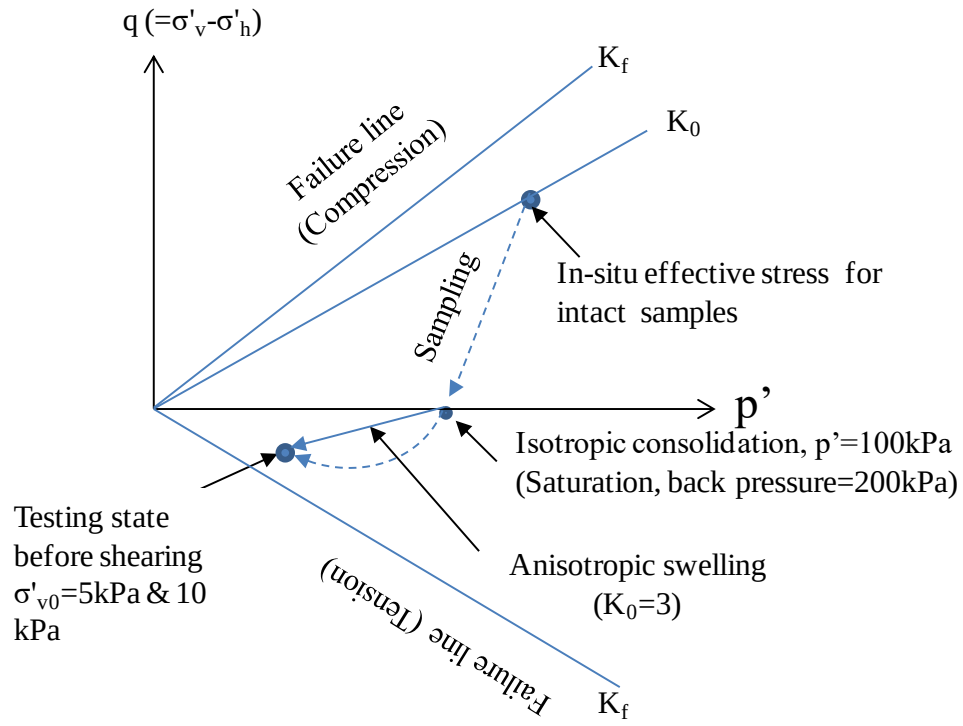

Figure 4.9. Experimental procedure and soil specimen states for hollow cylinder simple shear tests

Consolidation stage

After the isotropic loading and full saturation, the specimens were anisotropically swelled to a vertical effective stress of 10kPa for intact Izumi clay by following quasi-K_0-paths (straight line connected path, as shown in **Figure 4.9**), while it was 5kPa for all other specimens. K_0 value was estimated to be 3, near the coefficient of passive earth pressure, for this low

effective stress level and high OCR. The unloading rate was maintained constant of about 1-2 kPa/hour. These unloading processes were continued until the axial strain and volume strain lower than 0.001% per hour was attained.

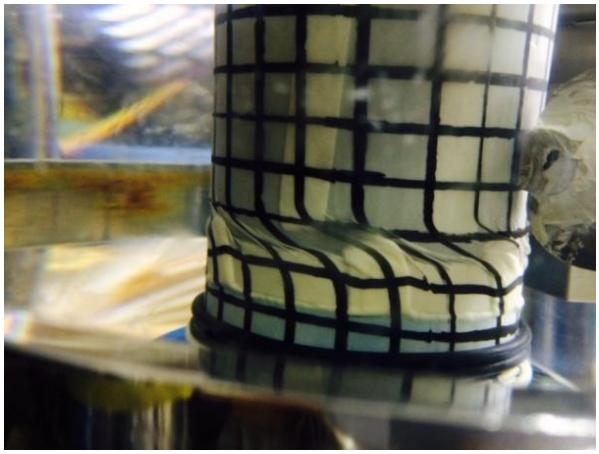

(a)

(b)

Figure 4.10. Hollow cylinder simple shear tests (a) Problem of interface slippage during shearing in intact Izumi clay (b) Simple shear deformation during simple shearing

Simple shearing stage

After the anisotropic unloading/swelling stage, the specimen was sheared torsionally by applying a shearing rate of 0.006%/minute, while closing the specimen and inner cell drainage valves to keep all the normal strains zero. For the intact specimen of Izumi clay, the

shearing was not completely successful due to specimen-platen slippage, as shown in **Figure 4.10 (a)**, but some data before shearing were reliable as indicated by the measurements of local and global strains. In all other tests, complete shearing was carried out by using porous discs with long vanes, and the simple shear deformation was monitored by taking photographs of grid deformations drawn on the outer rubber membrane, as shown in **Figure 4.10 (b)**. The shearing was stopped when a maximum shear strain of about 30% was attained.

4.5 EXPERIMENTAL PROGRAMMES

A series of constant-volume direct shear tests was performed with different consolidation stresses i.e. 10, 20, 50, and 400kPa. The void ratios just before shearing were calculated by using the initial water content and the subsequent consolidation strain. This void ratio was then finally verified by the final water content measured at the end of shearing. The experimental programme is summarised in **Table 4.2.**

Table 4.2. Summary of constant-volume direct shear tests on Izumi clay, Atsuma clay, and clay-sand mixed soil

States	Vertical effective stress (kPa)	Izumi clay		Atsuma clay		C-S soil	
		Void ratio	Yield stress, σ_{vy}' (kPa)	Void ratio	Yield stress, σ_{vy}' (kPa)	Void ratio,	Yield stress, σ_{vy}' (kPa)
Intact	10	0.954	1690	1.130	96	-	-
	20	0.945		1.110		-	
	50	0.942		1.090		-	
	400	0.901		0.796		-	
Reconstituted	10	1.046	400	0.891	400	0.807	400
	20	1.031		0.889		0.762	
	50	1.038		0.865		0.752	
	400	0.934		0.761		0.702	
Compacted	10	0.742	*	0.725	*	0.703	*
	20	0.732		0.719		0.692	
	50	0.717		0.691		0.678	
	400	0.621		0.575		0.656	

* Not clearly observed below 3000kPa.

Likewise, the hollow cylinder simple shear tests were performed on the specimens of three different soils. The experimental programme is presented in **Table 4.3**.

Table 4.3. Summary of hollow cylinder simple shear tests on Izumi clay, Atsuma clay, and clay-sand mixed soil

States	Vertical effective stress (kPa)	Izumi clay		Atsuma clay		C-S soil	
		Void ratio	Yield stress, σ_{vy}' (kPa)	Void ratio	Yield stress, σ_{vy}' (kPa)	Void ratio	Yield stress, σ_{vy}' (kPa)
Intact	10/5**	0.940	1690	1.156	96	-	-
Reconstituted	5	1.054	400	0.901	400	0.817	400
Compacted	5	0.732	*	0.715	*	0.763	*

* Not clearly observed below 3000kPa, **10kPa for intact Izumi clay and 5kPa for Intact Atsuma clay.

CHAPTER 5 EXPLORATION OF NEAR-SURFACE STRENGTH OF RIVER DYKE SLOPES: MATERIALS AND METHODS

5.1 INTRODUCTION

This chapter presents the studied embankments, and the materials and methods employed in the second part of this research. The embankment, a dyke surrounding Maizuru flood-control site along Chitose river in Hokkaido, was investigated to understand the hydraulic and mechanical behaviour of soils. Additional field and laboratory data were obtained for dykes of two other flood-control sites, Ebetsubuto and Higashinosato, to assist the interpretation of Maizuru dyke and augment laboratory test data. **Figure 5.1** shows the locations of these three river dykes. The construction of Maizuru embankment was completed in 2013, whereas other two embankments were under construction when this study was carried out. The materials used for the construction of these embankments were initially the mixture of clay and sand in a proportion approximately 1:1 by volume, as mentioned in Chapter 4. For Higashinosato dyke, which is being constructed in three stages, eventually adopted higher proportions of sand for the second and the third stages to improve the dyke's strength. The field compaction was carried out by adopting the state at the wet of optimum in the laboratory compaction curve.

To understand the undrained strength behaviour, a series of undrained isotropic triaxial compression tests was performed in the laboratory on the compacted specimens of clay-sand mixed soil sampled from these three river dyke construction sites. On the other hand, to understand the in-situ strength after construction, portable cone penetrometer tests, both static and dynamic, were performed in 3-5 years Maizuru embankment and recently-constructed Higashinosato embankment. In addition, calibrations of both penetrometers were performed in a laboratory-compacted model ground.

Figure 5.1. Photograph showing locations of Maizuru, Higashinosato and Ebetsubuto river dykes

5.2 EMBANKMENT AND FIELD MONITORING

In this study, two embankments were investigated which include 3-5 years old Maizuru and recently-constructed Higashinosato located in a floodplain along Chitose River, Hokkaido, Japan, as mentioned earlier. The Maizuru embankment was constructed in three different stages with the height added by 1.4m, 2.6m and 1.7m in 2010, 2011, and 2013, respectively (Nishimura et al., 2015); the slope was maintained as 1:4 on both sides. The ground condition of Maizuru embankment is relatively uniform along the embankment length. At the studied site (SP250), the original ground consists of a thin (about 2 m) alluvial clay underlain by a thick layer of volcanic sand. **Figure 5.2** shows the cross-section of studied embankment in which the monitoring station was installed at the mid-slope. The installation had been completed by the team from Hokkaido University in 2014, prior to this test (Nishimura et al., 2015). The climate station was installed on the ground which recorded the climate data such as precipitation, snow cover, humidity and temperature. The precipitation and humidity data turned out not to be accurate and eventually data from AMeDAS Chitose weather station (Japan Meteorological Agency) were adopted for analysis. Below the dyke surface, the pore water pressure, volumetric water content and temperature were measured at different depths ranging from shallower to deeper, as labelled in the figure. The locations of in-situ strength tests, both static cone penetrometer test (SCPT) and dynamic cone penetrometer test (DCPT), at an interval of 3m along the slope surface by dividing the slope into three regions (top, mid and toe) are also shown in the figure.

The ground surface of Maizuru embankment was densely covered with grass, as shown in **Figure 5.3**. The Higashinosato embankment, on the other hand, was recently constructed and still kept without any surface vegetation. As both embankments are located in the snowy cold region of Hokkaido, the surface receives significant snow cover (maximum up to 0.7-1m) for

about four months in winter. During snow melting season, the surface soil receives significant wetting with a rise of pore water pressure close to hydrostatic levels, as measured by the field monitoring. In spring and summer, the surface soil receives significant drying**.**

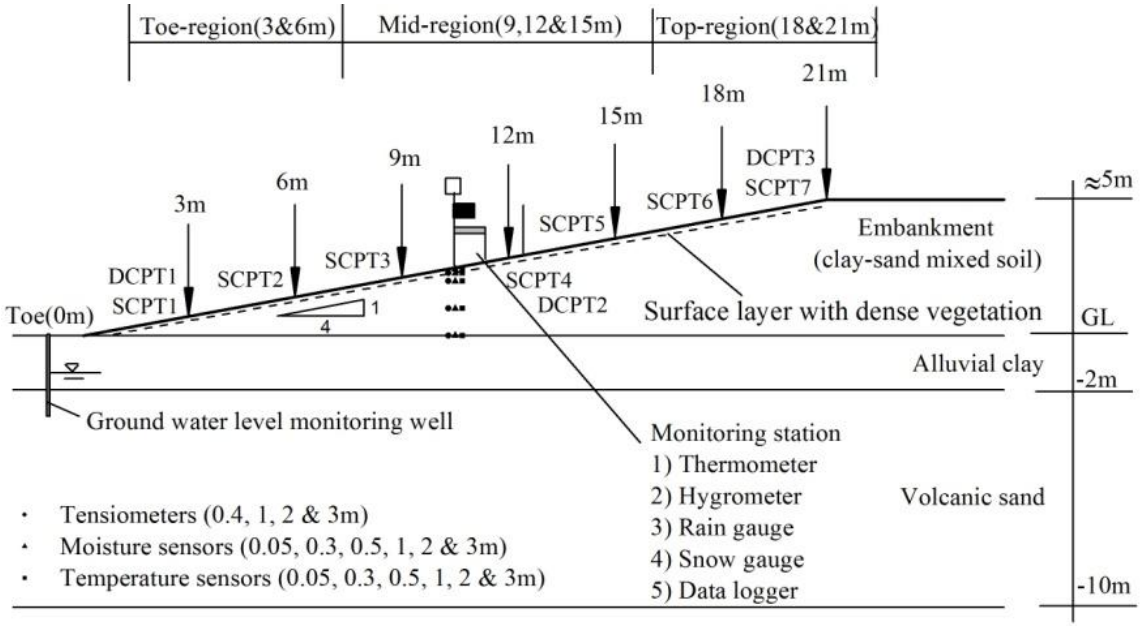

Figure 5.2. Cross-section of embankment, field monitoring instrumentation and testing locations for static/dynamic cone penetrometer tests in Maizuru site


Maizuru river dyke surrounding
Maizuru flood control site
Studied area and location
of field monitoring station
in Maizuru river dyke
2D
Google
ZENRIN Google DigitalGlobe Camera : 1,701 m 42°54'50"N 141°42'25"E 6 m 100%

(a)

(b)

(c)

(d)

(e)

(f)

Figure 5.3. Photographs showing surface conditions in Maizuru river dyke (a) overall view of dyke surrounding (b) 02-Feb-2016(c) 10-March-2016 (d) 13-May-2016(e) 05-Sep-2016 (f) 12-Nov-2016

5.3 MATERIALS

As this study focused on investigating the near-surface strength of river dyke slopes, which have been already constructed and recently under construction, the materials were sampled undisturbed from a constructed slope in Maizuru, as well as disturbed from two construction sites. Two on-site mixtures of alluvial clay and sand, which were sampled from river dyke construction sites located at Ebetsubuto and Higashinosato, and undisturbed samples, which were sampled from Maizuru embankment close to the location of penetrometer testing, were

studied. The depth of undisturbed sampling was chosen to be 0.4-0.5m from the surface at the mid-slope. This depth corresponded to a transition zone of cone penetrometer strength resistance patterns, as will be discussed later. The standard proctor compaction curves and gradation curves for these tested materials are shown in **Figures 5.4** and **5.5**. Comparing these curves, they are broadly similar, except that Ebetsubuto soil is more clayey as indicated by the gradation curves. The physical properties and the detail strength characterization of compacted soil from Maizuru embankment during construction have been presented by Panta and Nishimura (2017). **Table 5.1** gives the physical properties of all three tested materials.

5.4 PREPARATION OF COMPACTED SAMPLES

The laboratory-compacted samples, which are defined as as-compacted samples, were prepared by compacting soils with the standard proctor compaction energy (598kJ/m^3) in the standard proctor mould, as explained in Chapter 4. Three different states (1.05w_{opt}, 1.15w_{opt} and 1.30w_{opt}) at the wet of optimum were adopted for the laboratory compaction because the water content used in field compaction was in this range, as shown in **Figure 5.6**. The degrees of compaction for all the as-compacted samples of different states were above 90% and the degrees of saturation were larger than 90%. Adopting the state wet of optimum for the compaction of embankments can avoid large collapse deformation and decrease in soil strength and stiffness upon wetting (Tarantino and De Col, 2008; Alonso et al., 2013; Tatsuoka, 2015). Whereas adopting the state too wet of the optimum may cause the problem of excessive shrinkage and subsequent development of cracks which may eventually exacerbate the strength deterioration of surface soil. Therefore surface topping such as grass is necessary to counter this problem.

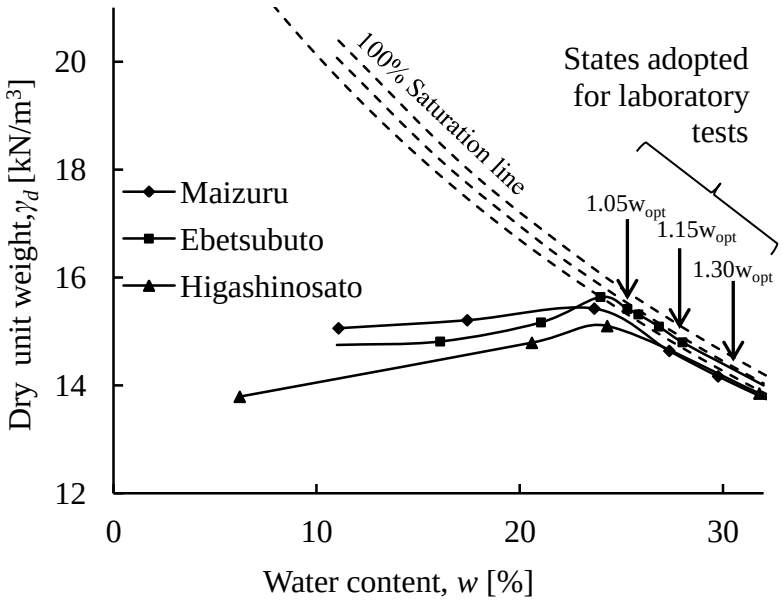

Figure5.4. Standard proctor compaction curves for tested soils

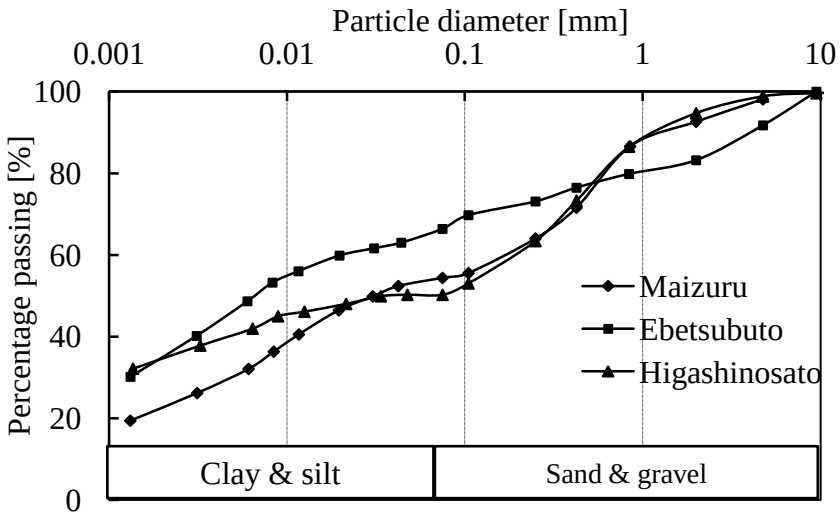

Figure 5.5. Particle size distribution curves for tested soils

(a)

(b)

Figure 5.6. Sample preparation (a) Clay-sand mixed soils from Maizuru embankment (b) Standard proctor mould and hammer used for soil compaction

Table 5.1. Physical properties of tested materials

Name of soil	w_n(%)[3]	w_p (%)	w_l (%)[1]	G_s	Clay fraction (%)[2]	Sand / Gravel (%)
Maizuru	27.4	30	49	2.711	22/30	39/7
Ebetsubuto	31.7	29	59	2.641	36/40	35/17
Higashinosato	31.8	25	54	2.581	36/44	50/6

[1] Measured for constituents passing through a 425μm sieve

[2] (Finer than 2μm)/(Finer than 5μm)

[3] As measured in field after compaction

5.5 TESTING METHODS

The strength behaviours of clay-sand mixed soils in both laboratory-compacted (as-compacted) and field-compacted (undisturbed) states were investigated by performing laboratory element tests in association with in-situ strength tests. The laboratory element tests include a series of undrained isotropic triaxial compression tests at low to medium consolidation pressures (p'=10-400kPa). The in-situ strength tests include a portable static/dynamic cone penetrometer tests performed at regular intervals over a year in river dyke slopes. In addition, the pore water pressure as a potentially major parameter governing the in-situ strength variation is also needed, which is both measured by field monitoring and simulated by using a finite element seepage flow model proposed by Nishimura et al. (2015, 2016).

5.5.1 TRIAXIAL COMPRESSION TESTS

Principle and apparatus

Triaxial test is a widely used shear test in the laboratory to investigate the strength of fine-grained soils with relatively high precision at low stresses. Observing the state of a soil along the potential slip surface just before failure, the soil may experience initially compression to simple shear modes and finally extension mode during failure. The constant-volume direct

shear tests are considered more relevant reflecting the failure mechanism at the verge of shallow slope failure, as explained in Chapter 4. Understanding the strength of soil before failure, the study investigating the strength from triaxial compression tests on similar soils is required to complete the research. Therefore, a series of isotropic triaxial compression tests was planned and performed on the field-compacted (undisturbed) samples from the Maizuru embankment together with laboratory (as)-compacted samples.

5.5.2 PORTABLE CONE PENETROMETER TESTS

Principle and apparatus

The portable cone penetrometer test is an easy and convenient method for the exploration of shallow vegetated slopes at different locations repeatedly compared to the standard penetration test and cone penetration test, which is less mobile, require larger equipment and disturbs the wider surface. The static cone penetrometer apparatus consists of a pushing handle, a proof-ring with dial gauge, rods of 50cm in length and 16mm in diameter, load hangers, and weights. The cone has an apex angle of 60^{o} and a cross-sectional area of $3.24cm^{2}$, as shown in **Figure 5.7 (a)**. The resistance offered by the soil at a tip of the cone is measured as the penetration resistance, maximum about 2.87MPa; this can be measured with the proof-ring at every 10cm penetration.

The apparatus of dynamic cone penetrometer consists of a guide rod, a hammer (5kg), rods and a cone with dimensions same as the static cone penetrometer but with a tapered tip tale, as shown in **Figure 5.7 (b)**. The number of drops of falling hammer from a height of 50cm at every 10cm penetration is recorded as the penetration resistance.

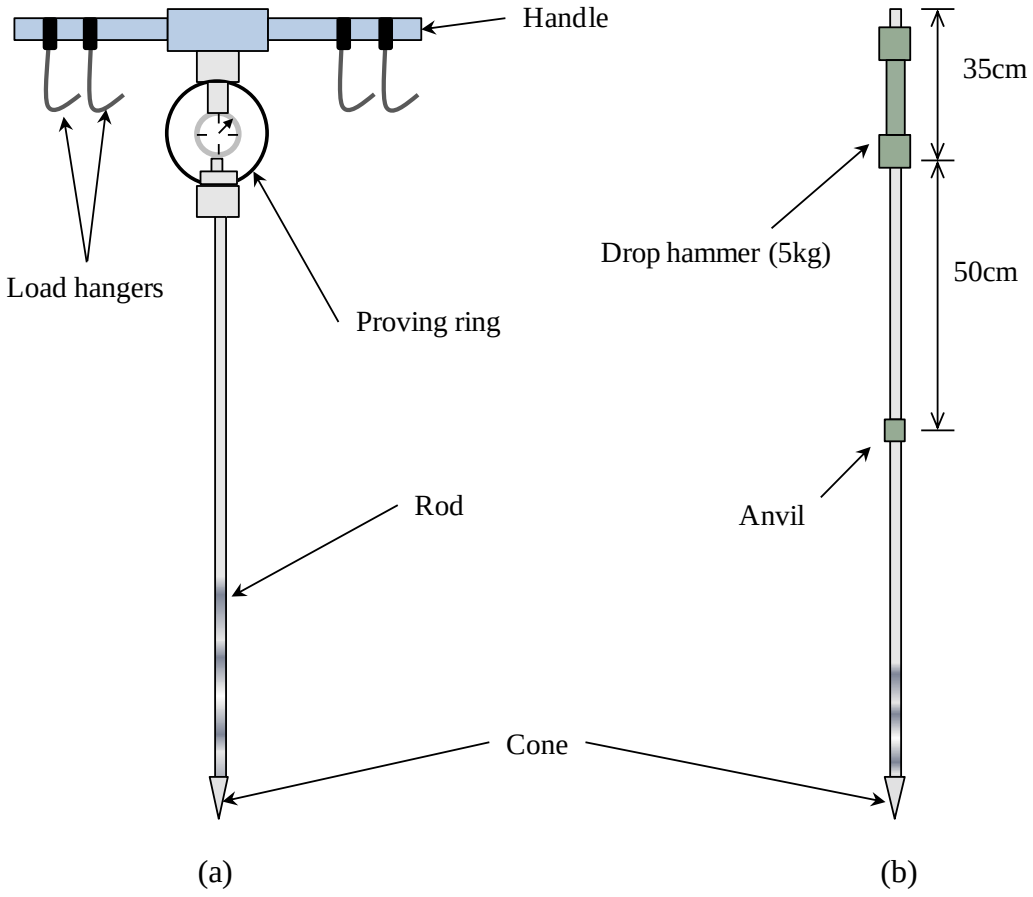

Figure 5.7. Schematic diagram of cone penetrometer apparatus (a) static (b) dynamic

5.5.3 NUMERICAL SIMULATION OF PORE WATER PRESSURE

The pore water pressure at different depths and locations was simulated by using a seepage flow model, which considers unsteady unsaturated seepage flow by solving Richards' equation (as discussed in Nguyen et al., 2014) by using non-linear finite element methods. This model also incorporates an evapotranspiration model by using Hamon's (1961) equation. The details of the model, parameters used and boundary conditions are presented by Nishimura et al. (2015 and 2016). Thus simulated pore water pressure considering both infiltration and evapotranspiration at different depths and regions of a slope reproduced well the measured pore water pressure at 0.4m depth, even when the model assumed a relatively simple scenario of undrained surface during a period of accumulation of snow, and thaw

infiltration by applying total precipitation uniformly over the thawing period. The boundary between the accumulation period and the thawing period is defined as the time of peak snow cover thickness. In the simulation, the coefficient of permeability for shallower depth (0.5m) was assumed larger value than deeper depth. The analysis was essentially a re-run of Case 4 in Nishimura et al., (2016) with extended simulated period. Refer to the work for the specific modelling and parameter set.

The predicted pore water pressure at shallower depth reacted sharply with rainfall as observed in the field measurement. Comparing the predicted profiles of pore water pressure for top-, mid- and toe-regions at shallower depths, the top-region showed slightly lower pore water pressure than other two regions at the same depth, probably due to the gravimetric flow of water moving towards the mid- and toe-regions keeping soils wetter than the top-region. The simulated pore water pressure results are presented together with the field monitoring data in Chapter 7.

5.6 EXPERIMENTAL PROCEDURES

5.6.1 TRIAXIAL COMPRESSION TESTS

In this research, the triaxial apparatus driven by mega direct-drive motor, with complete driving and monitoring system, was employed, as shown in **Figure 5.8**. The apparatus is run by Windows software with automatic control, data acquisition and real time plotting capabilities. The pore water pressures at the top and the bottom of sample, and the cell pressure are measured by using pressure transducers; and the axial load is measured by using a load cell. The direct-drive motor (Mega-torque motor) allows the control of axial displacement accurately, with a precision smaller than 0.00001mm.

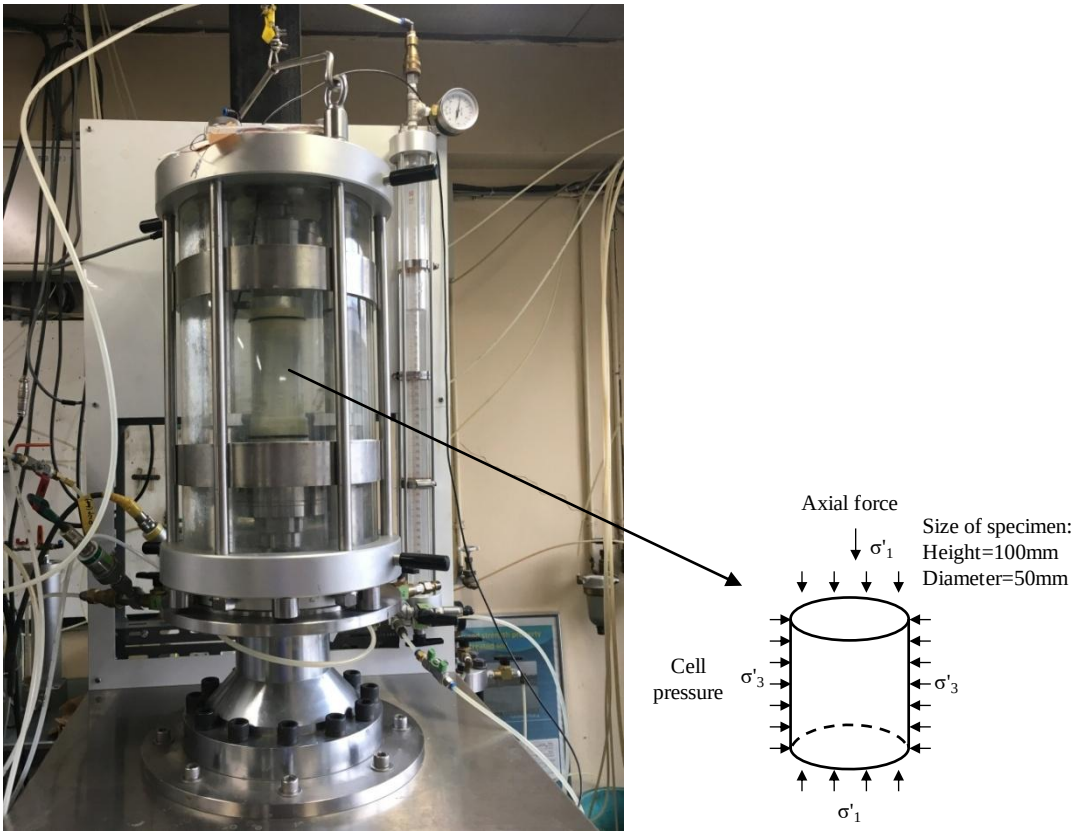

Figure 5.8. Photograph of mega-torque triaxial apparatus used in this study and stress states in triaxial specimen

Sample preparation

As the focus of this study was on the compacted specimens, the clay-sand mixed soil was first compacted in a standard proctor mould following the procedure same as in a standard proctor test. The sample was then removed from the mould and wrapped with a cling film to prevent moisture loss before preparing a triaxial specimen. The size of the triaxial specimen was 50mm in diameter and 100mm high, which was trimmed carefully in a soil lathe from the initial standard proctor specimen of size 100mm in diameter and 125mm high, as shown in **Figure 5.8**. In the meantime, the initial water content was measured twice. The dimension of the specimen was then measured in three different positions, and an averaged value was

taken. After measuring the weight of the specimen, it was wrapped with a cling film and transferred to the apparatus.

Experimental set up

After the sample preparation, the steps such as saturation of porous discs and water channels, resetting the zero reading of sensors, installation of platens, preparation of membranes and filter papers etc., were undertaken to minimize a time between unsealing of the sample and application of cell pressures. The specimen was then placed on the bottom pedestal. Damp strip filter papers of 1cm width and six in numbers were attached around the specimen to facilitate water drainage during consolidation and shearing. Rubber membrane was then placed around the specimen attaching with two O-rings at the bottom pedestal. The specimen was then raised together with the pedestal by the motor until its upper surface met the top cap, by checking the load sensor's reading on the window to avoid compression. The rubber membrane was again attached with two O-rings. The cell chamber was then put into the position fixing with three bolts on the top and it was filled completely with de-aired water.

Saturation

After completing all the apparatus set up, the back pressure saturation method was applied to improve the saturation of the specimen. The back pressure of 200kPa was applied. Skempton B-value was then measured after keeping about 24hours; it was close to 0.8 for all the tested specimens.

Consolidation stage

After the saturation stage, isotropic loading was carried out with effective stresses of 10kPa, 20kPa, 50kPa and 400kPa for each test in a series. The rate of isotropic loading was about 2kPa/min. After reaching the desired effective stress, the consolidation process was continued for at least 24hrs.

Undrained shearing stage

After the consolidation stage, the specimen was sheared axially by applying a shearing rate of 0.05%/min, while keeping the specimen drainage valves closed. Evolution of pore water pressure was monitored during the shearing stage on a real time plot. The shearing process was terminated when the maximum axial strain of 15% was reached.

5.6.2 PORTABLE CONE PENETROMETER TESTS

The experimental procedure of portable static cone penetrometer involves pushing the cone into a soil surface through the handle first by hands and then by hanging loads in load hangers until reaching the maximum penetration resistance of about 2.87MPa. The rate of penetration was maintained as close as 10mm/sec. The penetration resistance was measured with the dial gauge on the proof ring at every 10cm depth. The rod of length 50 cm was connected after penetrating every 50cm depth until reaching the maximum penetration resistance of 2.87MPa or maximum depth of 5m from the surface.

The experimental procedure of dynamic cone penetrometer involves dropping the hammer of weight 5kg along the guide rod from a height of 50cm. The number of blows required to penetrate every 10cm depth was recorded as the penetration resistance. The rod of length 50 cm can be connected after penetrating every 50cm depth, until the maximum depth of 5m from the surface reached.

Calibration of cone penetrometers

Both static and dynamic cone penetrometers were calibrated in a laboratory-compacted model ground, following the procedure same as in the field, on the compacted clay-sand mixed soils with compaction energy same as in the standard proctor test, as shown in **Figure 5.9**. The cylindrical PVC container 200mm in diameter and 600mm high was chosen for calibration tests, in which the boundary effect was initially confirmed by performing the tests

on two additional containers with diameters of 250mm and 300mm, and 600mm high. Comparing the depth profiles of penetration resistances performed in these three different containers compacting with the Ebetsubuto soil at water content of 1.30w_{opt}, it can be seen that they are broadly same, except close to the bottom boundary, as shown in **Figure 5.10(a)**. Similar to the triaxial tests, three different states of soil were used for the compaction with water contents of 1.05w_{opt}, 1.15w_{opt}, and 1.30w_{opt} at the wet of optimum. The depth profiles of penetration resistance obtained from three different calibration tests with water contents of 1.05w_{opt}, 1.15w_{opt}, and 1.30w_{opt} are presented in **Figures 5.10(b)** and **5.11.** The pore water pressure was measured with tensiometers at four different depths of 100mm, 250mm, 400mm, and 550mm from the surface, and the water content was also measured at the same depths at the end of each test. The depth profiles of the measured suction and water contents in three different calibration tests are presented in **Figure 5.12.**

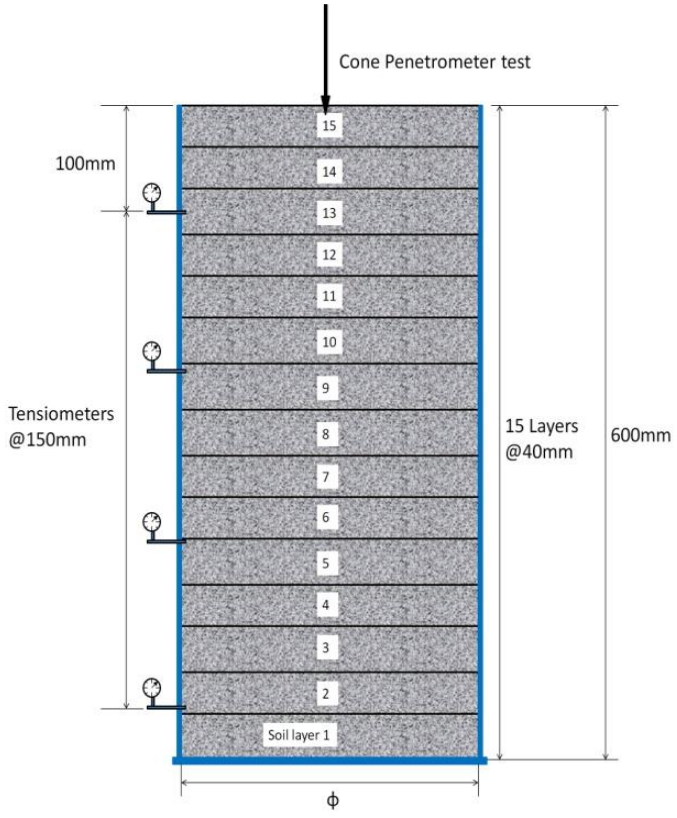

Figure 5.9. Calibration of cone penetrometer in laboratory-compacted model ground

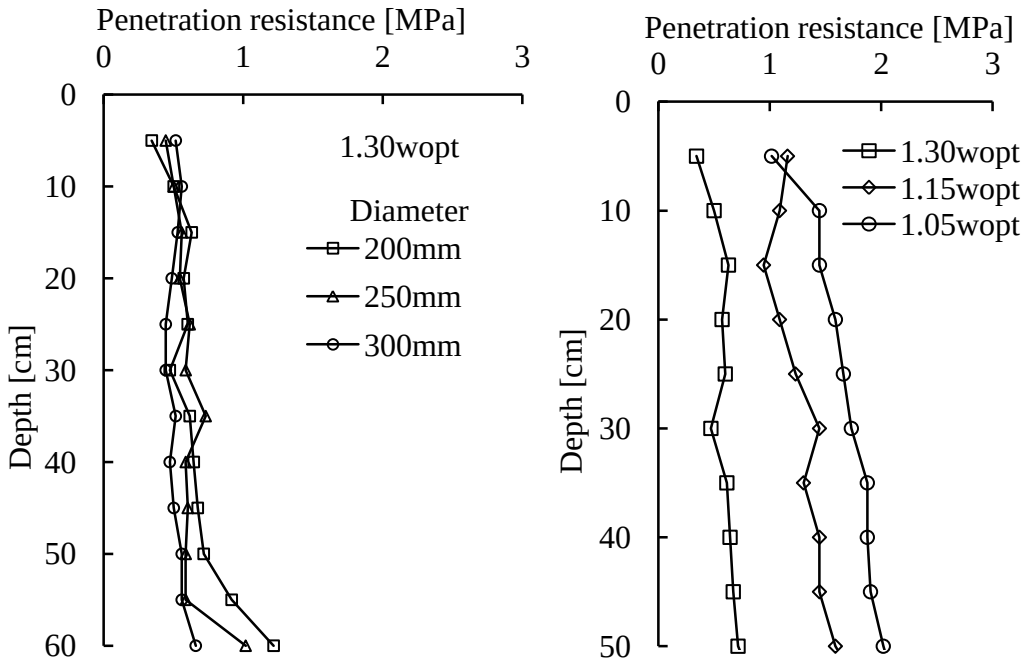

Figure 5.10. Depth profiles of penetration resistance from static cone penetrometer tests performed in laboratory-compacted model ground (a) container with different diameters but same water content (b) container with same diameter but different water contents

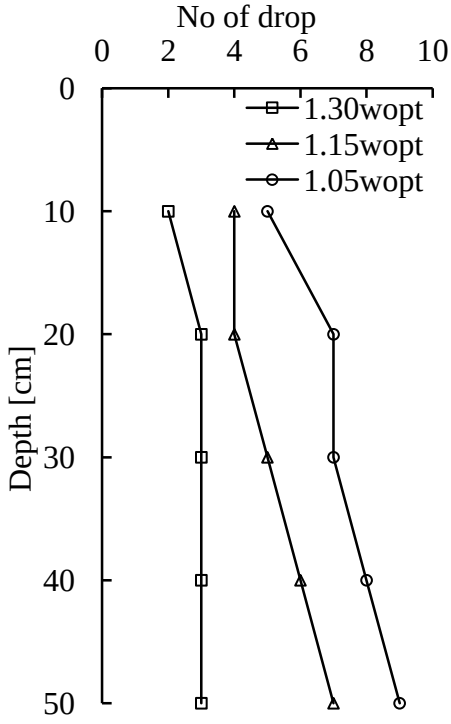

Figure 5.11. Depth profiles of penetration resistance from dynamic cone penetrometer tests performed in laboratory-compacted model ground

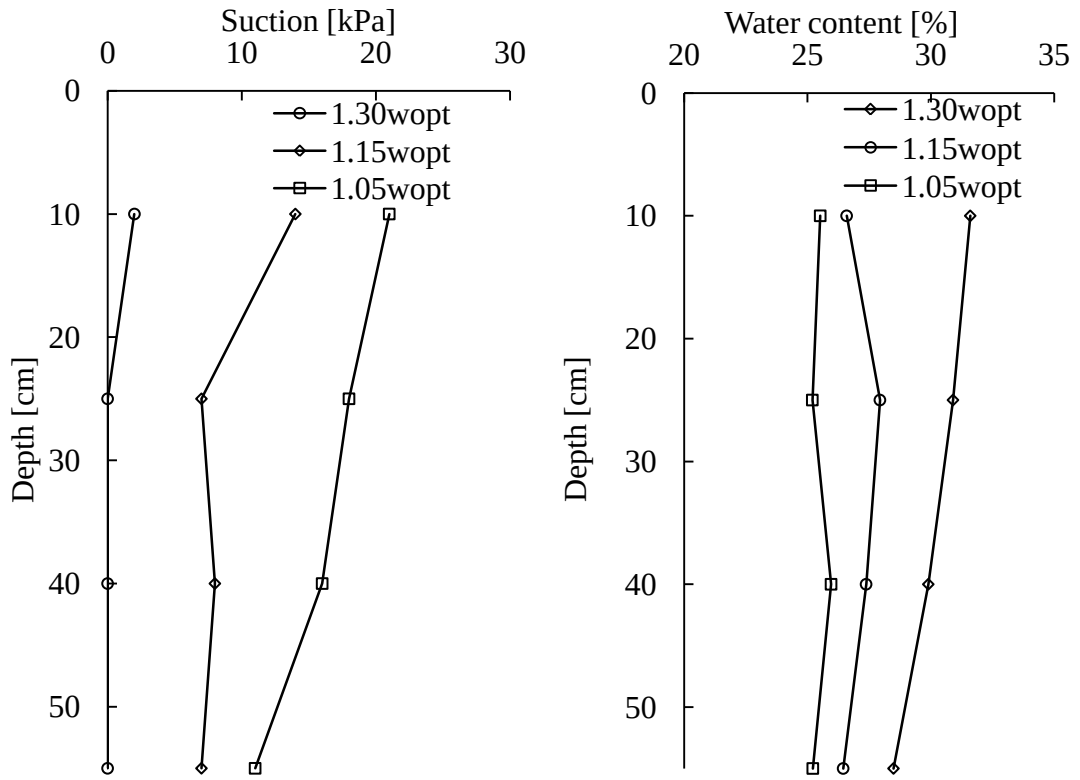

Figure 5.12. Depth profiles of suction and water content measured in laboratory-compacted model ground

5.7 EXPERIMENTAL PROGRAMMES

5.7.1 TRIAXIAL COMPRESSION TESTS

A series of isotropic triaxial compression tests was performed on different states of laboratory-compacted Ebetsubuto and Higashinosato soils, and undisturbed Maizuru soil at low to medium consolidation pressure (p'=10-400kPa). The void ratio before shearing was calculated from the final water content measured at the end of shearing. The undrained strength was assumed as the maximum shear stress on the undrained effective stress path. The experimental programme is summarized in **Table 5.2**.

Table 5.2. Experimental programme for Isotropic triaxial compression tests

Soil	Soil state	Test No	σ_{v0}' [kPa]	Initial dry unit weight, γ_d [kN/m^3]	Initial water content, w [%]	Void ratio before shearing, e	Undrained strength , c_u [kPa]
Ebetsubuto	1.05w_{opt}	ITC-1	10	14.94	25.66	0.760	63.16
		ITC-2	20	14.84	26.31	0.747	73.54
		ITC-3	50	14.75	26.43	0.722	83.16
		ITC-4	400	14.83	26.76	0.658	270.90
	1.15w_{opt}	ITC-5	10	14.41	28.9	0.792	50.74
		ITC-6	20	14.43	29.73	0.781	65.54
		ITC-7	50	14.49	28.34	0.757	71.78
		ITC-8	400	14.49	28.13	0.675	248.99
	1.30w_{opt}	ITC-9	10	14.28	30.55	0.837	37.58
		ITC-10	20	14.22	30.65	0.816	38.81
		ITC-11	50	14.32	29.99	0.789	56.38
		ITC-12	400	14.24	30.02	0.688	232.28
Higashinosato	1.30w_{opt}	ITC-13	10	13.80	31.17	0.874	38.81
		ITC-14	20	14.07	30.17	0.859	44.80
		ITC-15	50	14.15	29.81	0.820	64.88
		ITC-16	400	13.94	30.44	0.708	252.11
	1.05w_{opt}	ITC 17	10	-	-	-	69.65
Maizuru	Undisturbed (Close to optimum)	ITC-18	10	15.77	23.98	0.721	85.59
		ITC-19	20	15.75	23.08	0.711	95.47
		ITC-20	50	15.79	24.45	0.685	117.94
		ITC-21	400	15.74	23.13	0.623	333.28
	1.05w_{opt}	ITC-22	20	15.99	23.19	0.652	131.95
		ITC-23*	50	15.96	23.40	0.614	72.09
		ITC-24*	10	16.20	23.13	0.608	41.95

*Results were not reliable due to a problem with sensors' calibration.

5.7.2 PORTABLE CONE PENETROMETER TESTS

The in-situ surface strength was measured each month from February, 2106 to February, 2017 by performing the portable static cone penetrometer tests across the river dyke slope at seven different locations along the cross-section direction at two longitudinal positions ('Line') each time, as shown in **Figures 5.2** and **5.13**. To understand the temporal and spatial variations in strength across the slope, two plans were set out along the embankment length: plan I at every 1m interval and plan II at every 3m interval, as shown in **Figure 5.13**. The dates and line numbers in which the static cone penetrometer tests were performed every month are listed in table together with **Figure 5.13**. On the other hand, the dynamic cone penetrometer tests were performed at an interval of four months.

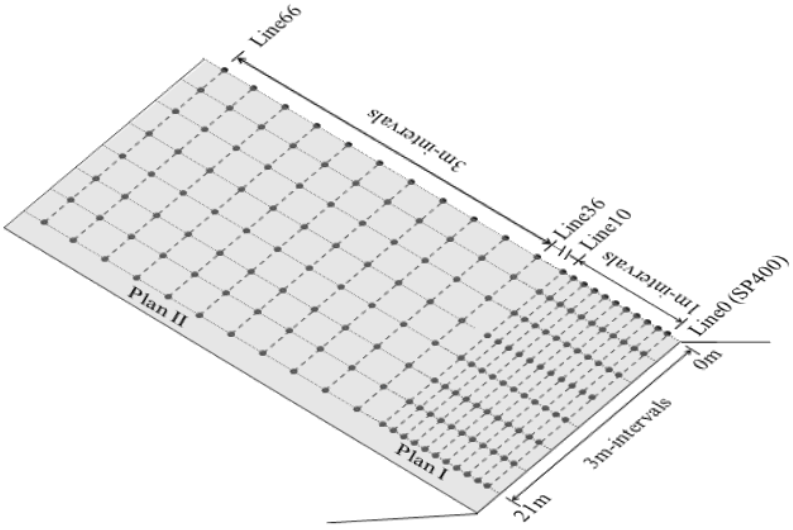

Date	Line no
2016/02/02	Line 0, Line 36
2016/03/10	Line 1, Line 39
2016/04/27	Line 2, Line 42
2016/05/14	Line 3, Line 45
2016/06/22	Line 4, Line 48
2016/08/02	Line 5, Line 51
2016/09/05	Line 6, Line 54
2016/10/19	Line 7, Line 57
2016/11/26	Line 8, Line 60
2017/02/15	Line 9, Line 63
2017/03/27	Line 10, Line 66

Figure 5.13. Plans and dates of cone penetrometer testing in Maizuru river dyke slope

CHAPTER 6 CHARACTERIZATION OF UNDRAINED STRENGTH OF FINE-GRAINED SOILS AT LOW STRESSES: RESULTS AND DISCUSSIONS

6.1 INTRODUCTION

This chapter discusses experimental results obtained from the constant-volume direct shear tests and the hollow cylinder simple shear tests on different states (intact, reconstituted and compacted) of fine-grained soils such as Izumi clay, Atsuma clay, and clay-sand mixed soils, as introduced in Chapter 4. The results are interpreted by focusing on how the undrained strength of fine-grained soils having different structures induced by natural, reconstitution and compaction phenomena behave at low confining stresses by analyzing the undrained effective stress paths and the strength envelopes, while the emphasis is particularly given to non-linearity of the strength envelopes. The non-linearity of the strength envelopes are quantified by applying a non-linear power-law strength criterion. After normalizing the stress paths and the strength envelopes with respect to the intrinsic equivalent pressure, to eliminate the effects of different density or void ratio and OCR just before shearing, the non-linear state bounding surfaces (Hvorslev surfaces) on the dry side of the critical for different states of these soils are compared in a single framework.

Several previous researches (e.g. Seed and Chan, 1959; Barden and Sides, 1970; Burland 1990; Leroueil and Vaughan, 1990; Gens, 1996) have reported that the strength parameters, whatever failure criterion is employed, are never inherent properties and are strongly dependent on the soil state and structure. In this study, the strength parameters for three different states of fine-grained soils are derived at low stresses. In addition, meso-scale soil fabrics in the specimens of reconstituted and compacted states are observed by taking X-ray

micro-CT images, and which are used to explain the state and structure dependent strength behavior in normalized scales.

6.2 CONSTANT-VOLUME DIRECT SHEAR TEST RESULTS

The experimental results obtained from the constant-volume direct shear tests include the undrained effective stress paths and the shear stress-horizontal displacement curves. As the pore water pressure cannot be measured in the direct shear test, the change in vertical stress is equal to the change in pore water pressure in saturated samples under the constant-volume condition. Therefore, the evolution of vertical stress during shearing under the constant-volume is assumed to give the effective stress as in the undrained condition. The undrained effective stress paths are drawn in terms of the horizontal shear stress (τ) against the vertical effective stress (σ'). The non-linear effective strength envelopes and consolidated-undrained strength envelopes are expressed by the non-linear power law function, as proposed by Atkinson (2007).

6.2.1 UNDRAINED EFFECTIVE STRESS PATHS AND STRENGTH ENVELOPES

The undrained effective stress paths for each state of the tested soils are drawn by testing four different samples at the consolidation stresses σ'_0=10, 20, 50, and 400kPa, except two additional tests for the intact Atsuma clay at σ'_0=5kPa, and 96kPa (yield stress) to get a complete picture of the strength behavior. The effective strength envelopes for all the states are drawn by taking the points of maximum stress ratio (τ/σ') on the stress paths. While the consolidated-undrained strength envelopes are drawn by taking the maximum shear stress and the initial vertical effective (consolidation) stress on the stress paths.

Izumi clay

As the Izumi clay is a heavily overconsolidated clay with the yield stress of about 1.7MPa, all the intact samples were tested under the overconsolidated conditions. It can be seen that the undrained effective stress paths for all the samples at low stresses (σ'_0=10kPa, 20kPa, and 50kPa) show stiff and dilative behaviour, as shown in **Figure 6.1 (a)**. The intact stiff samples initially showed uniform and smooth behaviour until reaching the peak states, followed by a rapid loss of strength. The post-peak shear stress increased again, seemingly converging along the intrinsic strength envelope and moving towards a potential critical state. This meta-stable behaviour could be due to shear-induced destructuring, which caused the soil state to that of the intrinsic state, before the shear strength fully mobilized along a horizontal plane Burland et al., (1996). This post-peak behaviour may be affected by the stress and strain non-uniformities in the direct shear specimens. However, its abruptness appears to be pronounced in comparison to the existing data of different overconsolidated soils. This interesting observation led to carry out an investigation by performing the hollow cylinder simple shear tests to explore a possibility of true inter-particle cohesion and eventual tensile failure, which is discussed in a later section. The stress path for the sample at higher stress (σ'_0=400kPa) shows stiff and dilative behaviour until reaching the peak state, which is followed by contraction and strain softening. The effective strength envelope is drawn by taking the points of maximum stress ratio on the stress paths, which shows significantly non-linear soil failure behaviour, the degree of non-linearity b=0.57, as expressed by the power law function. It should be noted that the points of maximum stress ratio and the peak state points are not the same but they are very close to each other, and this small difference does not result in significantly different soil behaviour adopting whether the effective strength envelope or the peak strength envelope.

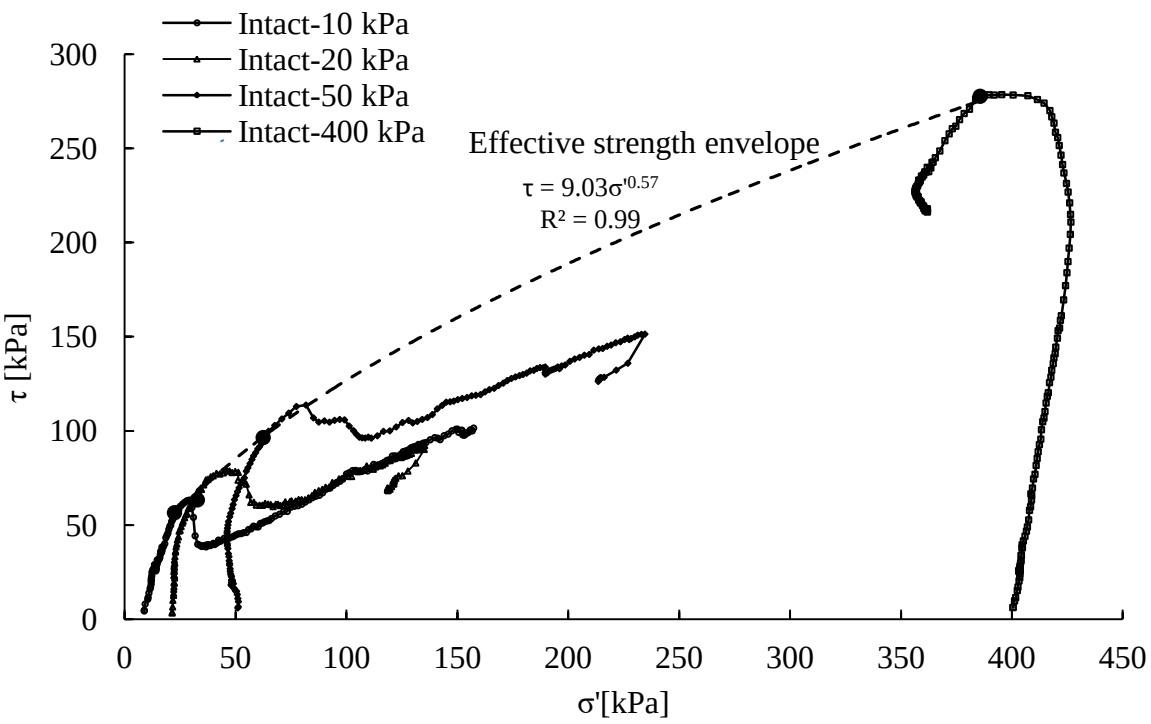
Intact-10 kPa
Intact-20 kPa
Intact-50 kPa
Intact-400 kPa
Effective strength envelope
τ = 9.03σ'^0.57
R² = 0.99
τ [kPa]
σ'[kPa]
0
50
100
150
200
250
300
350
400
450

(a)

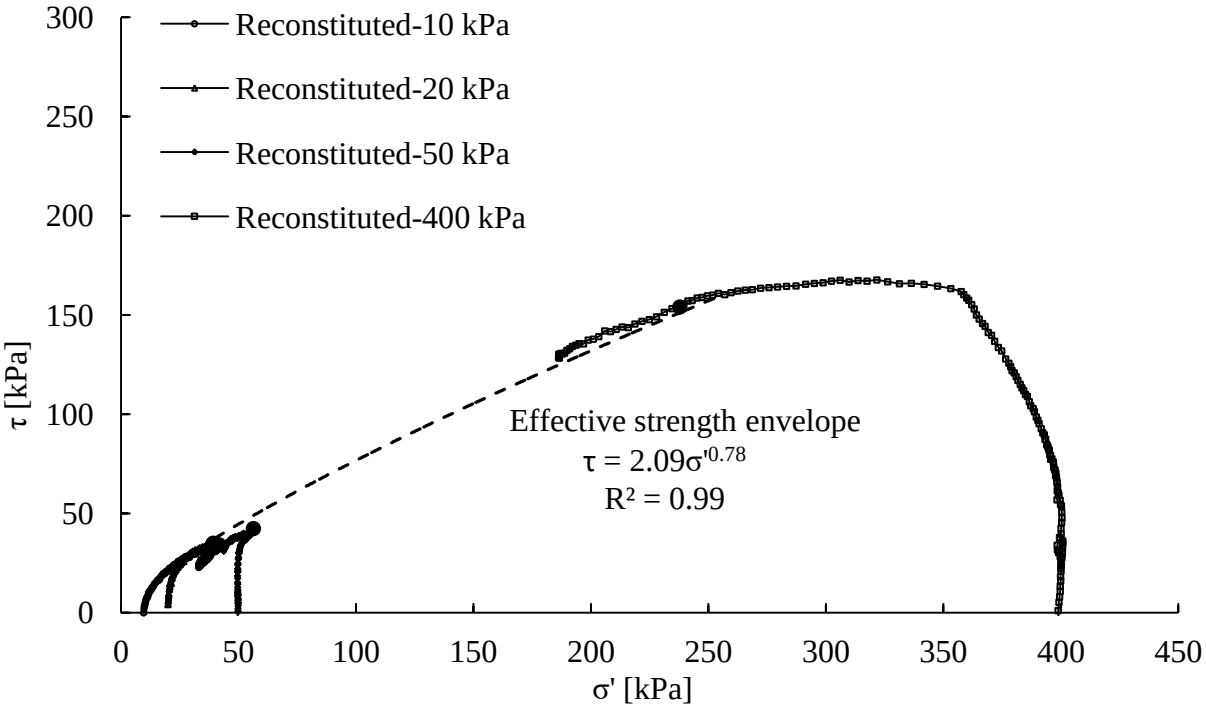
Reconstituted-10 kPa
Reconstituted-20 kPa
Reconstituted-50 kPa
Reconstituted-400 kPa
Effective strength envelope
τ = 2.09σ'^0.78
R² = 0.99
τ [kPa]
σ' [kPa]
0
50
100
150
200
250
300
350
400
450

(b)

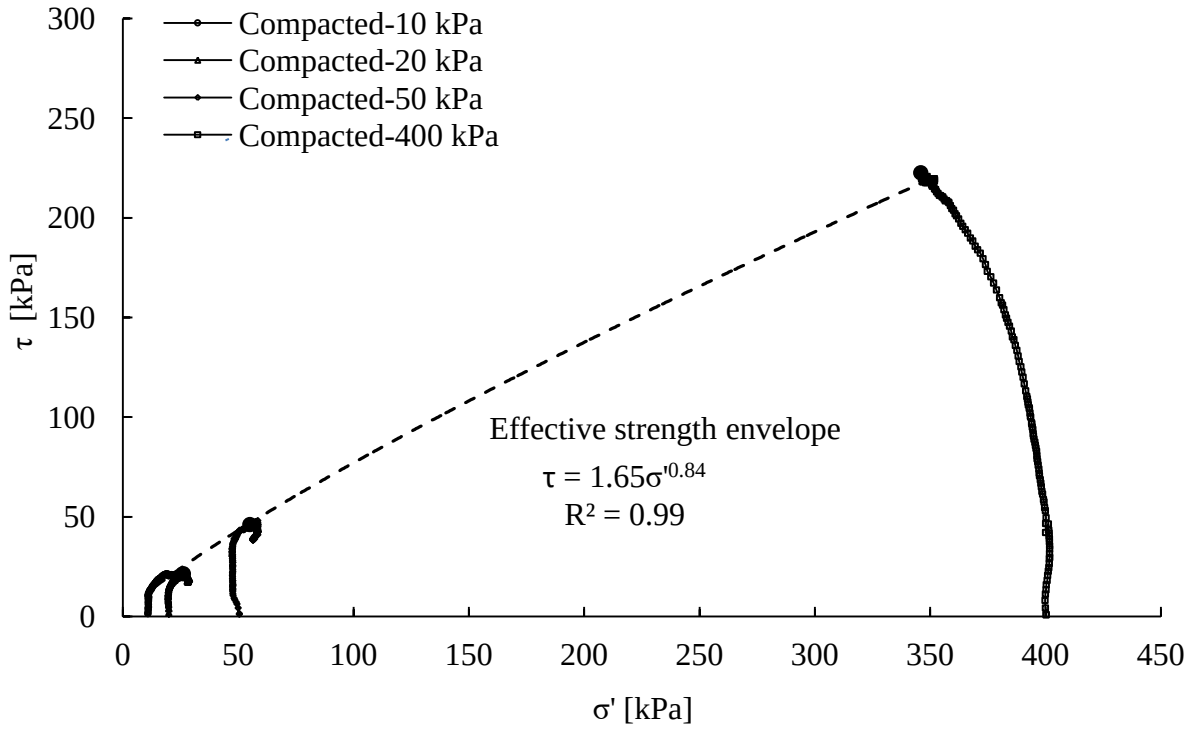
Compacted-10 kPa
Compacted-20 kPa
Compacted-50 kPa
Compacted-400 kPa
Effective strength envelope
τ = 1.65σ'^0.84
R² = 0.99
τ [kPa]
σ' [kPa]
0
50
100
150
200
250
300
350
400
450

(c)

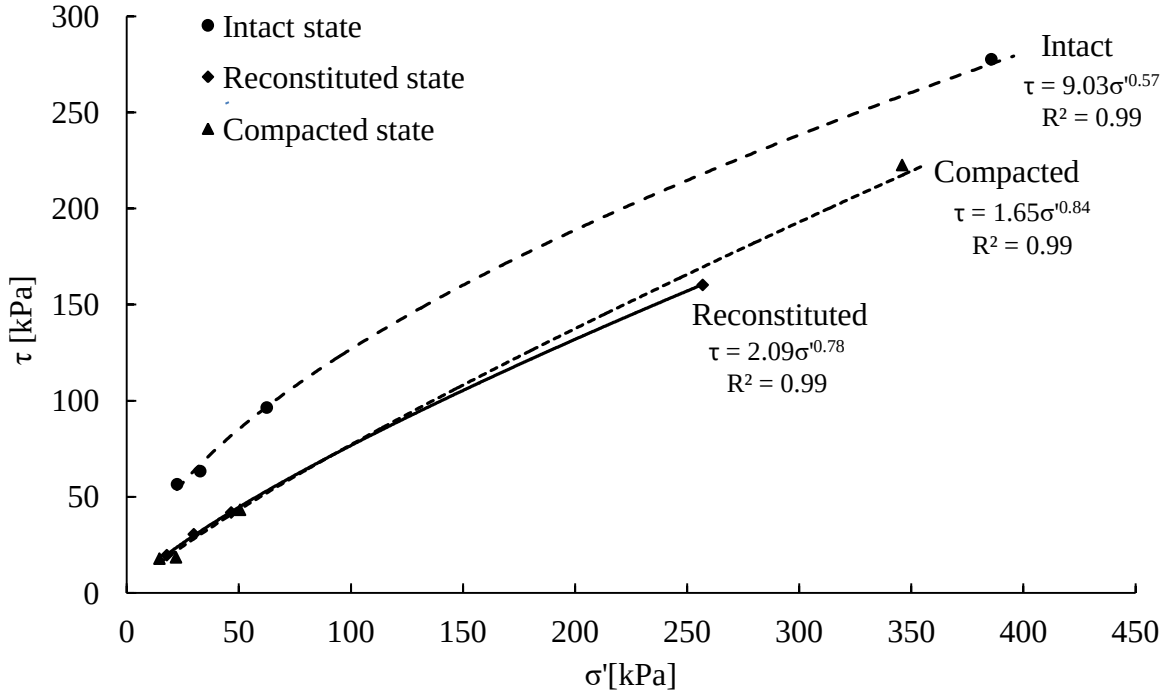
Intact state
Reconstituted state
Compacted state
Intact
τ = 9.03σ'^0.57
R² = 0.99
Compacted
τ = 1.65σ'^0.84
R² = 0.99
Reconstituted
τ = 2.09σ'^0.78
R² = 0.99
τ [kPa]
σ'[kPa]
0
50
100
150
200
250
300
350
400
450

(d)

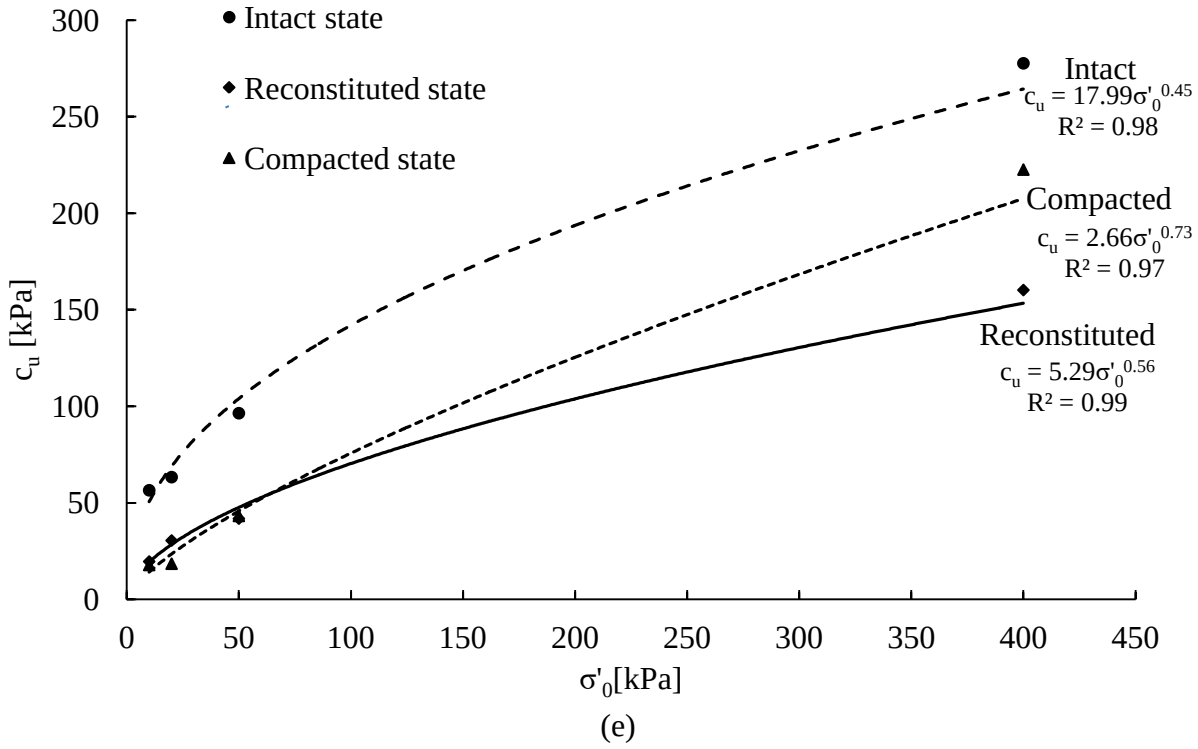

(e)

Figure 6.1. Undrained effective stress paths and strength envelopes for Izumi clay (a) Intact state (b) Reconstituted state (c) Compacted state (d) Effective strength envelopes (e) Consolidated-undrained strength envelopes

Figure 6.1 (b) depicts the undrained effective stress paths for the reconstituted Izumi clay. The reconstituted samples at low stresses (σ'_0=10kPa, 20kPa, and 50kPa) showed initially stiff and dilative behaviour with stress paths travelling rightwards until reaching the peak, followed by strain softening, seemingly converging along a critical state line. The sample at σ'_0=400kPa (OCR=1) showed initially stiff behaviour, followed by strong contractive behaviour with stress path turning leftwards and heading towards a critical state. The non-linear effective strength envelope is drawn by taking the points of maximum stress ratio and expressed by the power law function, as shown in **Figure 6.1 (b)**. The degree of non-linearity of this envelope is b=0.78.

Similarly, the undrained effective stress paths and the effective strength envelope for the compacted Izumi clay are shown in **Figure 6.1 (c)**. The denser compacted samples showed

initially stiff and dilative behaviour until reaching the peak state, followed by strain softening. Comparing the stress paths of the compacted samples with that of the reconstituted samples at low stresses (σ'_0=10kPa, 20kPa, and 50kPa), it seems that the compacted samples exhibited less dilative behaviour, probably due to the lack of full saturation which caused the compacted soil specimen compressible and eventually absorbed dilation, as indicated by the shape of the stress paths. However, at higher stress (σ'_0=400kPa), the compacted specimen showed more stiff and strain hardening behaviour in comparison to the reconstituted specimen. The stress paths at low stresses are seemingly not consistent; this could be due to the variability of the standard proctor compaction effort in the specimens of different soil layers. The non-linearity of the effective strength envelope is b=0.84, as expressed by the power law function.

The effective strength envelopes and the consolidated-undrained strength envelopes for three different states of Izumi clay are drawn and compared in a single plot, although all the tested samples have different void ratios and OCRs just before shearing, as shown in **Figures 6.1 (d)** and **(e)**. In this absolute scale, it is found that the intact strength and its degree of non-linearity were much higher than the reconstituted (intrinsic) strength, probably due to the presence of natural micro-structure enhancing the strength of heavily overconsolidated intact samples; and the compacted strength was comparable to that of the reconstituted strength at the low stress range, but it became slightly higher towards the higher stress range. The degree of non-linearity of the consolidated-undrained strength envelope for each state is significantly higher than that of the effective strength envelope reflecting the influence of development of excess pore water pressure on the top of already curved effective strength envelope.

Atsuma clay

The tests performed on the soft intact Atsuma clay at low stresses (σ'_0=5, 10, 20 and 50kPa) are in the overconsolidated conditions, while the remaining two tests at the yield stress (σ'_0=96kPa) and higher stress (σ'_0=400kPa) are in the normally consolidated conditions. **Figure 6.2 (a)** shows the undrained effective stress path and the effective strength envelope for the intact Atsuma clay. The stress paths for the intact samples at σ'_0= 5kPa, 10kPa, and 20kPa show initially stiff and dilative behaviour, which is followed by strain softening, whereas at σ'_0=50, 96, and 400kPa show strong contractive behaviour. The degree of non-linearity of the effective strength envelope is *b*=0.86.

Figure 6.2 (b) shows the undrained effective stress paths and the effective strength envelope for the reconstituted Atsuma clay. The undrained effective stress paths at low stresses (σ'_0=10, 20, and 50 kPa) show dilative behaviour, which is followed by strain softening, whereas the stress path at σ'_0=400kPa (OCR=1) shows contractive behaviour, similar to the reconstituted Izumi clay. The degree of non-linearity of the effective strength envelope is *b*=0.85.

Figure 6.2 (c) shows the undrained effective stress paths and the effective strength envelope for the compacted Atsuma clay. The denser compacted specimens exhibited stiff and dilative behaviour, followed by strain softening, similar to the compacted Izumi clay. Slight inconsistency in the stress paths at low stresses can be noticed, this could be probably due to the variability of the standard proctor compaction effort in different layers, as mentioned earlier.

All the effective strength envelopes and consolidated-undrained strength envelopes are presented in **Figures 6.2 (d)** and **(e).** It can be noticed that the effective strength envelopes for three different states converge in a narrow region, whereas significant differences can be seen between the consolidated-undrained strength envelopes, which indicates the influence of the

pore water pressure generation in the differently prepared clay specimens. The degrees of non-linearity of both the effective strength envelopes for three different states are comparable with each other.

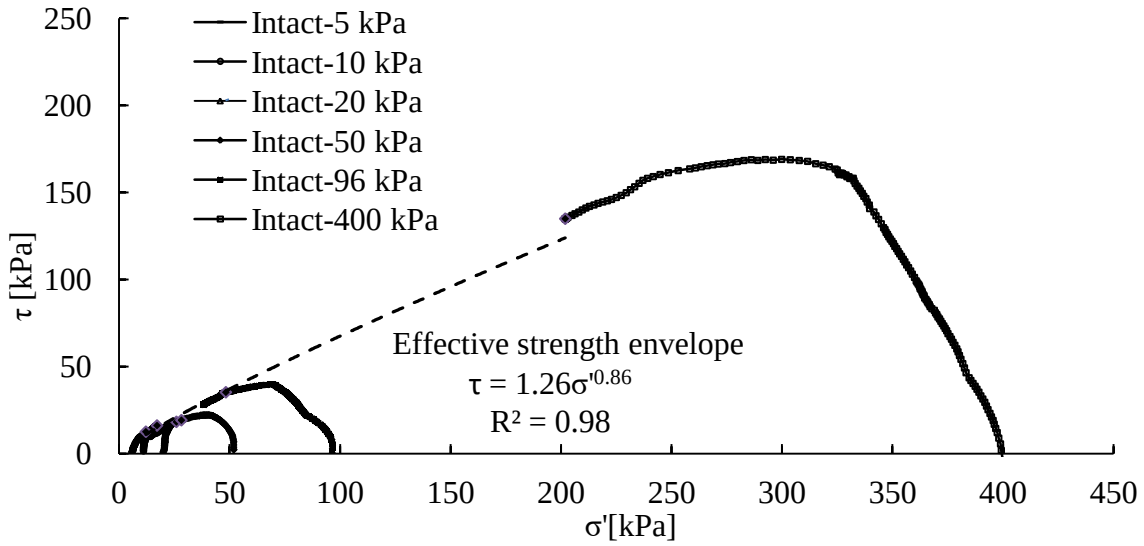

(a)

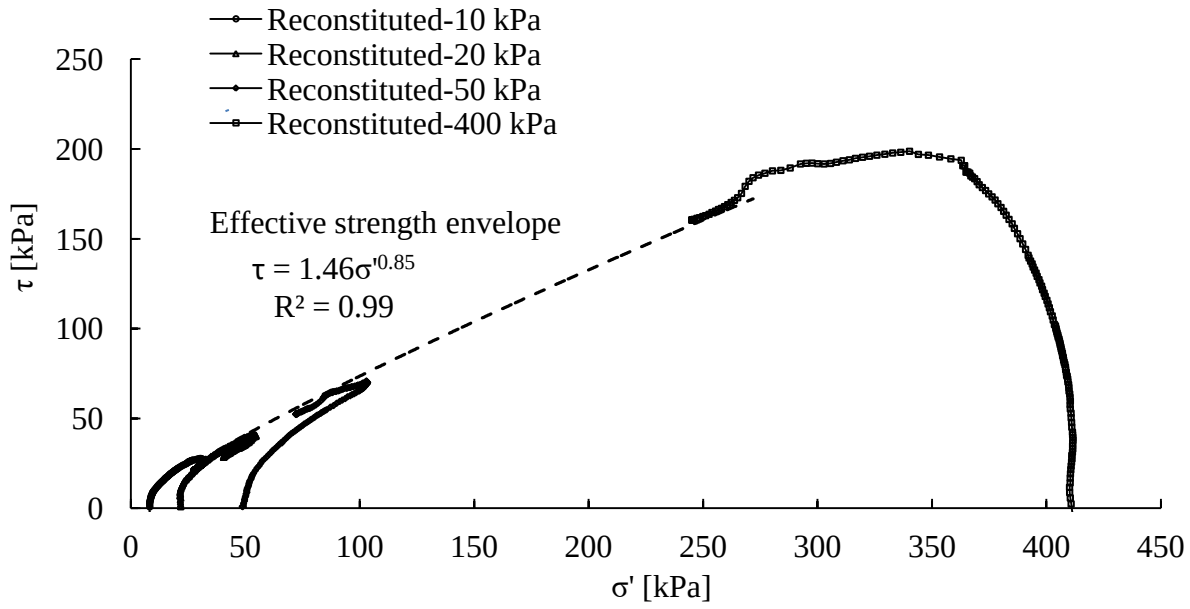

(b)

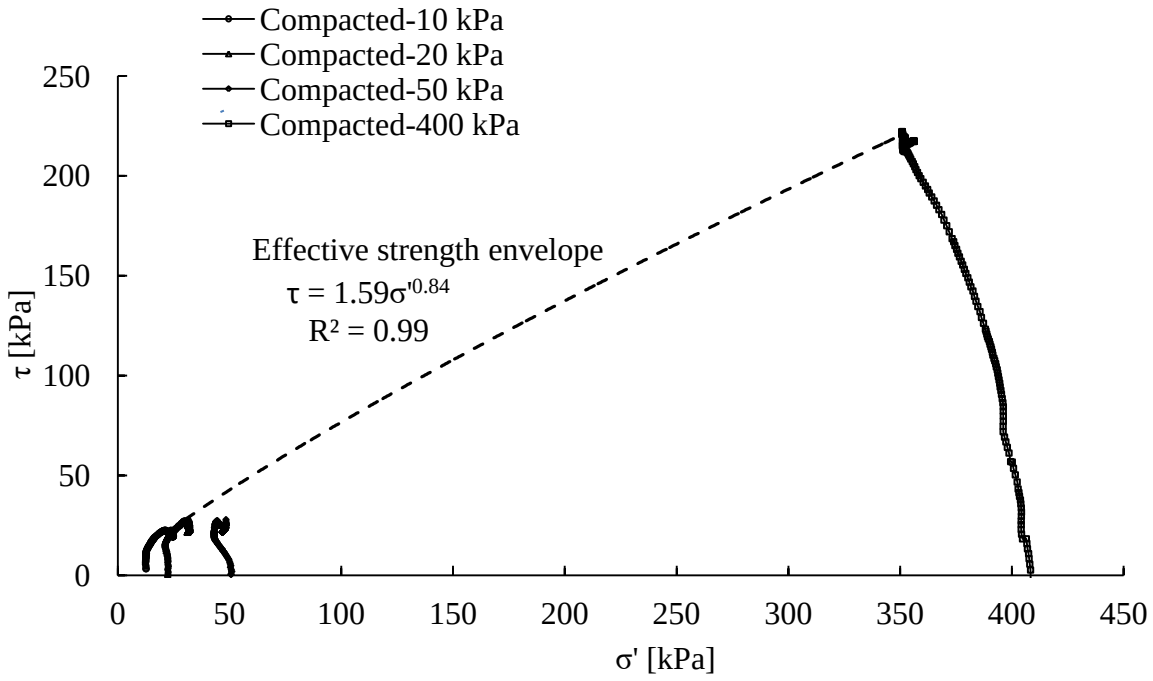
Compacted-10 kPa
Compacted-20 kPa
Compacted-50 kPa
Compacted-400 kPa
Effective strength envelope
τ = 1.59σ'0.84
R² = 0.99
τ [kPa]
σ' [kPa]
0
50
100
150
200
250
300
350
400
450

(c)

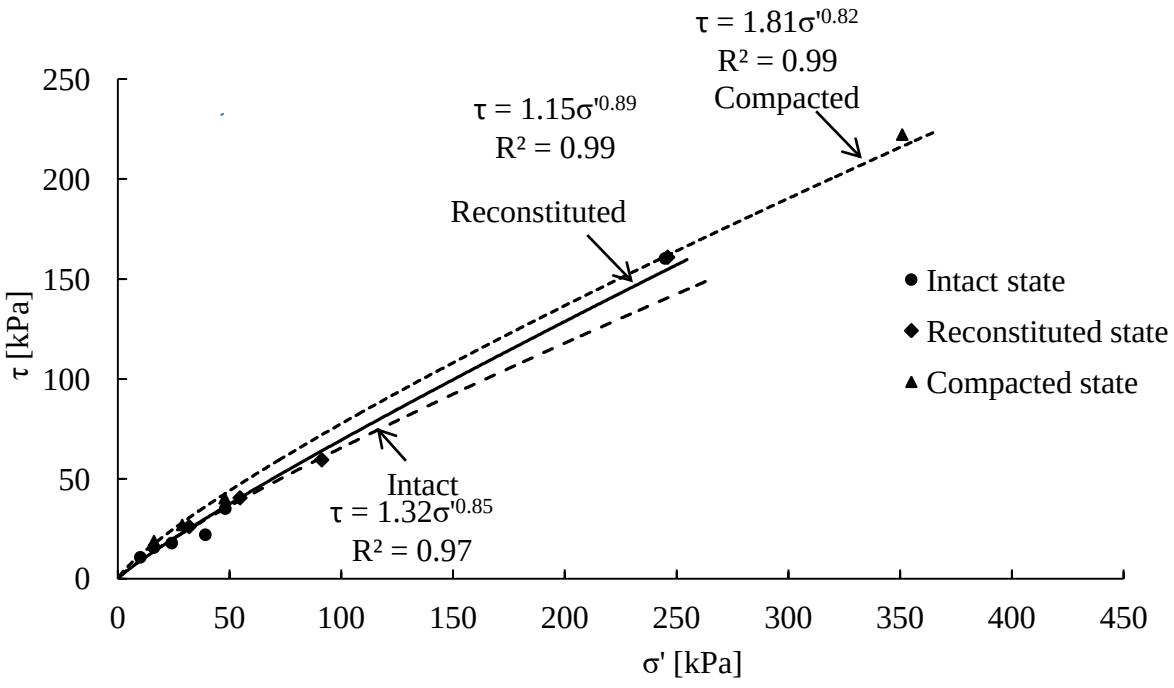
τ = 1.81σ'0.82
R² = 0.99
Compacted
τ = 1.15σ'0.89
R² = 0.99
Reconstituted
Intact state
Reconstituted state
Compacted state
Intact
τ = 1.32σ'0.85
R² = 0.97
τ [kPa]
σ' [kPa]

(d)

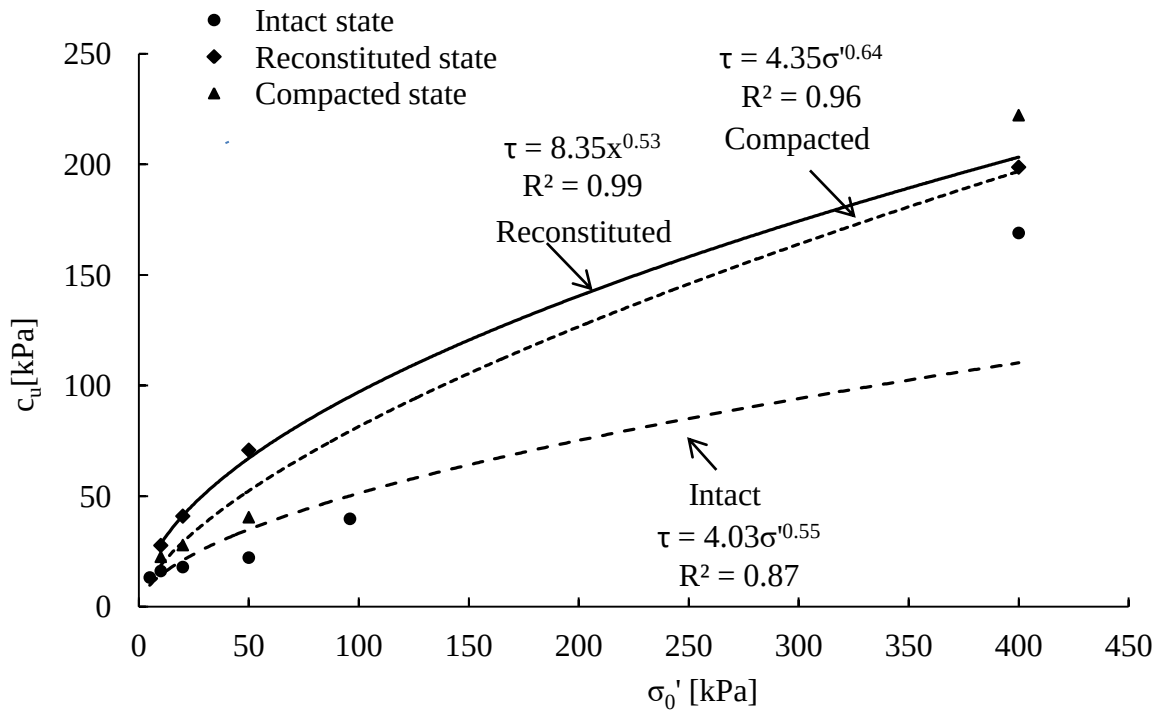

(e)

Figure 6.2. Undrained effective stress paths and strength envelopes for Atsuma clay (a) Intact state (b) Reconstituted state (c) Compacted state (d) Effective strength envelopes (e) Consolidated-undrained strength envelopes

Clay-sand mixed soil

Figure 6.3 (a) shows the undrained effective stress paths and effective strength envelope for the samples of reconstituted clay-sand mixed soil. The stress paths at low stresses (σ'_0=10, 20, and 50kPa) show strong dilative behaviour with a rightward turn close to the failure, and moving up to the maximum displacement of 6mm in contrast to the clays. The effective stress path at higher stress σ'_0=400kPa (OCR=1) shows initially contractive behaviour until reaching the failure, which is followed by strain hardening, and apparently moving towards a potential critical state. This strain hardening behaviour at σ'_0=400kPa after reaching the failure, which is a typical characteristic of coarse-grained soils, indicates a dominant effect of coarse soil particles on the strength behaviour. This behaviour can also be confirmed by the consolidation curves obtained from a constant-rate-of-strain (CRS) oedometer test in which

the coefficient of compressibility is small, nearly equal to 0.2, without a well-defined yield stress, as explained in the later section (**Figure 6.6 (b)**).

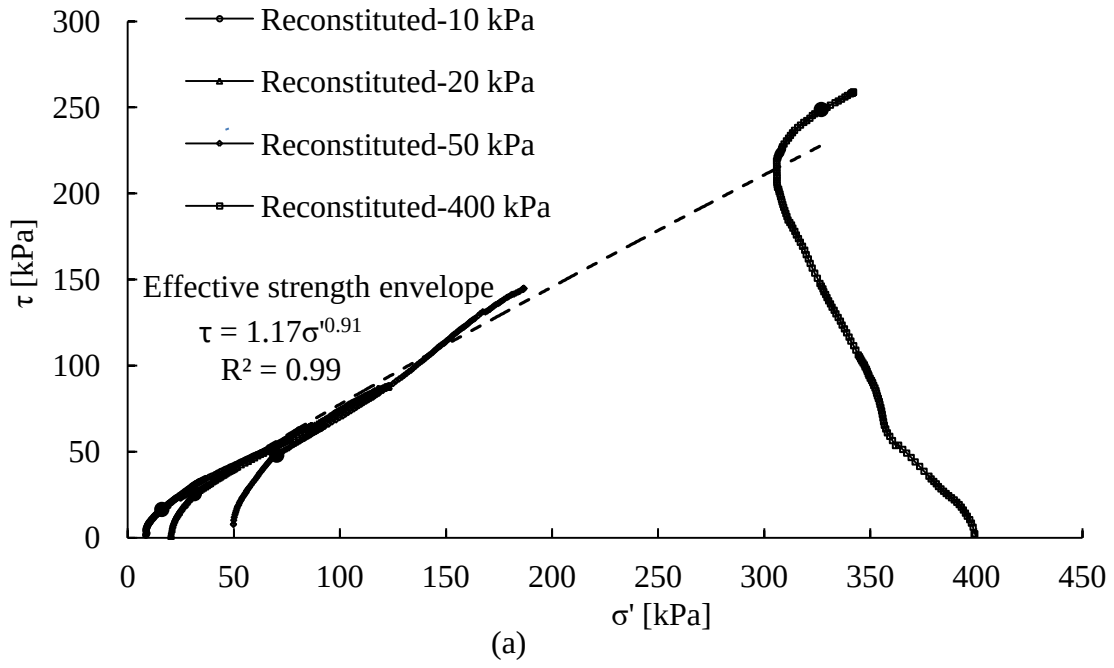

(a)

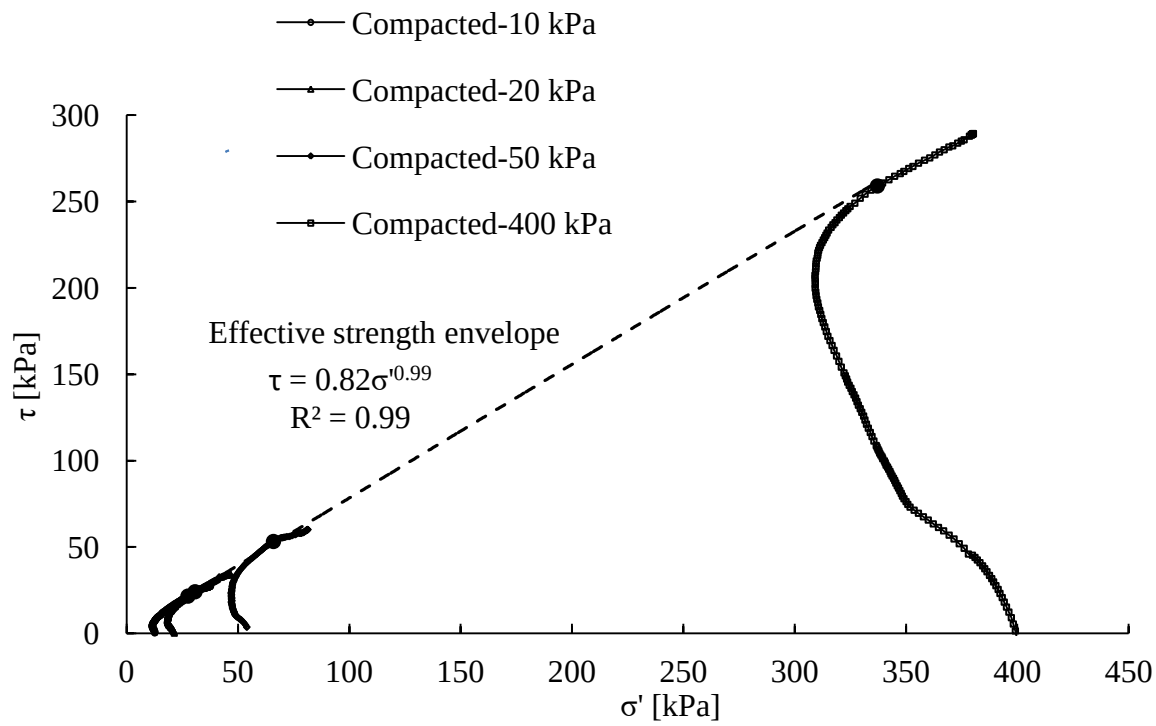

(b)

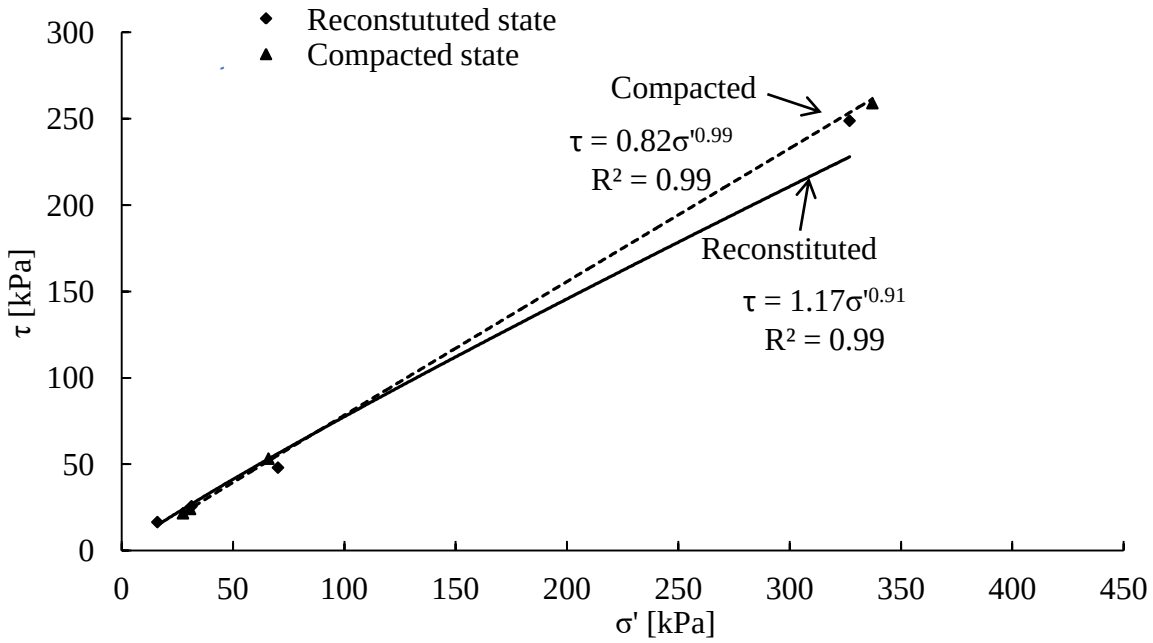

(c)

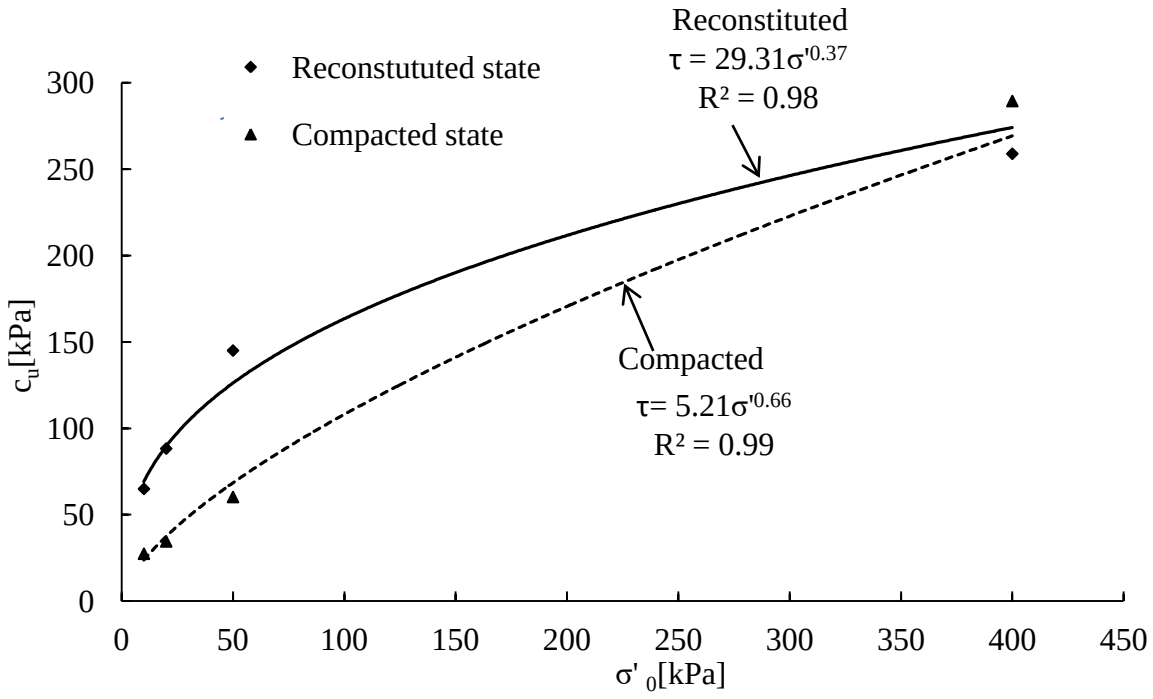

(d)

Figure 6.3. Undrained effective stress paths and strength envelopes for clay-sand mixed soil (a) Reconstituted state (b) Compacted state (c) Effective strength envelopes (d) Consolidated-undrained strength envelopes

Figure 6.3 (b) shows the undrained effective stress paths and effective strength envelope for the compacted clay-sand mixed soil. The stress paths show initially contractive behaviour at low stresses (σ'_0=10, 20, and 50kPa), unlike in the reconstituted samples, which is followed by strong dilation until reaching the maximum displacement of 6mm. The degree of dilative tendency in the compacted samples is broadly similar but it is somewhat more in the reconstituted samples. This could be due to inter-aggregate macro-pores in the compacted specimens and imperfect saturation during testing. The stress path at σ'_0=400kPa shows initially contractive behaviour until reaching the failure, and which is followed by strain hardening, and apparently moving towards a potential critical state, similar to the reconstituted samples.

The effective strength envelopes and the consolidated-undrained strength envelopes for reconstituted state and compacted state are shown in **Figures 6.3 (c)** and **(d)**. The degrees of non-linearity of the effective strength envelopes for both the states are comparable and close to unity, it seems that a conventional linear fitting may be more justifiable than the power law fitting.

6.2.2 NORMALIZED EFFECTIVE STRESS PATHS AND STATE BOUNDING SURFACES

All the samples of different states of soils tested at different consolidation stresses have different apparent overconsolidation ratios and specific volumes just before undrained shearing. To understand the effect of soil structure on the strength behaviour with reference to the intrinsic state in a single framework, such differences can be corrected by normalizing the undrained effective stress paths by the intrinsic vertical equivalent pressure (σ^*_{ve}), as explained in Chapter 2. The intrinsic vertical equivalent pressure is calculated on the intrinsic

compression line (ICL) with respect to the void ratio just before undrained shearing, which is expressed as:

$$\sigma^{*}{}_{ve} = \exp\left(\frac{N - \nu_0}{C^{*}{}_{c}}\right) \qquad \text{Equation 5.1}$$

where, $\nu_0 = 1 + \mathrm{e}_0$, and N and $C^{*}{}_{c}$ are the intercept at 1kPa and the intrinsic compressibility index, and e_0 is the void ratio just before shearing. Constant-rate-of-strain (CRS) oedometer tests were performed on the samples of each state of soils to obtain these parameters on the compression curves.

After the normalization of the stress paths and the effective strength envelopes for different states of soil, the state bounding surfaces for different states can be plotted in a single framework. The normalized power-law strength envelopes constituting the state bounding surfaces can be expressed as:

$$\frac{\tau}{\sigma^{*}_{ve}} = \alpha\left(\frac{\sigma'}{\sigma^{*}_{ve}}\right)^{\beta} \qquad or \quad \tau^{*} = \alpha\,(\sigma'^{*})^{\beta} \qquad \text{Equation 5.2}$$

where, the parameter β gives the degree of curvature, and the parameter α is equivalent to the friction coefficient.

The normalized strength envelope for the reconstituted samples provides in theory an intrinsic state bounding surface, with the curved power-law Hvorslev surface on the dry side of the critical, which can be used as a reference to understand the effect of soil states and structures on the strength of soil (Burland, 1990; Burland et al., 1996).

Izumi clay

Figure 6.4 (a) illustrates the normalized undrained effective stress paths with the dry side of the state bounding surfaces, and the evolution of normalized shear stress with horizontal

displacement for three different states of Izumi clay; the state bounding surfaces are represented by the non-linear power law function, as given in **Equation 5.2.** The degrees of curvature for intact, intrinsic and compacted states are β = 0.51, 0.71, and 0.88, respectively, in which β =1 represents a linear bounding surface. The intact state bounding surface lies well above the intrinsic state showing higher strength and significant degree of non-linearity. This difference can be explained by the role of natural microstructure enhancing the strength and the corresponding degree of non-linearity (Burland, 1990; Burland et al., 1996).

The normalized stress path and state bounding surface for the compacted state lie in a lower normalized stress region in comparison to other two states due to higher density in the compacted samples. An interesting finding here is that the normalized compacted strength was significantly lower than that of the intrinsic one. This indicates that a compacted state can provide strength even smaller than the intrinsic strength when normalized. However, in the un-normalized form, the compacted strength was not necessarily low, as shown in **Figure 6.1**. It should be noted that the two states represent very different void ratios, just before shearing, as shown in **Figure 6.4 (b)**; the compacted state was relatively denser with lower void ratio than that of the reconstituted state. It means that the standard proctor compaction can provide soil strength but it is low for its density or void ratio. In addition, there might also be some elements which could not be normalized in terms of OCR by the equivalent pressure but dependent on the absolute magnitude of stress. This interesting strength behaviour led to observe the meso-scale soil fabrics in both reconstituted and compacted specimens by taking X-ray micro-CT images, which is explained in a later section. **Figure 6.4 (b)** illustrates the compression curves for three different states of Izumi clay, initial direct shear test points and intrinsic compression lines.

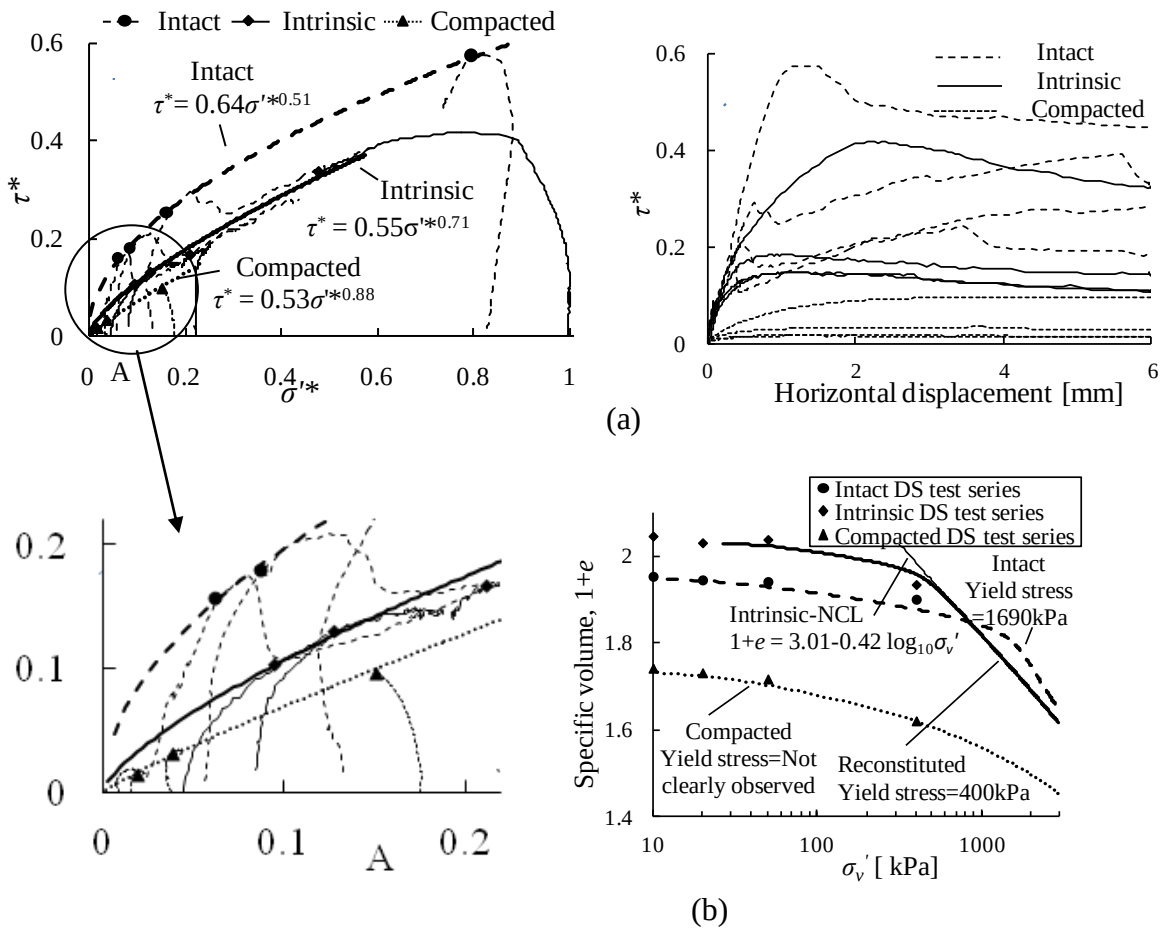

Figure 6.4. (a) Normalized stress paths and state bounding surfaces (b) Compression curves and volume-effective stress states before undrained shearing

Atsuma clay

Figure 6.5 (a) shows the normalized effective stress paths with the dry side of non-linear state bounding surfaces, and the evolution of normalized shear stress with horizontal displacement for three different states of Atsuma clay. Similar to Izumi clay, the non-linear state bounding surfaces for different states are represented by the power law function. The degrees of non-linearity for intact, intrinsic and compacted states are 0.70, 0.74, and 0.78, respectively. The intact state bounding surface lies above the intrinsic state showing slightly higher strength and its degree of non-linearity. This could be due to the natural microstructure enhancing the strength and its non-linearity in the intact state of Atsuma clay. The stress path for intact Atsuma clay from the yield stress (σ'_{vy}) provides the bounding surface on the wet

side of the critical, which is known as Roscoe-Rendulic surface; and for the consolidation above the yield stress, a collapse of yield surface was observed.

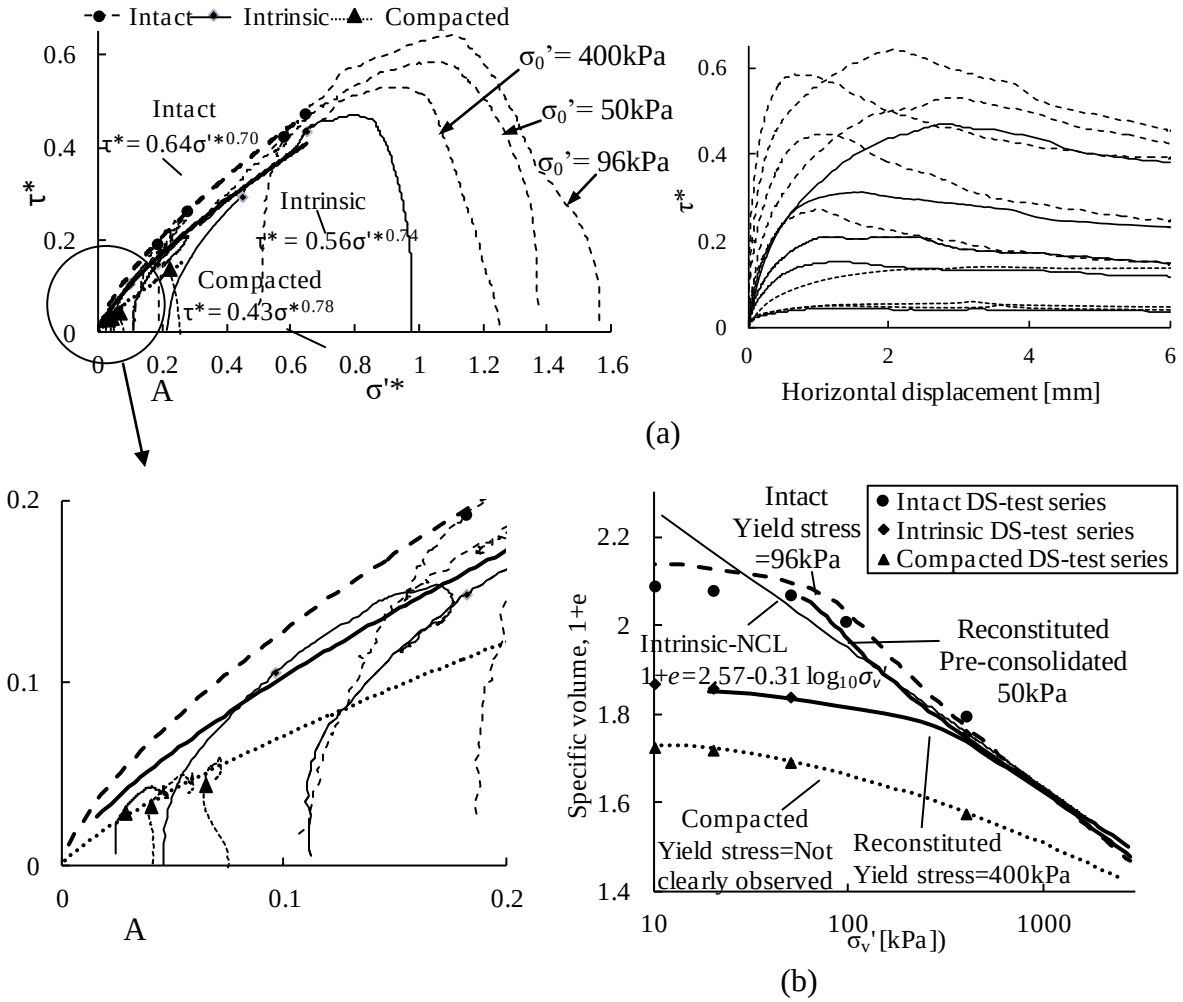

Figure 6.5. (a) Normalized stress paths and state bounding surfaces (b) Compression curves and volume-effective stress states before undrained shearing

On the other hand, the normalized compacted strength was significantly lower than that of the intrinsic one, as indicated by the difference in the state bounding surfaces. This behaviour further illustrates that the compacted state at the same void ratio or OCR was even weaker than the intrinsic state, as demonstrated by the Izumi clay. Observing such behaviour in two uniform plastic clays, an important lesson is that the compacted clays' strength should not be treated as simply 'destructured and densed' strength when field saturated without matric

suction as the compacted strength could be associated with a micro/meso-fabric which is very different from that in more homogenous intact and reconstituted clays. **Figure 6.5 (b)** shows the compression curves, the direct shear test points just before undrained shearing for three different states of Atsuma clay and the intrinsic compression line. The uniqueness of intrinsic compression line was also confirmed by the compression curve of the reconstituted specimen with pre-consolidation pressure of 50kPa.

Clay-sand mixed soil

Figure 6.6 (a) illustrates the normalized stress paths with the dry side of state bounding surface, and the evolution of normalized shear stress with horizontal displacement for different states of clay-sand mixed soil. The non-linear bounding surfaces are represented by the power law function. Comparing the compacted state bounding surface and the intrinsic state bounding surface, the normalized strength and its non-linearity, i.e. β=0.92 and 0.96, respectively, did not show significant difference as both the states had comparable densities, unlike in the clays, indicating the influence of coarser silt/sand particles. The pre-failure deformation characteristics were markedly different between two states, as seen by the effective stress-path shapes, in which the compacted specimens were more compressible at the initial stage of shearing, probably due to inter-aggregate macro-pores and imperfect saturation in the compacted specimens. The X-ray micro-CT images of meso-scale soil fabric in both reconstituted and compacted specimens explains, albeit qualitatively, the reconstituted-compacted bounding surfaces compatibility in the clay-sand mixed soil and in-compatibility in other two clays, which is presented in the later section. It was also observed that a clear critical state was not reached in the clay-sand mixed soil samples during shearing.

Figure 6.6 (b) shows the compression curves and the direct shear states just before undrained shearing for two different states of clay-sand mixed soil and the intrinsic

compression line. While the intrinsic compression line for both Izumi clay and Atsuma clay were well defined, for clay-sand mixed soil it is gentle without a distinct yield point below σ'_v=3000kPa, as usually experienced with the intermediate soil. As all the intrinsic compression line were defined in a similar way, which offers parallel view of three different soils, and the uncertainty in the intrinsic compression line of the clay-sand mixed soil affects the study's conclusions little.

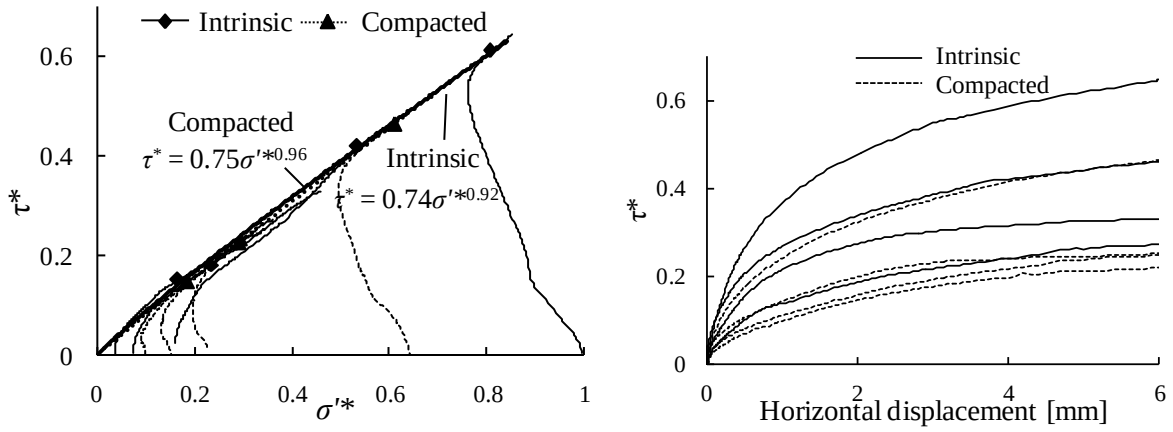

(a)

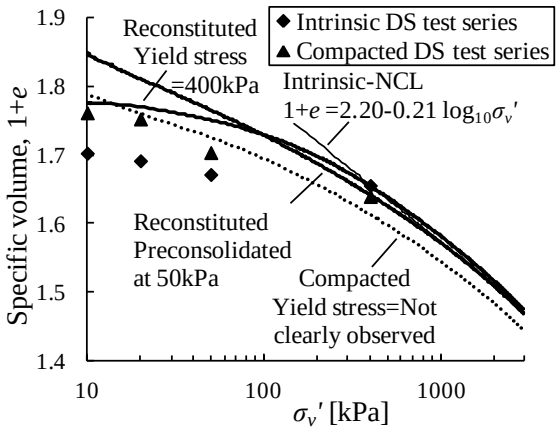

(b)

Figure 6.6. (a) Normalized stress paths and state bounding surface (b) Compression curves and volume-effective stress states before undrained shearing

6.3 OBSERVATION OF MESO-FABRIC FROM X-RAY MICRO CT-IMAGES

Figures 6.7-6.9 show the X-ray micro-CT images of the compacted and reconstituted specimens of Izumi clay, Atsuma clay, and clay-sand mixed soils. Each figure shows the images of horizontal and vertical sections of a specimen with a dimension 70mm in diameter and 70mm high, in which the soil fabric in meso-scale can be seen. With these images, the pattern of density variation within the specimen can be observed (Viggiani and Hall, 2008; Hall et al., 2010), as indicated by different colours (whiter parts indicate higher density). Particularly, in the clay-sand mixed soil specimens, the scattered white colour particles indicate the uniform spatial distribution of coarser particles without segregation and inhomogenization.

Interestingly, the compacted specimens of both clays exhibit numerous large pores forming fissure-like discontinuities with a size as much as 10mm; while they are absent in the reconstituted specimens, as shown in **Figures 6.7** and **6.8.** The occurrence of these discontinuities could be due to air entrapment between clay aggregates during compaction, perhaps aggravated by swelling to low effective stresses as the air in the confined large pores rebounded. By observing the images of compacted bentonite specimens from a scanning electron microscopy (SEM), Wang et al (2014) reported the similar fissure-like large pores as a result of the division of clay particles within the aggregates due to swelling. Observing the pattern of discontinuities in the two pure clays, it seems that the plasticity of clay control forming these discontinuities as they are more conspicuous in more plastic Atsuma clay than Izumi clay. On the other hand, the compacted clay-sand mixed soil specimen shows significantly fewer visible discontinuities in comparison to pure clays, probably due to the

presence of coarser sand particles and resulting lower plasticity in the compacted clay-sand mixed soil specimen, as shown in **Figure 6.9**.

Although these small discontinuities may close due to confining pressure during shearing, they are likely to affect the ultimate shear strength of the compacted clay specimens. Several past researches on investigating the strength behaviour of naturally fissured clays (Gasparre et al., 2007; Nishimura et al., 2007; Vitone and Cotechia, 2011; Hosseini Kamal et al., 2014), it reveals that the normalized shear strength of such fissured clays were similar to or even lower than that measured for the reconstituted states. This is understood by considering the discontinuities or macro-pores represent the local zones of low density with loss of bonding. Most of those observed discontinuities made small angles to the horizontal. This sets a very unfavourable condition for direct shear and hollow cylinder simple shear, which mobilises maximum stress ratio along the horizontal. With these observations, the lower normalized strength of the compacted clays than the reconstituted clays can be explained, though qualitatively, while a further investigation is needed to understand the mechanism of development of these meso-structural discontinuities and their influence on the ultimate strength quantitatively.

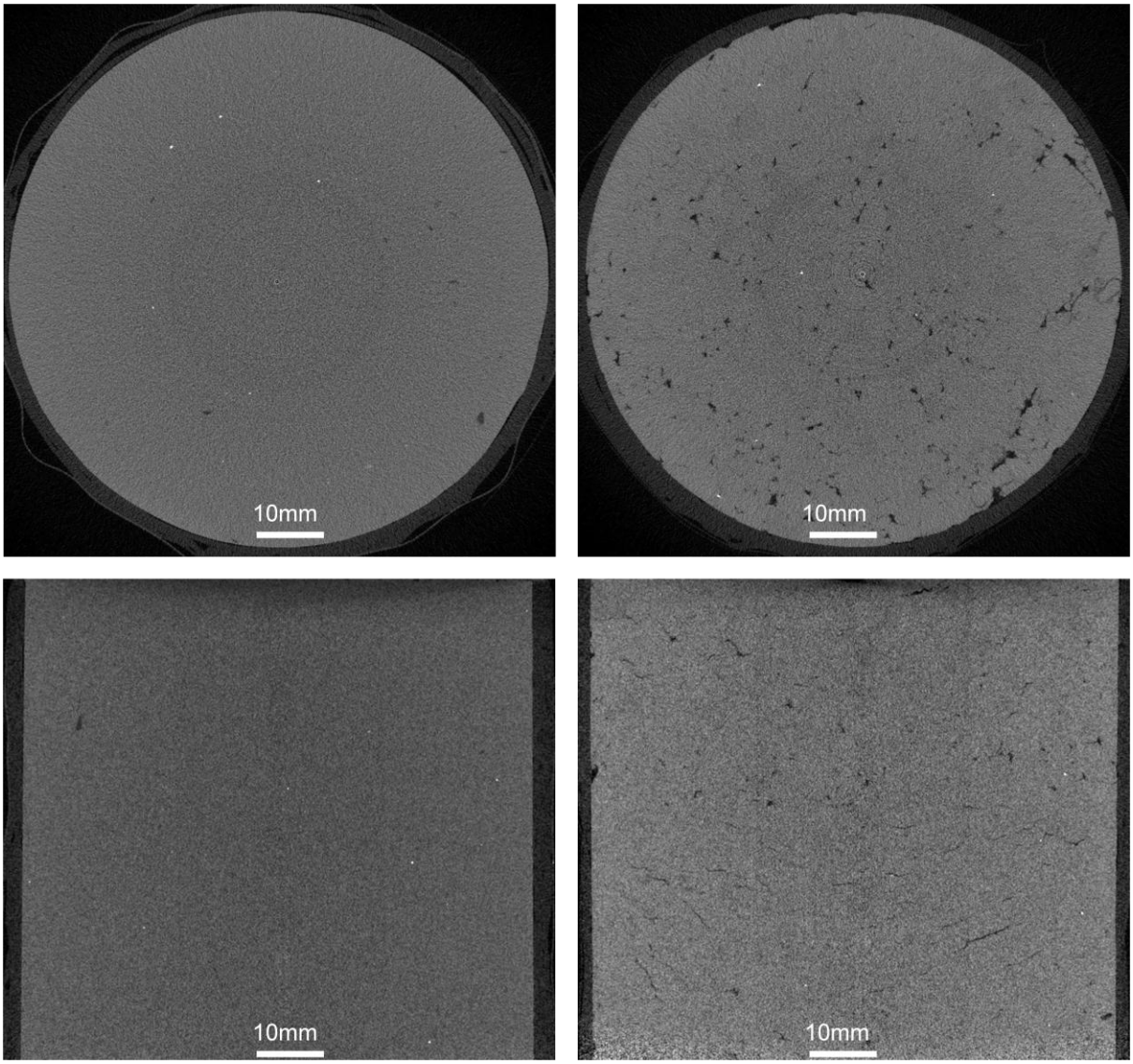

(a) (b)

Figure 6.7. X-ray micro-CT images for Izumi clay (a) reconstituted state (b) compacted state

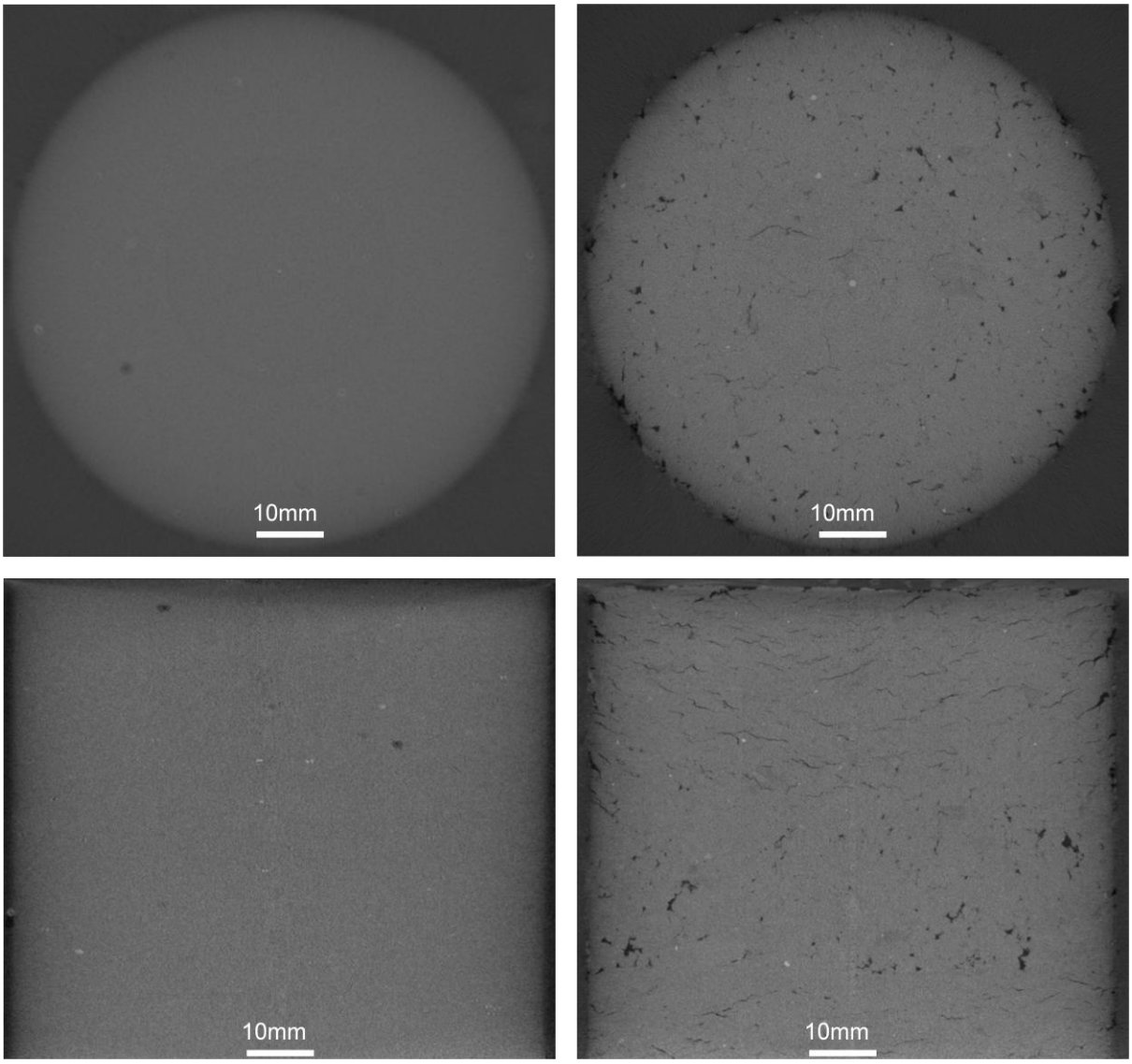

(a) (b)

Figure 6.8. X-ray micro-CT images for Atsuma clay (a) reconstituted state (b) compacted state

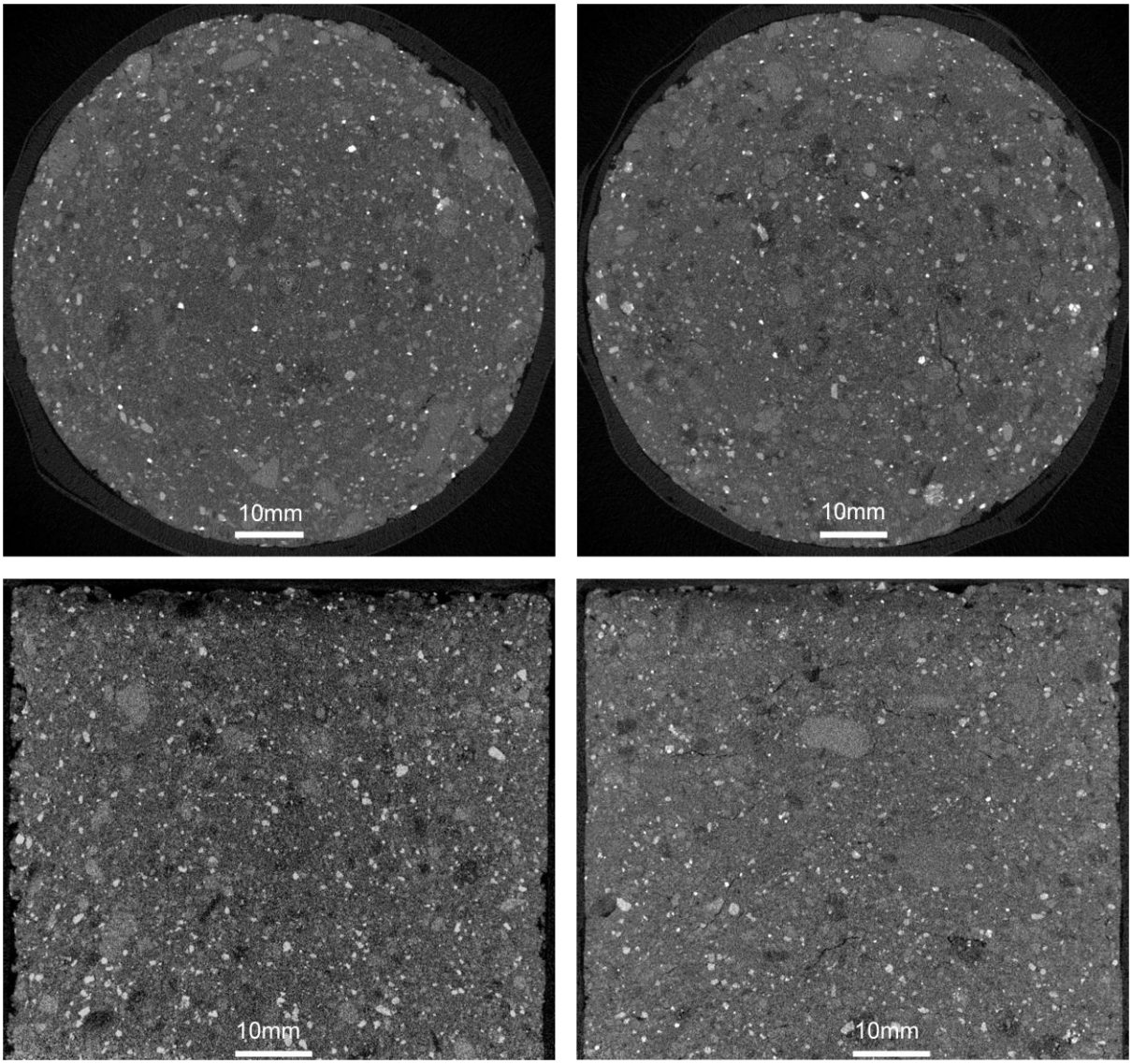

(a) (b)

Figure 6.9. X-ray micro-CT images for clay-sand mixed soil (a) reconstituted state (b) compacted state

6.4 REAPPRAISAL OF DIFFERENT STRENGTH CRITERIA

To derive the effective stress and total stress strength parameters for different states of tested soils at low to medium effective stresses, the linear Mohr-Coulomb strength criterion and non-linear power-law strength criterion are used at different stress ranges. In addition, the undrained strength expression proposed by Mitachi and Kitago (1976) is also reappraised for the intact and reconstituted clay specimens sheared at different overconsolidation ratios.

6.4.1 MOHR-COULOMB FAILURE CRITERION

Application of the Mohr-Coulomb (M-C) failure criterion to represent the shear strength of soil is simple, but the strength parameters are strongly dependent on the stress range chosen, particularly the apparent cohesion at a low stress range, which greatly affects the slope stability analysis results, usually put a significant coverage in the design codes and research papers. It is therefore important to determine such parameters with the strength envelopes based on the stress range in a field. As this study focuses on the shallow slope stability analysis, the low stress range between 10kPa and 50kPa is more appropriate to derive the linear M-C strength parameters. In addition, the strength parameters derived from a higher stress range between 50kPa and 400kPa, although only two points are available, are used for the comparison purpose. All the linearly approximated M-C effective stress strength and total stress (consolidated-undrained) strength parameters in both stress ranges are listed in **Table 6.1**.

Comparing the M-C strength parameters for two different stress ranges, they are different for all the states of tested soils. The differences are more significant for the intact Izumi clay. In which, as both stress ranges lie in the overconsolidated condition, the angle of internal friction in the low stress range of 10-50kPa is higher by 1.5 times than that from the higher stress range of 50-400kPa, whereas the cohesion intercept decreases by a factor of two between these two stress ranges. For intact Atsuma clay, the apparent cohesion is significant only in the low stress range, and it is about zero in the higher stress range of 50-400kPa as this range lies in the normally consolidated condition. For the clay-sand mixed soil, the apparent cohesion is very small, close to zero, in terms of effective stress strength, but it is significant and increases from lower to higher stress range in terms of total stress strength, probably due to the presence of coarser soil particles in contrast to both clays.

Table 6.1. Summary of Mohr-Coulomb effective and total stress strength parameters for different states of tested soils

		Stress Range: 10-50 kPa				Stress Range: 50-400 kPa			
Soil	States	$\varphi'(^0)$	c'(kPa)	$\varphi_{cu}(^0)$	c_{cu}(kPa)	$\varphi'(^0)$	c'(kPa)	$\varphi_{cu}(^0)$	c_{cu}(kPa)
Izumi clay	Intact	45.7	32.0	45.6	45.6	29.2	61.4	27.3	70.5
	Reconstituted	37.5	6.6	27.2	17.0	29.4	15.6	18.7	24.9
	Compacted	36.9	4.7	34.2	8.4	31.3	12.6	27.11	17.6
Atsuma clay	Intact	19.9	8.5	12.1	12	33.3	0	21.85	0
	Reconstituted	29.2	8.8	38.3	20.9	33.2	0	16.2	45.0
	Compacted	34.3	7.6	27.3	11.6	30.9	11.6	27.4	14.4
Maizuru C-S soil	Reconstituted	37.3	0	37.9	9.3	37.1	0.7	29.8	19.3
	Compacted	39.5	0	39.7	10.7	37.2	3.2	30.5	23.8

6.4.2 POWER-LAW STRENGTH CRITERION (ATKINSON, 2007)

As explained in the earlier section, the power-law strength criterion has been applied to represent the non-linear effective strength envelopes for all the states of tested soils. The power law strength parameters are summarised in **Table 6.2**. In an un-normalized form, the degrees of non-linearity (b) of strength envelopes for the intact states of two clays are significantly larger than the reconstituted state, probably due to natural microstructure including true inter-particle cohesion in the intact state. The reconstituted and compacted states of all the soils show comparable degrees of non-linearity of the strength envelopes. The degrees of non-linearity of strength envelopes for both the compacted and reconstituted states of the clay-sand mixed soil are significantly lower in comparison to two plastic clays indicating the influence of coarser soil particles on decreasing the degree of non-linearity. In a normalized form, the envelopes representing the non-linear bounding surfaces for different states of soils have already been explained in detail in the earlier section.

Table 6.2. Summary of power law strength parameters in un-normalized and normalized form for different states of tested soils

		Un-normalized form		Normalized form	
Soils	States	A	b	α	B
Izumi	Intact	9.03	0.57	0.64	0.51
	Reconstituted	2.09	0.78	0.55	0.71
	Compacted	1.65	0.84	0.53	0.88
Atsuma	Intact	1.32	0.85	0.64	0.70
	Reconstituted	1.15	0.89	0.56	0.74
	Compacted	1.81	0.82	0.43	0.78
Maizuru C-S soil	Reconstituted	1.17	0.91	0.74	0.92
	Compacted	0.82	0.94	0.75	0.96

6.4.3 UNDRAINED STRENGTH EXPRESSION (MITACHI AND KITAGO, 1976)

The undrained strength expression proposed by Mitachi and Kitago (1976) for overconsolidated soil is applied to the intact and reconstituted states of soils. The expression is in the form:

$$\left(\frac{\tau}{\sigma_0'}\right)_{OC} = \left(\frac{\tau_1}{\sigma_p'}\right)_{NC} OCR^{1-m} \qquad \text{Equation 5.3}$$

They proposed this equation by performing several undrained triaxial tests on the reconstituted clay with OCR less than 10. According to this equation, the relation between the ratio of undrained shear strength (τ) and vertical effective stress before shearing (σ'_0), and the overconsolidation ratio in a logarithmic plot is linear. The study found that the slope of this line was close to 0.8 under isotropic condition. In this study, similar plots are drawn for different states of soils at very high OCRs, as shown in **Figure 6.10**.

The undrained strength of samples during constant-volume direct shearing are assumed as the maximum shear stress on the effective stress paths, and the OCRs were calculated with respect to the yield stress obtained from the CRS oedometer tests. As the dilation continued until the end of shearing in the clay-sand mixed soil, the shear stress corresponding to the maximum horizontal displacement of 6mm was chosen as the undrained strength. The graphs of τ/σ'_0 versus OCR in a log-log scale show linear relations, as shown in **Figure 6.10**. The slopes, which are also defined as parameter (1-*m*), which is related to the compressibility and swelling indices, are listed in Table 6.

Table 6.3. Summary of parameter (1-*m*) for intact and reconstituted states of tested soils

Soils	States	Slope (1-*m*)
Izumi	Intact	0.73
	Reconstituted	0.55
Atsuma	Intact	0.64
	Reconstituted	0.49
Maizuru C-S soil	Reconstituted	0.63

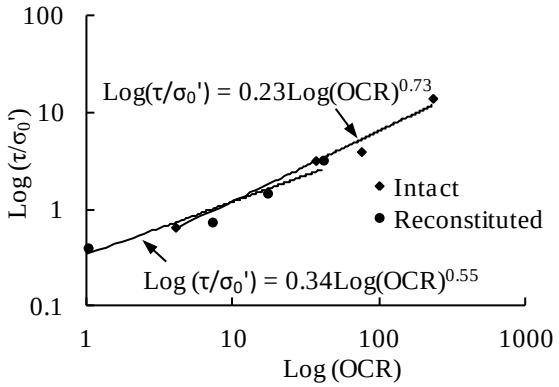

(a)

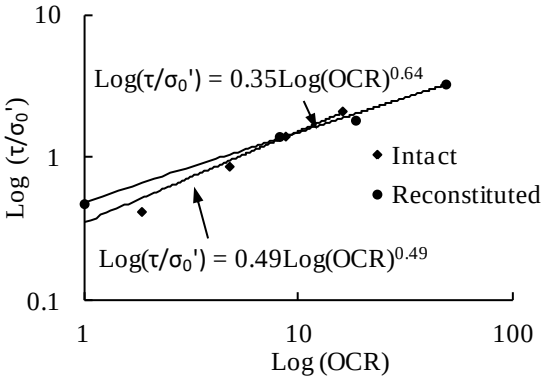

(b)

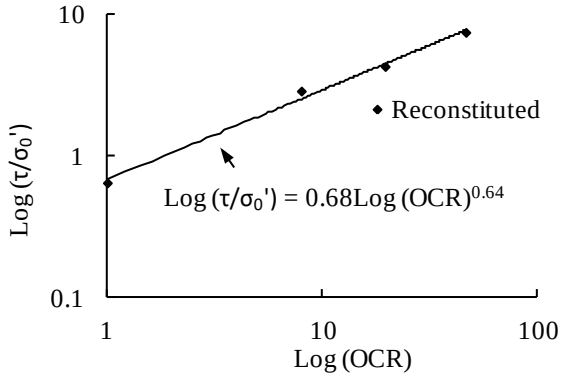

(c)

Figure 6.10. Variation of undrained strength ratio (τ/σ'_0) with OCR for different states of (a) Izumi clay (b) Atsuma clay (c) Clay-sand mixed soils

6.5 HOLLOW CYLINDER SIMPLE SHEAR TEST RESULTS

In this thesis, the selected experimental results from the hollow cylinder simple shear tests are analyzed, interpreted and discussed. The experimental results include undrained effective stress paths plotted in terms of vertical effective stress (σ_z') and torsional shear stress ($\tau_{z\theta}$), the evolution of torsional shear stress ($\tau_{z\theta}$) with torsional shear strain ($\gamma_{z\theta}$), and the evolution of principal stresses (σ_1:σ_3) at different moments during simple shearing.

The analysis of principal stresses in the σ_1:σ_3 plane is studied by the Mohr's stress circles. With the help of these circles, the true cohesion is evaluated for the intact specimens. The comparisons between the stress paths obtained from the constant-volume direct shear tests and the hollow cylinder simple shear tests are carried out in a single plot, even though the rate of shearing, sample size, modes of application of loads are completely different in both types of tests.

6.5.1 UDRAINED EFFECTIVE STRESS PATHS AND PRINCIPAL STRESS STATES

Izumi clay

Figure 6.11 shows the undrained stress paths together with the Mohr's stress circles, and the torsional shear stress-strain curves for different states of Izumi clay. As the intact Izumi clay is very stiff and overconsolidated, slippage along the soil-platen interface before failure was unavoidable, even with three different approaches, i.e. porous stone with short vanes, long vanes and bonding created by the gypsum paste along the interface, as explained in Chapter 4. Comparing the shear strains data measured by local and global sensors, it was identified that some of the data before slippage were reliable. The evolutions of torsional shear stress-strain curves obtained from these three different approaches, with slippage points, are shown in **Figure 6.11 (a)**. The method using gypsum was eventually found to be more reliable than other two methods.

The undrained effective stress path and Mohr's stress circles obtained from the gypsum method are shown in **Figure 6.11 (a)**. The stress path shows very stiff and dilative behavior before slippage. The Mohr's stress circle starts expanding and minor principal stress moves towards a tensile stress region showing the presence of significant true cohesion or bonding due to the natural cementation. The magnitudes of tensile stress of 10kPa and true cohesion of 34kPa were recorded during simple shearing using gypsum method, as shown in **Figure 6.11 (a)**. The potential use of this tensile strength and true cohesion at a low effective stress range would greatly affect the shape of failure envelope, and eventually the stability analysis results of natural cut slopes or embankment made up of bonded soil, such as Izumi clay.

Figure 6.11 (b) and **(c)** show the similar results for the reconstituted and compacted states of Izumi clay. These tests were performed by using the porous discs with long vanes, without any problem of slippage. The stress paths show dilative behavior in both compacted and reconstituted samples. The Mohr's stress circles expand during shearing and eventually converge within a positive effective normal stress zones, in contrast to the intact state.

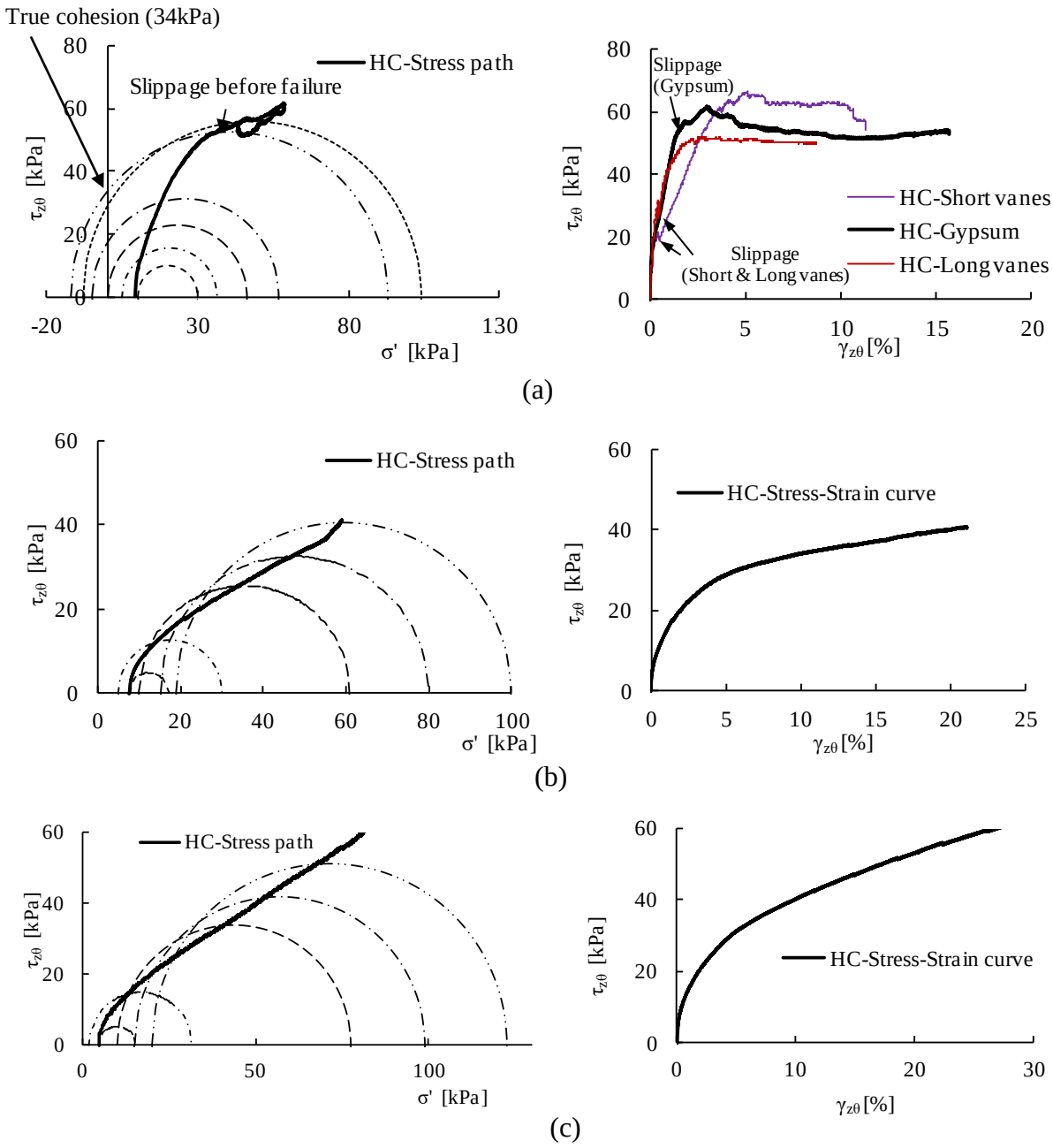

Figure 6.11. Mohr's stress circles and stress-strain curves for Izumi clay (a) Intact state (b) Reconstituted state (c) Compacted state

Atsuma clay

Figure 6.12 shows the undrained effective stress paths with Mohr's stress circles and the evolution of torsional shear stress-strain curves for different states of Atsuma clay. In the figure, the stress path for intact state shows initially dilative behaviour followed by strain softening. In contrast to the intact state of Izumi clay, Mohr's stress circles expand gradually, but remains within the positive effective normal stress zones. The reconstituted and compacted samples showed more dilative and strain-hardening stress paths as in the Izumi clay, as shown in **Figure 6.12 (b) and (c)**.

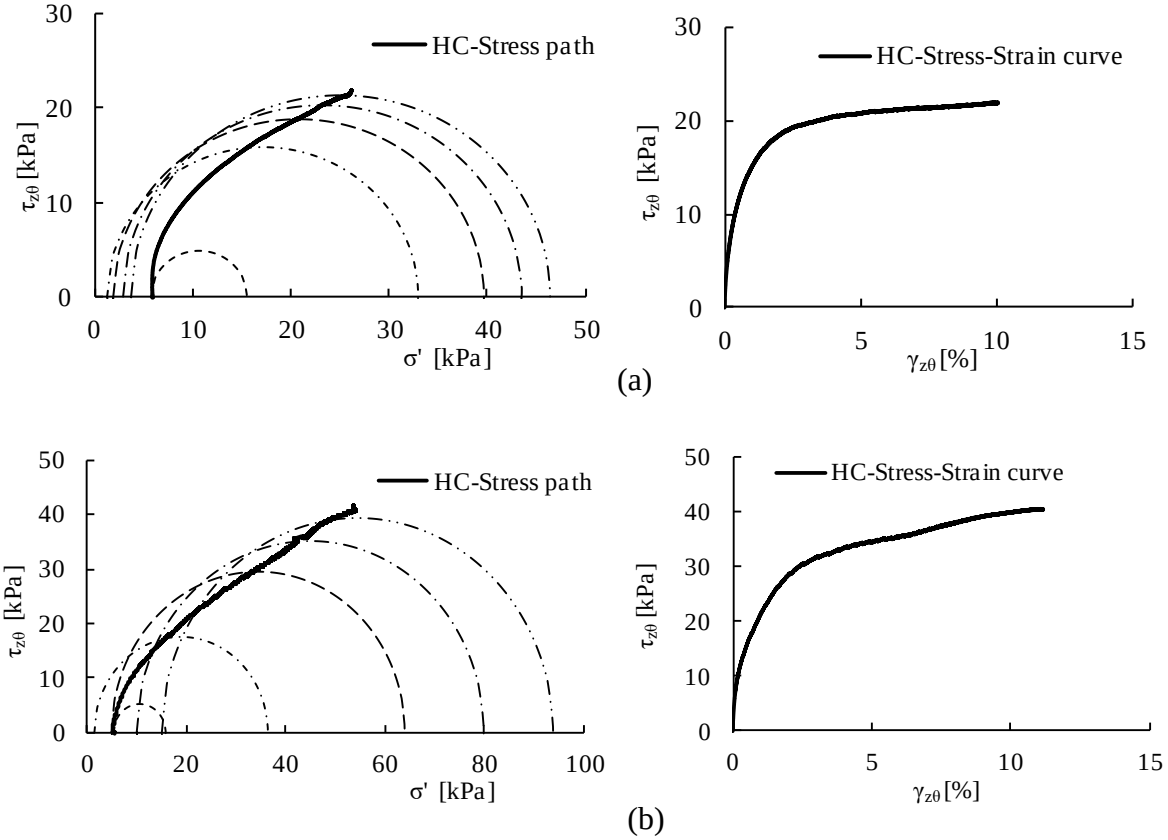

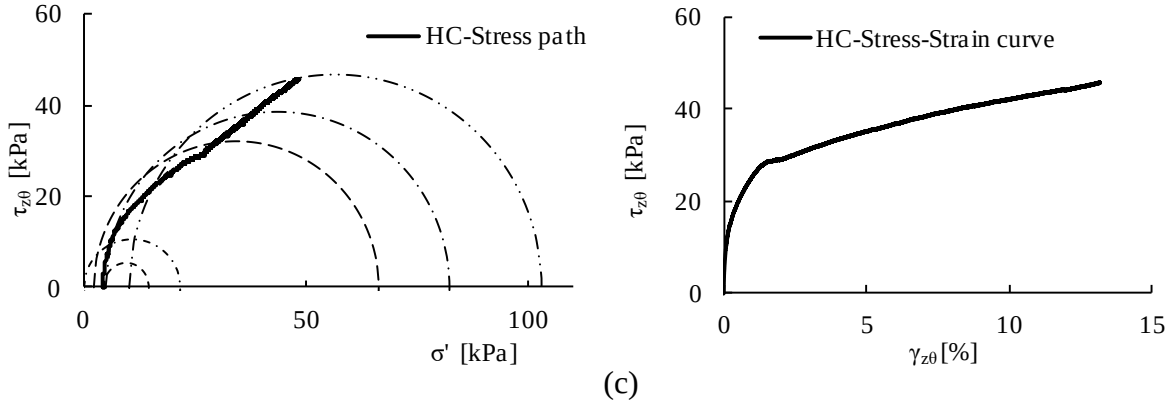

(c)

Figure 6.12. Mohr's stress circles and stress-strain curves for Atsuma clay (a) Intact state (b) Reconstituted state (c) Compacted state

Clay-sand mixed soil

Figure 6.13 shows the undrained effective stress paths and Mohr's stress circles for the reconstituted and compacted states of clay-sand mixed soil. The stress paths for both states show strongly dilative behaviour. In both states, Mohr's stress circles expand gradually but remain within the positive effective normal stress zones.

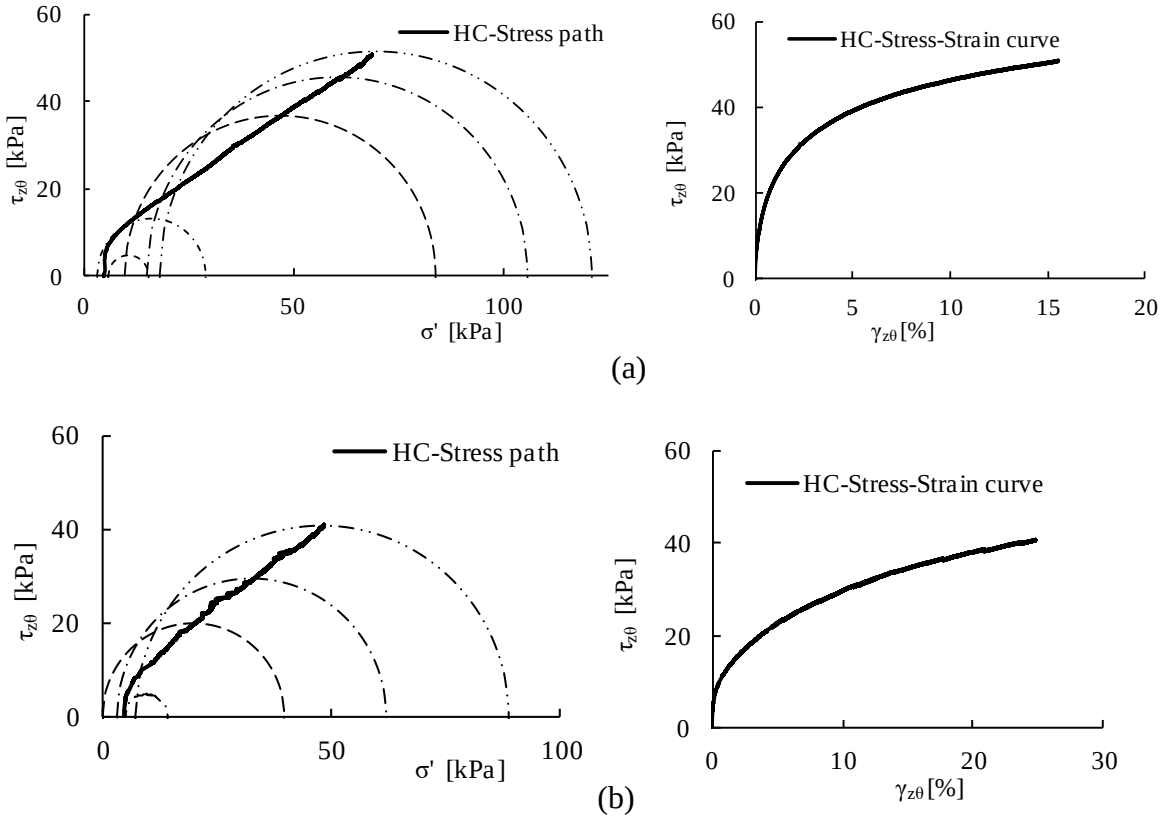

Figure 6.13. Mohr's stress circles and stress-strain curves for clay-sand mixed soil (a) Reconstituted state (b) Compacted state

Rotation of principal stress

As all the HCA tests were performed from triaxial extension modes, by assuming a passive state failure condition. As in the constant-volume direct shear test, the major principal stress was initially in the horizontal direction and the minor principal stress in the vertical direction. Therefore, the angle between the major principal stress and the vertical axis was initially at $\alpha = 90^{o}$. The rotation started from the beginning of simple shearing and eventually converged at $\alpha = 40^{o}$-50^{o}, which is close to the slope of the embankment, as listed in **Table 6.4**. Similarly, the intermediate principal stress factor $b=(\sigma'_2 - \sigma'_3)/(\sigma'_1 - \sigma'_3)$ was initially closer to unity, and eventually converged between 0.35 and 0.45. Similar behavior of principal stresses was also observed by Nishimura et al. (2007) in the London clay.

Table 6.4. Summary of rotation of principal stresses (α) at the ultimate state during simple shearing for different states of tested soils

Soils	States	Rotation α (^{o})
Izumi	Intact	46.8
	Reconstituted	44.9
	Compacted	47.8
Atsuma	Intact	44.1
	Reconstituted	47.2
	Compacted	48.9
Maizuru C-S soil	Reconstituted	41.2
	Compacted	44.7

6.5.2 CONSTANT-VOLUME DIRECT SHEAR VS HOLLOW CYLINDER SIMPLE SHEAR

The undrained effective stress paths obtained from the hollow cylinder simple shear tests and the constant-volume direct shear tests at low effective stresses for different states of Izumi clay, Atsuma clay and clay-sand mixed soil are compared in a single plot, as shown in **Figures 6.14-6.16**. The tests on the intact Izumi clay was performed with three different specimen-platen coupling arrangement, all tests eventually suffered interface slippage and the slippage points were detected by a deviation of external and internal strain measurements, as indicated in **Figure 6.14 (a)**. Comparing the strength behavior of these stress paths, the hollow cylinder stress paths largely conform to the state bounding surface established by the direct shear tests, as explained in the previous section, although they show more dilative behavior, turning further to the right. The more dilative tendency of the hollow cylinder stress

paths at low stresses could be due to the uniform simple shearing throughout the large-sized specimen as indicated by the grid drawn on the outer membrane, while it was localized within the small-sized specimen between two shear boxes in the direct shear tests. It means that the undrained effective stress increased in the direct shear specimen may have been underestimated as the volume compliance in the less intensely deformed parts may have absorbed the dilation to maintain constant-volume condition. This direct shear-hollow cylinder discrepancy is more pronounced in the denser compacted specimen. A further investigation is needed to understand fully such discrepancy and which strength behavior is more relevant to a failure in the field.

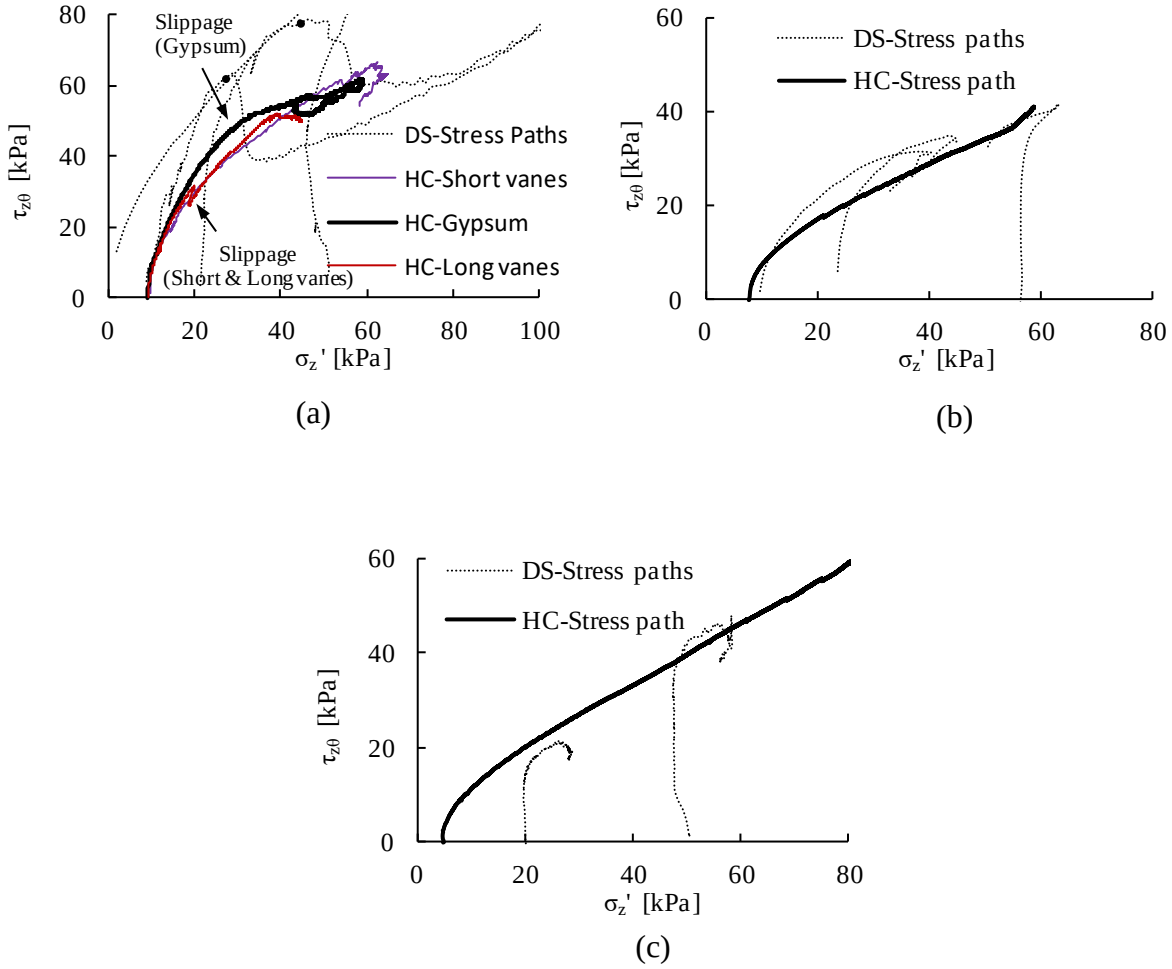

Figure 6.14. Comparison of undrained effective stress paths between direct shear and hollow cylinder simple shear for Izumi clay (a) Intact state (b) Reconstituted state (c) Compacted state

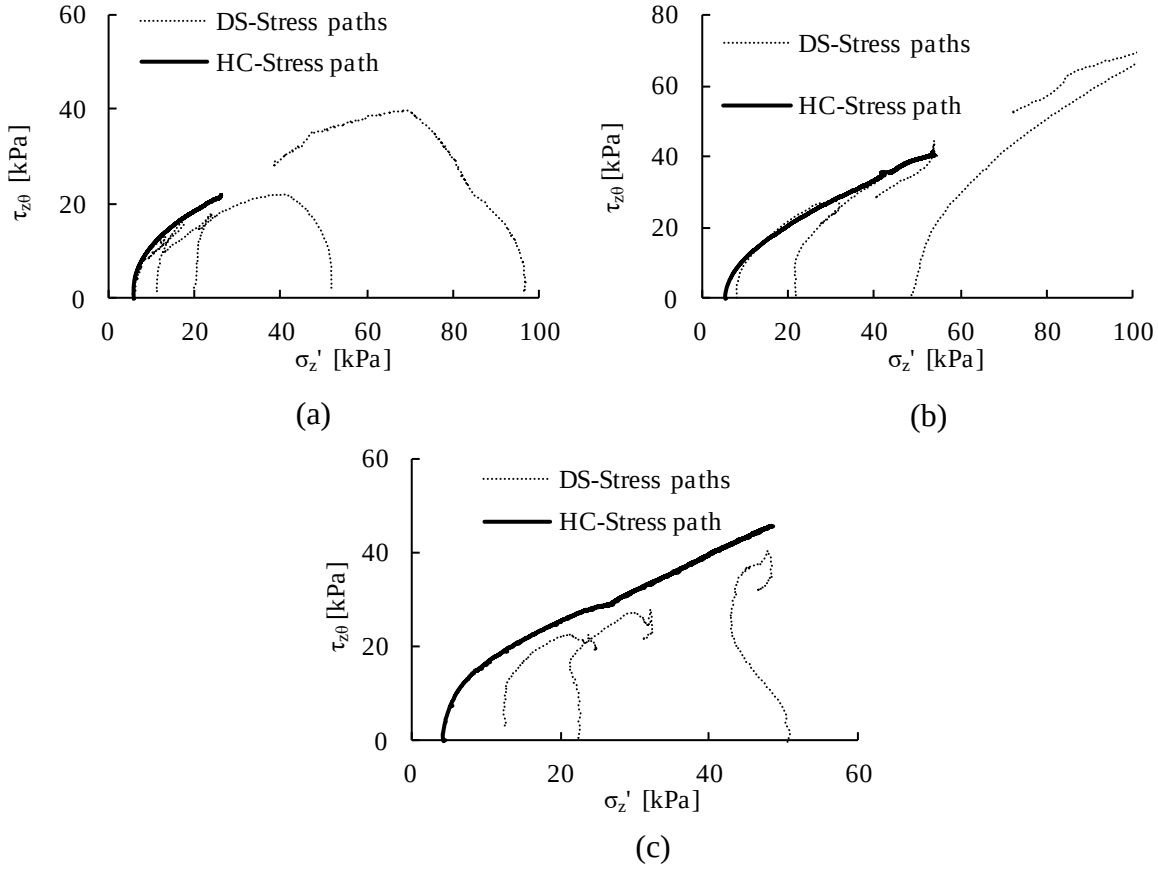

Figure 6.15. Comparison of undrained effective stress paths between direct shear and hollow cylinder simple shear for Atsuma clay (a) Intact state (b) Reconstituted state (c) Compacted state

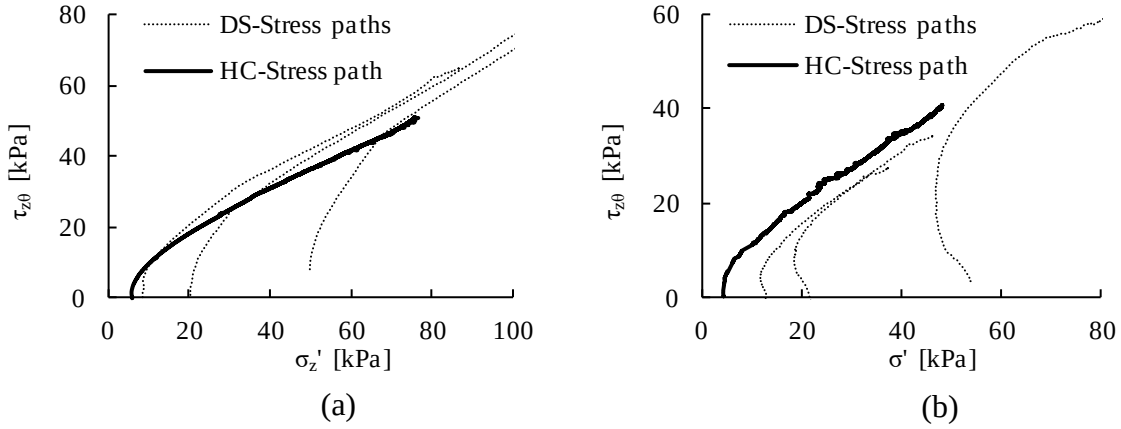

Figure 6.16. Comparison of undrained effective stress paths between direct shear and hollow cylinder simple shear for clay-sand mixed soil (a) Reconstituted state (b) Compacted state

6.5.3 EXPLORATION OF TRUE COHESION

In **Figure 6.11 (a)**, it can be seen that the minor principal stress evolved towards the tensile stress zone with a tensile stress of 10kPa and true cohesion of 34 kPa for the intact Izumi clay. This supports the foregoing discussion assuming cementation to enhance the strength and the non-linearity of power-law state bounding surface, as explained earlier.

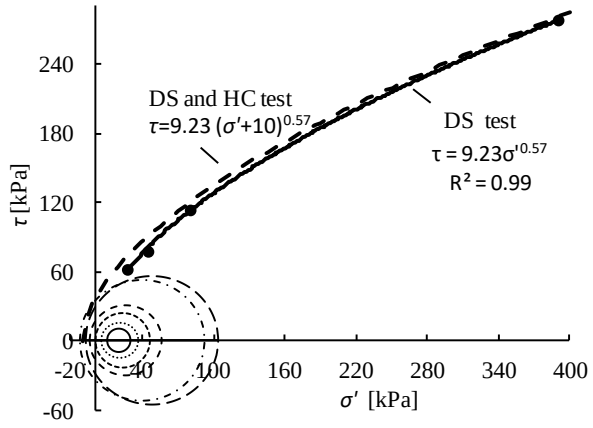

Figure 6.17. Evolution of Mohr's stress circle and strength envelopes for intact Izumi clay

Furthermore, although more experimental investigations are needed, it seems that the power-law failure envelope obtained from direct shear tests can be modified by taking into account of this true cohesion. A simple power law equation, using such limited data points, can be derived including a horizontal intercept (i.e. tensile stress of about 10kPa) with σ', as shown in **Figure 6.17**. This equation is not in a general form for all soils, but for intact Izumi clay there is a good agreement between hollow cylinder Mohr's stress circle and power-law strength envelope from direct shear tests. Observing the overall shearing behaviour of all three states of Izumi clay, the state bounding surfaces for intact Izumi clay can be constructed by extending towards the tensile stress zone, as shown in **Figure 6.17**.

CHAPTER 7 CHARACTERIZATION OF NEAR-SURFACE STRENGTH OF RIVER DYKE SLOPES: RESULTS AND DISCUSSIONS

7.1 INTRODUCTION

In this chapter, results on hydraulic and mechanical behaviour of river dykes obtained from the field and laboratory experiments are interpreted and discussed. The field experimental results include the cone penetration resistance obtained from the portable static and dynamic cone penetrometer tests on the aged (3-5 years) Maizuru and recently-constructed Higashinosato river dyke embankments, which particularly aim to understand the temporal and spatial variations in soil strength in the near-surface zone of embankment slopes, as explained in Chapters 1 and 3. In order to investigate the spatial variation in soil strength across the embankment slopes, the slopes have been divided into three different regions along the transverse direction of the embankment slope, i.e. top, mid, and toe. The long-term spatio-temporal variation in soil strength of the Maizuru embankment slope is eventually assessed with respect to the laboratory (as)-compacted strength.

The laboratory experimental results include the stress-strain curves and the undrained effective stress paths of the compacted clay-sand mixed soils, obtained from the consolidated-undrained triaxial tests. The compacted samples were tested in both laboratory (as)-compacted state (Higshinosato, Ebetsubuto, and Maizuru soils) and field compacted (undisturbed) state (Maizuru soil). To eliminate the effect of different specific volumes and apparent OCRs before undrained shearing of the specimens, and understand the strength behaviour of different states in a single framework, all the stress paths and strength envelopes are normalized by the critical equivalent pressure on the critical state lines, unlike the

intrinsic equivalent pressure as it was difficult to obtain the well-defined normal compression line within a limited vertical effective pressure of 3000kPa for the clay-sand mixed soil, as explained in Chapter 6. To represent the strength envelopes at a low stress range, a non-linear power-law failure criterion is used and the strength parameters are derived.

Finally, results of climatic and hydraulic responses obtained from the field monitoring and the numerical simulation are interpreted and discussed. Correlations are considered between the penetration resistance obtained in the Maizuru river dyke slope and the laboratory-compacted model ground and the undrained strength obtained from the consolidated-undrained triaxial tests, using both the measured and simulated pore water pressure at different depths.

7.2 IN-SITU STRENGTH VARIATIONS FROM PENETROMETER TESTING

7.2.1 PORTABLE STATIC CONE PENETROMETER TESTS

Soil strength in the near-surface zone of the Maizuru river dyke embankment slope was measured by performing the monthly portable static cone penetrometer tests at seven different locations in the transverse direction. The soil strength is expressed in terms of cone penetration resistance, as shown in **Figure 7.1**. The figure shows monthly depth profiles of the cone penetration resistance at the seven different locations across the slope according to plan I (at 1m interval) and plan II (at 3m interval). Together with the monthly depth profiles, lines representing the maximum cone penetration resistance, q_{cmax} = 2.87MPa, are drawn. These lines from two different plans are approximately parallel to the slope surface and converge into a narrow region indicating a similar result without significant spatial variation in soil strength along the longitudinal direction of the embankment slope.

Figure 7.2 shows the depth profiles of average penetration resistance (q_c) obtained in the Maizuru embankment slope together with the limited data from the Higashinosato embankment slope and the laboratory-compacted model ground (calibration tests). The average penetration resistance in each region (i.e. top, mid and toe) was calculated by taking an arithmetic mean of the cone penetration resistances measured by all the tests performed at the same location (i.e. three tests were performed at each location). In the Maizuru embankment slope, the soil strength increased gradually with depth in each region down to 0.5m depth, and the top-region showed higher strength than the other two regions at a same depth illustrating a small but statistically significant spatial variation in strength. All the depth profiles of penetration resistance obtained over a year converge into a narrow region. This indicates that the soil strength showed a small temporal variation due to monthly and seasonal changes in pore water pressure, which was not as significant as expected because the pore water pressure increased close to hydrostatic pressure during snow melting and heavy rainfall events. When comparing the soil strength in the near-surface zone of the Maizuru embankment slope with that of the recently-constructed Higashinosato embankment slope and the laboratory-compacted model ground at 0.4-0.5m depth, the Maizuru embankment showed consistently higher strength than both of them. On the other hand, the strength of Higashinosato embankment was comparable with the strength of the laboratory-compacted Ebetsubuto soil at initial compaction water content of $1.30w_{opt}$.

As all the monthly profiles of penetration resistance in each region in the Maizuru embankment slope increases gradually with depth and show consistently higher strength close to 0.4-0.5m depth than both the Higashinosato embankment and the laboratory-compacted Ebetsubuto soil, as shown in **Figures 7.1** and **7.2**., this interesting result led to carry out an investigation on the undrained strength behaviour of soil in this depth with

reference to the freshly-compacted soil by performing a series of triaxial tests, which is explained in a later section. When undisturbed sampling was carried out at the mid-region of the slope along this depth for the triaxial testing, after removing the top surface soil, the soil was seen to change its colour from brown to navy-greyish indicating a boundary of oxidized and un-oxidized soils. As the surface soil has already received a few wetting-drying cycles of seasons (about 5 years) after the construction, the oxidization front may have reached around this depth. On the other hand, Mitchell and Soga (2005) has highlighted that the soil at shallower depth of the slope may experience overconsolidation as a result of soil desiccation during prolong drying period. Stirling et al. (2017) has reported that a desiccated crust with low permeability soil in the near-surface soil can develop as a result of prolonged drying.

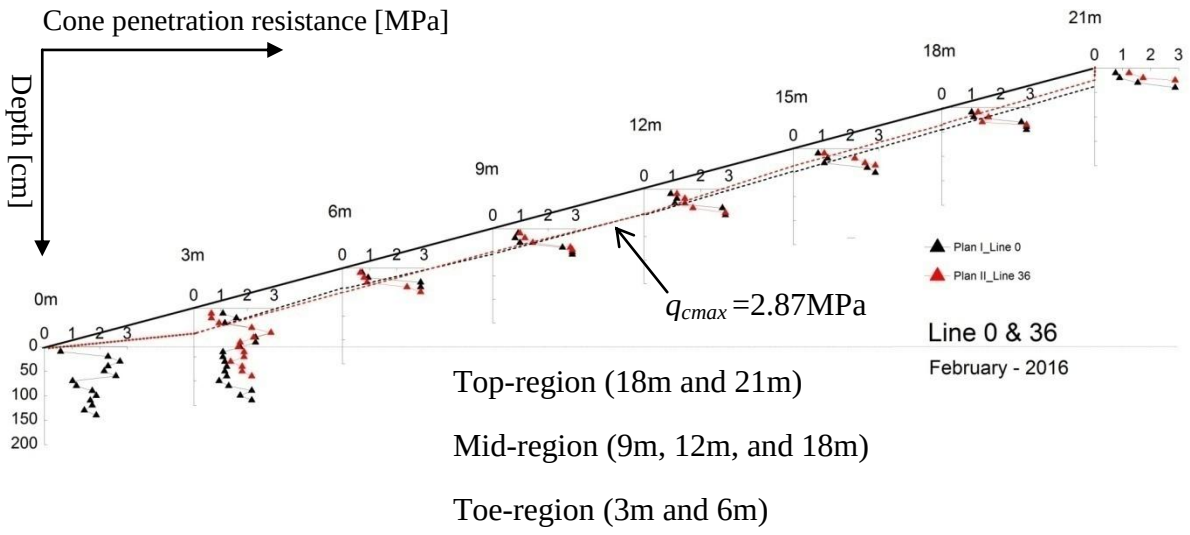

Figure 7.1. Results from static cone penetrometer tests in different regions along the slope in Maizuru embankment slope

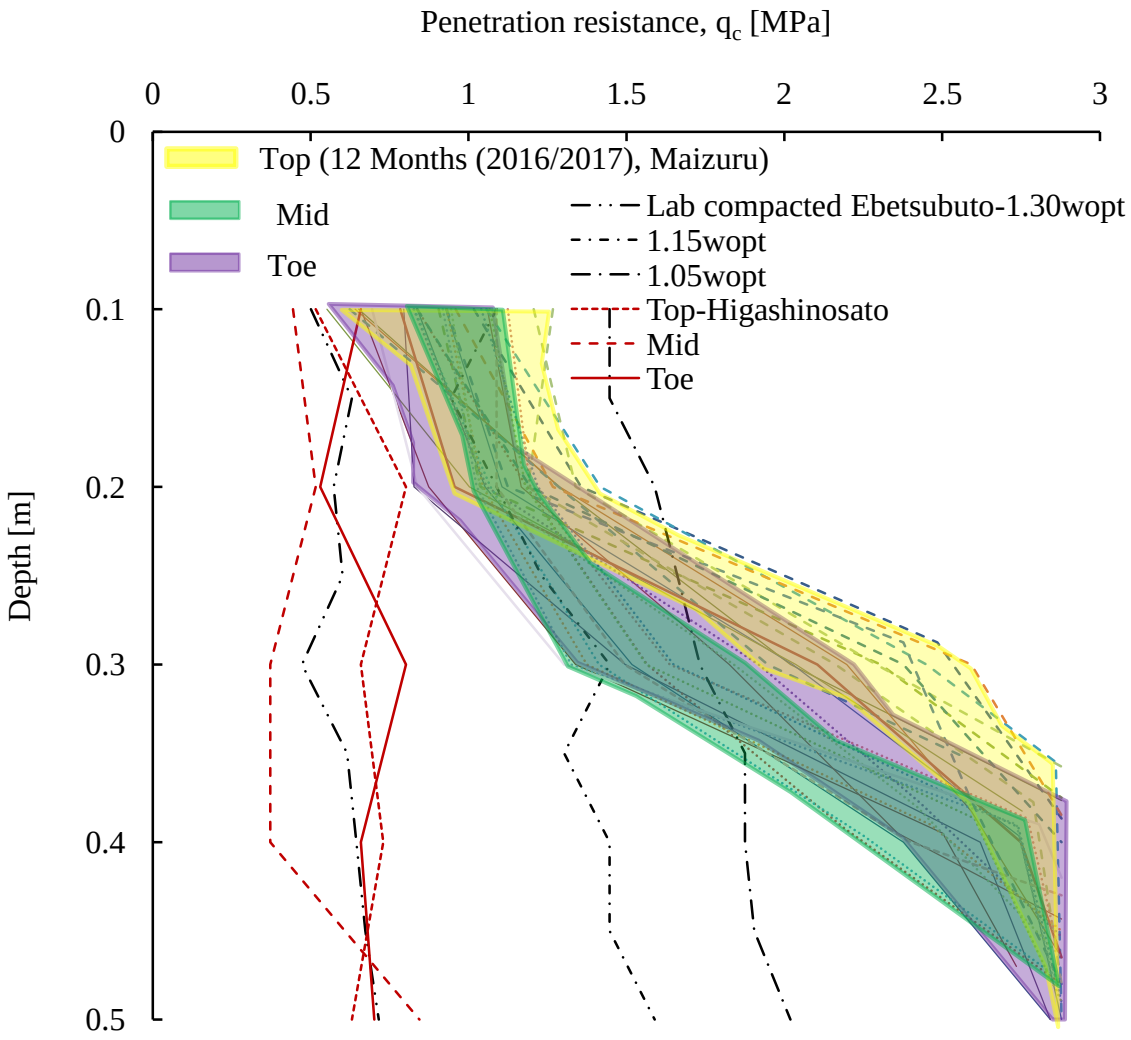

Figure 7.2. Depth profiles of penetration resistance in Maizuru embankment slope, Higashinosato embankment slope and lab-compacted Ebetsubuto soil

7.2.2 PORTABLE DYNAMIC CONE PENETROMETER TESTS

The results obtained from the portable dynamic cone penetrometer tests performed in the Maizuru and Higashinosato embankments at an interval of approximately four months are presented in terms of penetration resistance (number of blow) against depth, as shown in **Figures 7.3**. The shaded portion in the figure indicates the depth of embankment over the base layer. By observing the trends of penetration resistance in the depth profiles obtained over a year in the Maizuru embankment slope, three distinguished pattern of penetration

resistance variations can be seen with respect to the depth i.e. region 1 (0-0.5m), region 2 (0.5-1m), and region 3 (1-5m). In the region 1, between 0 and 0.5m depth, the penetration resistance increases gradually with depth, and conforms well to the corresponding trend obtained from the static cone penetrometer tests (i.e. **Figure 7.2**). In the region 2, between 0.5m and 1m depth, the penetration resistance decreases slightly and remains almost constant forming a neck-shaped profile. In the region 3, between 1m and 5m depth, the penetration resistance increases gradually with depth until reaching a base layer of the embankment, this gradual increment in penetration resistance could be related to the increase in overburden effective stress and significantly lower pore water pressure than the hydrostatic pressure projected from the surface as measured by the field monitoring. It can also be noticed that the penetration resistance increases abruptly in between two embankment layers of different stages of construction, probably due to more compaction effort and the influence of climate which may result in surface layer similar to the current 0.4-0.5m depth. Comparing the trends of increment in penetration resistance between the Maizuru embankment and the Higashinosato embankment, the Higashinosato embankment showed significantly lower strength without showing distinguished pattern of strength variation along the depth as the consolidation of soil was in progress when these tests were carried out. It is also difficult to distinguish the surface soil layer in the Higashinosato embankment.

Observing the results of penetration resistance obtained from both static and dynamic cone penetrometer tests (**Figures 7.2** and **7.3**) in the Maizuru embankment, it can be highlighted that the near-surface zone is characterized with top lower strength soil layer together with the higher strength soil layer at 0.4-0.5m depth. A further research will be necessary to improve the understanding of a progressive development of these layers and their implication in the shallow slope stability analysis of embankment slopes.

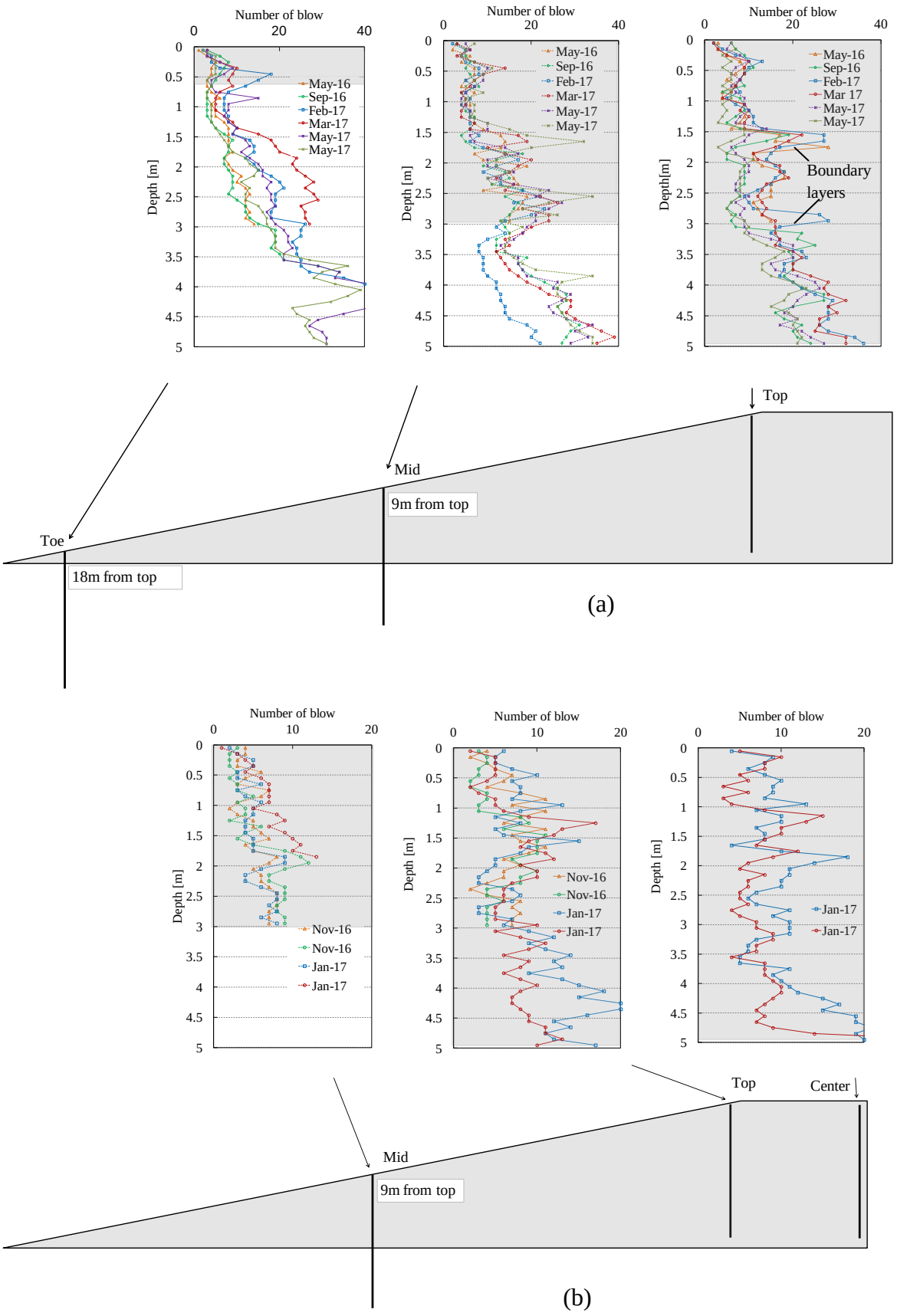

Figure 7.3. Depth profiles of penetration resistance from dynamic cone penetrometer tests (a) Maizuru embankment (b) Higashinosato embankment

7.3 UNDISTURBED SOIL SAMPLING, MEASUREMENTS OF IN-SITU WATER CONTENTS AND PARTICLE SIZE DISTRIBUTIONS

The undisturbed soil sampling was carried out at a depth of about 0.4-0.5m in the mid-region along the near-surface zone of Maizuru embankment on 21 October, 2017. This depth of sampling was chosen by analyzing the results of portable cone penetrometer tests performed over a year where the soil layer having higher strength from the surface was located. **Figure 7.4** shows the location of undisturbed sampling and the depth profiles of water content and penetration resistance measured in the near-surface zone on the day of sampling.

Figure 7.5(a) shows the particle size distribution curves for the near-surface soil at different depths. The top surface soil (i.e. 0-20cm depth) showed a slightly gap-graded profile of particle size distribution with higher percentage of sand particles in comparison to other depths. The particle size distribution of the undisturbed samples (i.e. 40-50cm depth) showed uniform distribution of finer clay to coarser sand particles nearer to the samples collected during the construction of the embankment. The particle size distribution curves for all other depths show the uniform distribution of finer clay to coarser sand particles and tend to converge into a narrow region.

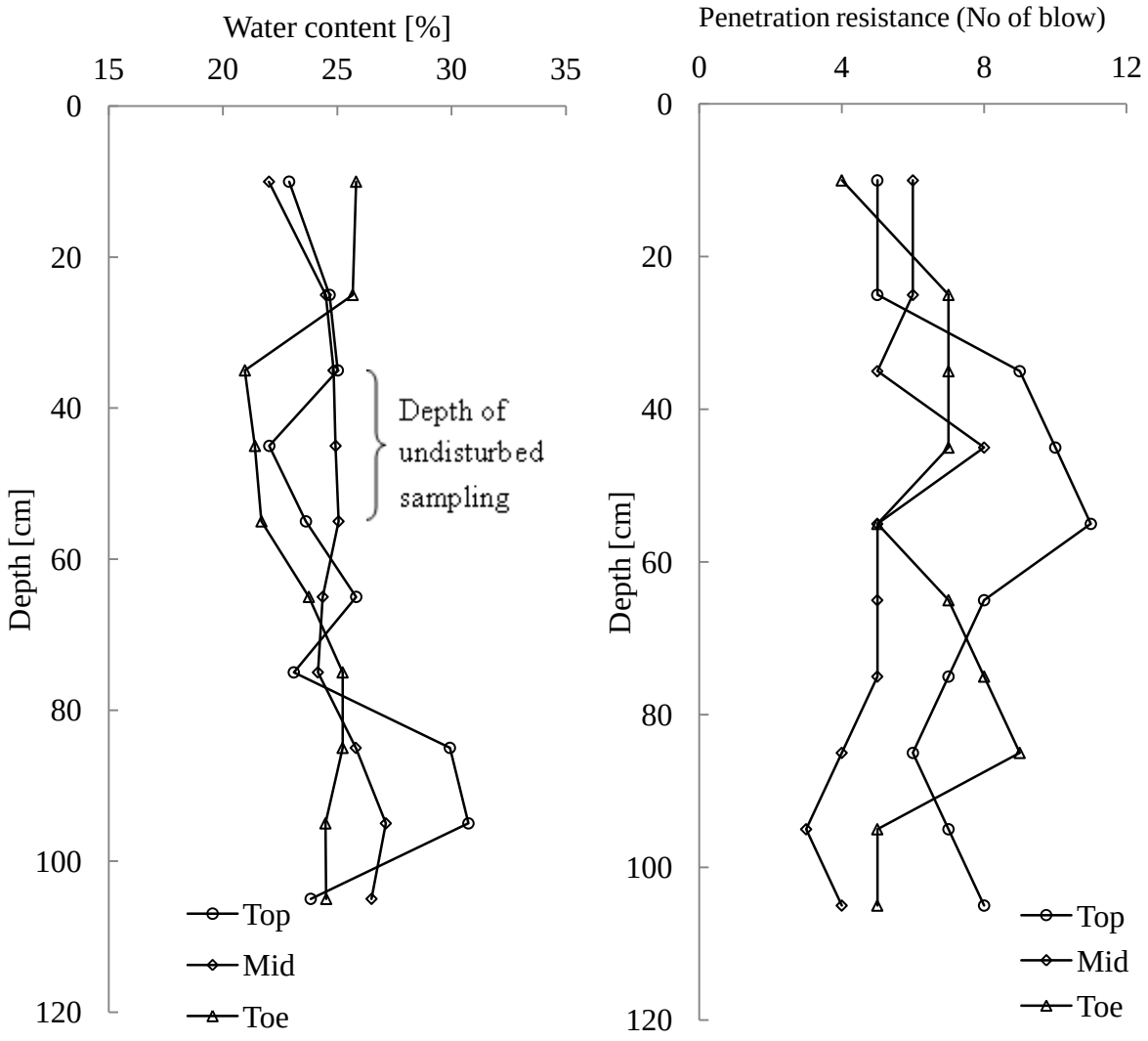

Figure 7.4. Depth profiles of water content and penetration resistance during undisturbed sampling in Maizuru embankment slope on 21 October, 2017

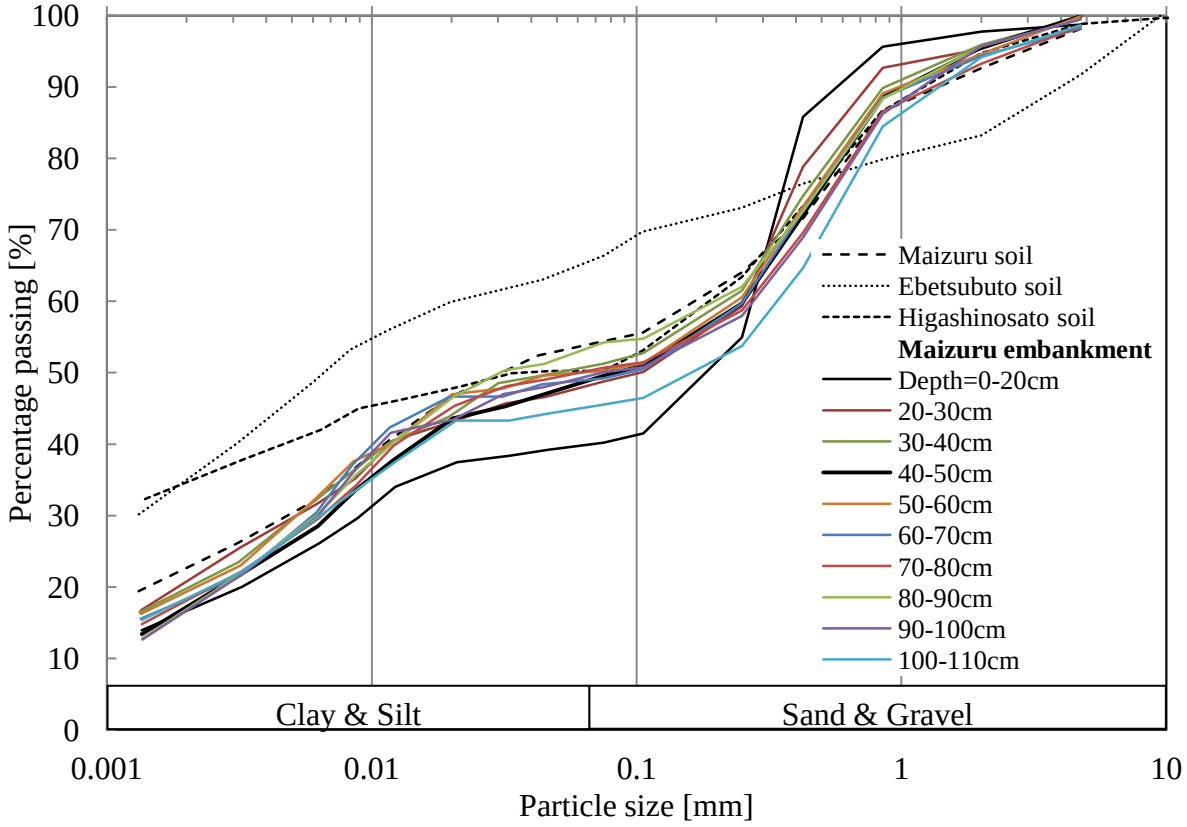

Figure 7.5. Particle size distribution curves for near-surface soil at different depths in Maizuru embankment slope

7.4 RESULTS FROM CONSOLIDATED-UNDRAINED TRIAXIAL COMPRESSION TESTS

The experimental results obtained from the consolidated-undrained triaxial compression tests at low to medium isotropic consolidation stresses, p'=10, 20, 50, and 400kPa on both laboratory (as)-compacted samples (Ebetsubuto, Higashinosato, and Maizuru soils) and field-compacted (undisturbed) samples (Maizuru soil) of clay-sand mixed soils are presented. The results are interpreted and discussed in terms of undrained effective stress paths and stress-strain curves. The undrained effective stress paths are expressed in terms of mean effective stress (p') plotted against deviatoric stress (q). As it is difficult to define a soil failure on the stress path for these strain hardening compacted clay-sand mixed soils, the failure is assumed

at a state when the maximum stress ratio (q/p') is mobilised on a failure plane; and the critical state is assumed at an ultimate state, at the end of shearing, which is corresponding to the maximum axial strain, ε_a=15%.

7.4.1 UNDRAINED EFFECTIVE STRESS PATHS AND STRESS-STRAIN BEHAVIOUR

As-compacted Ebetsubuto soil

Figure 7.6 (a) shows the undrained effective stress paths for the as-compacted samples of Ebetsubuto soil with water contents, $1.05w_{opt}$, $1.15w_{opt}$ and $1.30w_{opt}$. The stress paths followed by the as-compacted samples are strain-hardening up to high strain. The stress paths show initial contractive behaviour, which is followed by strong dilation so that they turn rightwards close to the failure and heading towards a potential critical state. The contractive behaviour in the compacted specimens at the initial stage could be due to the presence of occluded air bubbles which increased the compressibility of soil, and eventually the pore water pressure during shearing. This behaviour appears to be pronounced in comparison to the saturated samples of reconstituted and natural soils. In the past research, VandenBerge et al. (2014) also reported that the stress paths for the clay specimens compacted with water contents slightly wet of optimum showed similar strain hardening behaviour up to high strains by performing a series of consolidated-undrained triaxial tests at consolidation stresses (28-379kPa). Comparing the stress paths at low confining stresses (p'<50kPa) for different states, the compacted specimens showed broadly similar behaviour, as indicated by the shape of the stress paths. However, comparing the stress paths at higher confining stress (p'=400kPa) for different states, the compacted specimens for different states showed noticeably different initial contractive behaviour than at the low confining stresses, probably

due to different degree of saturation and grain crushing during shearing at the higher stress. All the stress paths eventually converge along a critical state line with a gradient M=1.34.

The deviatoric stress (q)-axial strain (ε_a) curves and the excess pore water pressure (Δu)-axial strain (ε_a) curves for the as-compacted samples of Ebetsubuto soil are presented in **Figure 7.6(b)** and **(c)**. The deviatoric stress in the dense compacted specimens increased gradually with axial strain without a distinct peak state and eventually reached a critical state, with small but negligible strain hardening closer to the maximum axial strain, ε_a=15%. At low confining stresses (p'<50kPa), the compacted specimen contracted initially, as indicated by the shape of the stress paths, so that the pore water pressure increased with shearing, and the maximum positive excess pore water pressure developed at smaller axial strain, and then decreased gradually as the specimen started dilating. At larger axial strain, the continuous decreased in pore water pressure resulted in negative excess pore water pressure. At higher confining stress (p'=400kPa), the pore water pressure increased gradually with shearing and the positive excess pore water pressure became maximum, and then decreased slightly at larger axial strain when the sample started dilating.

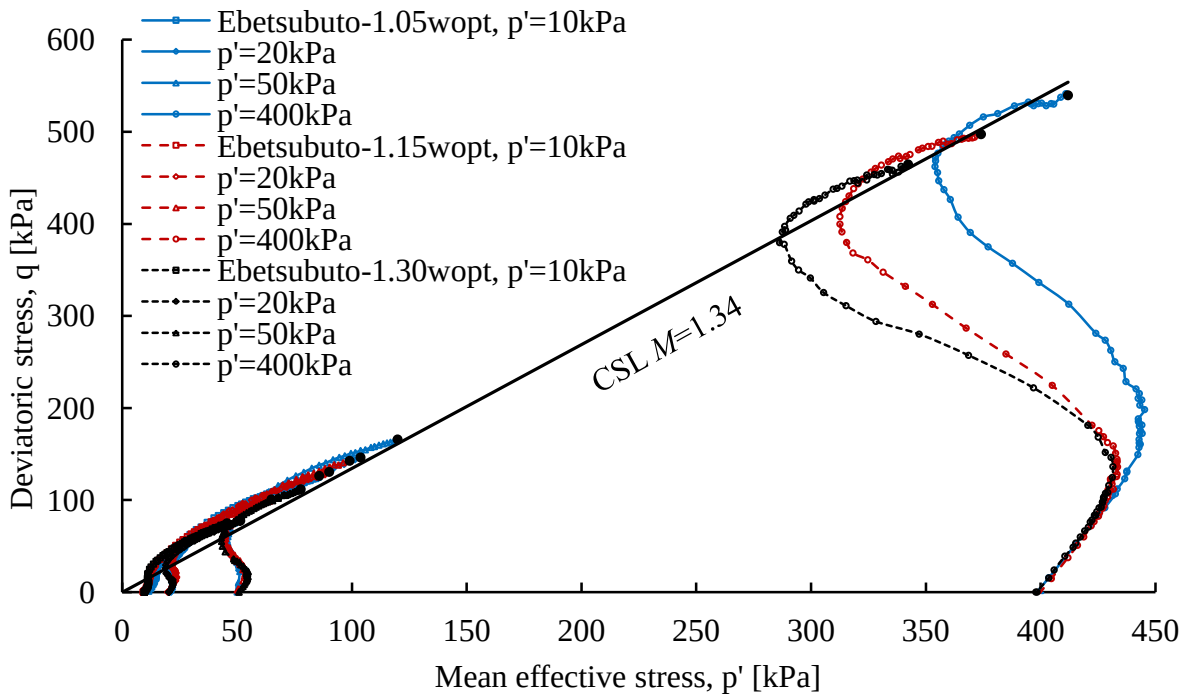
Ebetsubuto-1.05wopt, p'=10kPa
p'=20kPa
p'=50kPa
p'=400kPa
Ebetsubuto-1.15wopt, p'=10kPa
p'=20kPa
p'=50kPa
p'=400kPa
Ebetsubuto-1.30wopt, p'=10kPa
p'=20kPa
p'=50kPa
p'=400kPa
CSL M=1.34
Deviatoric stress, q [kPa]
Mean effective stress, p' [kPa]
0
100
200
300
400
500
600
0
50
100
150
200
250
300
350
400
450

(a)

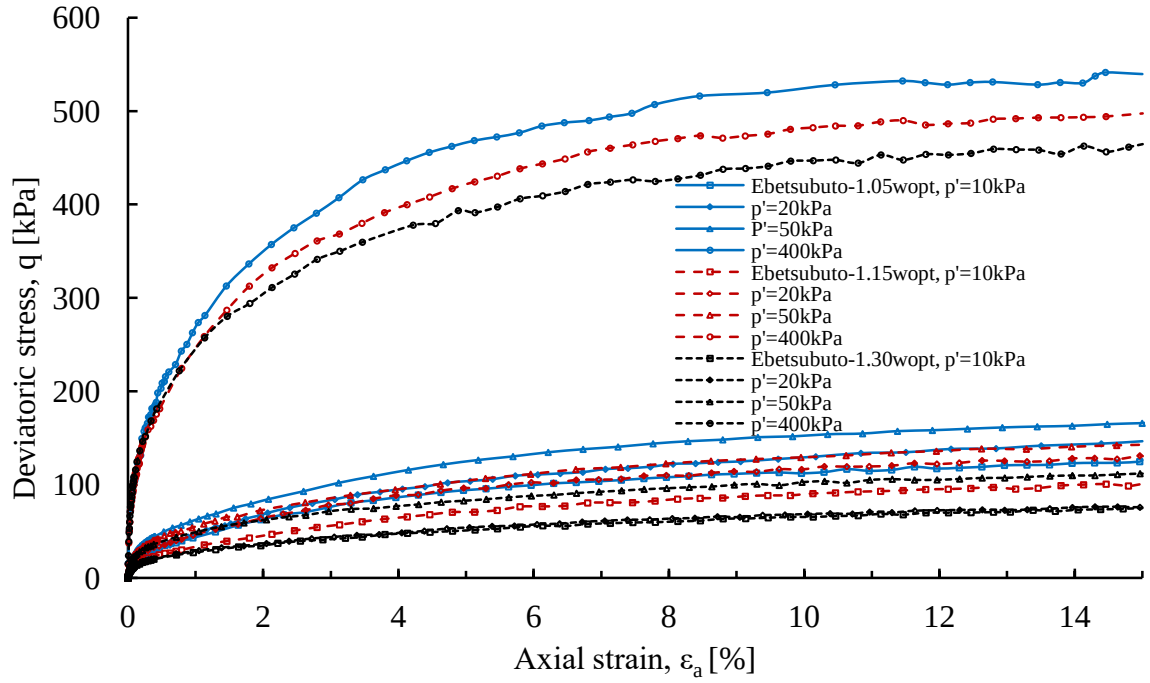
Ebetsubuto-1.05wopt, p'=10kPa
p'=20kPa
P'=50kPa
p'=400kPa
Ebetsubuto-1.15wopt, p'=10kPa
p'=20kPa
p'=50kPa
p'=400kPa
Ebetsubuto-1.30wopt, p'=10kPa
p'=20kPa
p'=50kPa
p'=400kPa
Deviatoric stress, q [kPa]
Axial strain, εa [%]
0
100
200
300
400
500
600
0
2
4
6
8
10
12
14

(b)

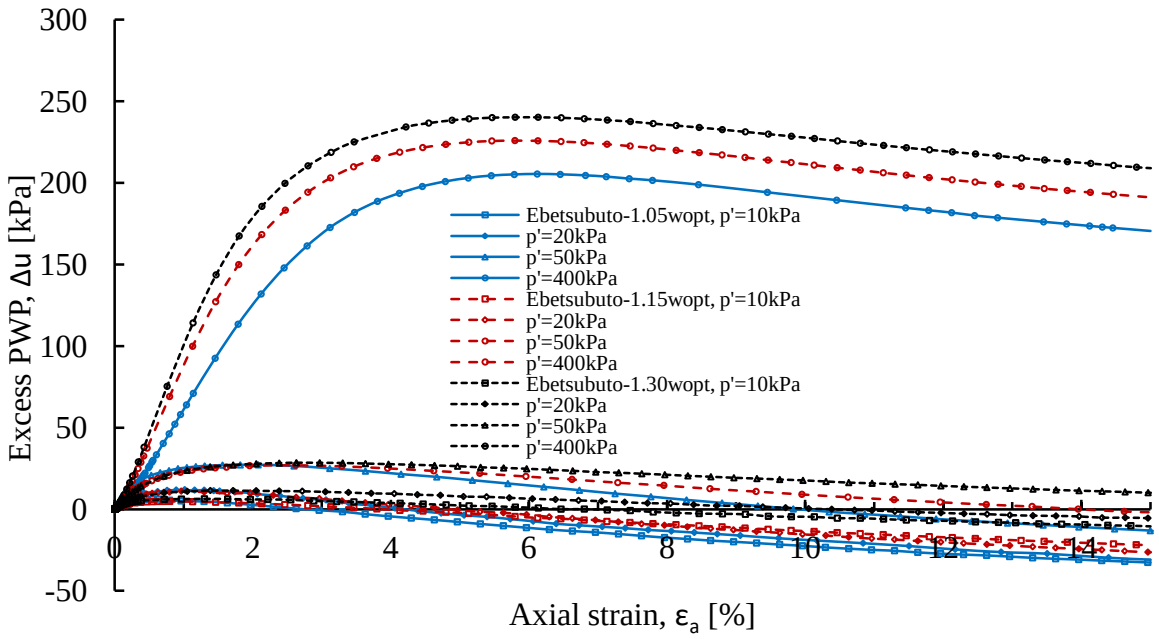

(c)

Figure 7.6. Undrained effective stress paths and stress-strain curves for as-compacted Ebetsubuto soil (a) Stress paths (b) Deviatoric stress-axial strain curves (c) Excess pore water pressure-axial strain curves

As-compacted Higashinosato soil

The undrained effective stress paths for the as-compacted samples of Higashinosato soil with water content, 1.30w_{opt}, are shown in **Figure 7.7 (a).** The stress paths are strain hardening up to high strain as in the as-compacted specimens of Ebetsubuto soil, but the rates of strain hardening are different as the Higashinosato soil has more sand particles than the Ebetsubuto soil as indicated by the gradation curves. All the stress paths eventually converge along a critical state line with a gradient, M=1.50.

The deviatoric stress (q)-axial strain (ε_a) curves and the excess pore water pressure (Δu)-axial strain (ε_a) curves during undrained shearing are presented in **Figure 7.7 (b)** and **(c)**. The deviatoric stress in the compacted specimens increased gradually with axial strain without a distinct peak state and reached a critical state. The pore water pressure in such dense compacted specimen at low confining pressure increased gradually with shearing and reached

maximum positive excess pore water pressure which then decreased gradually and even became negative excess pore water pressure at larger axial strain as the dilation was very strong. However, at higher confining stress, the pore water pressure increased gradually with shearing and became maximum positive excess pore water pressure, as the specimen contracted initially, and then decreased slightly at higher strain, as the sample started dilating.

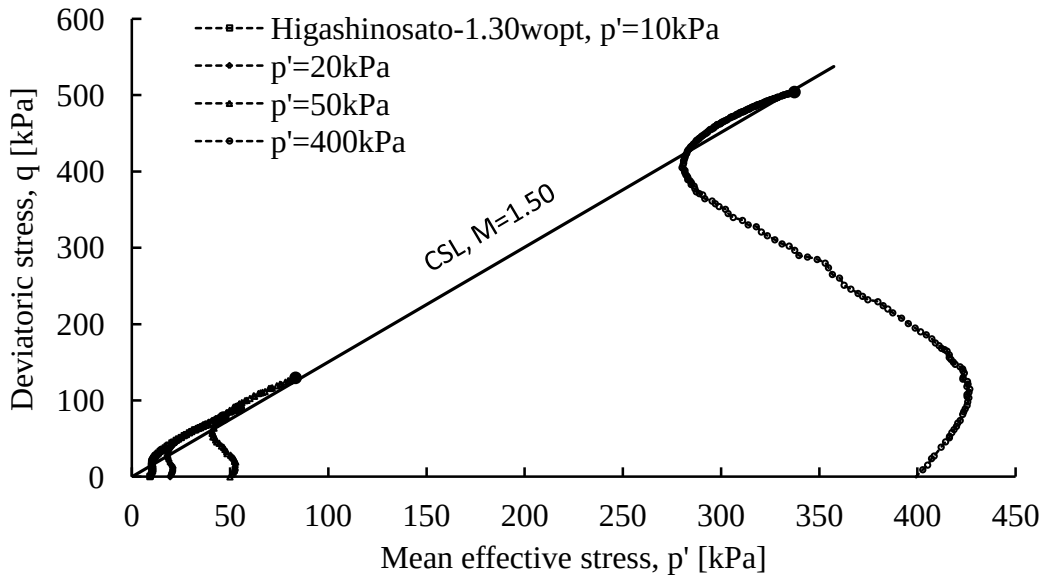

(a)

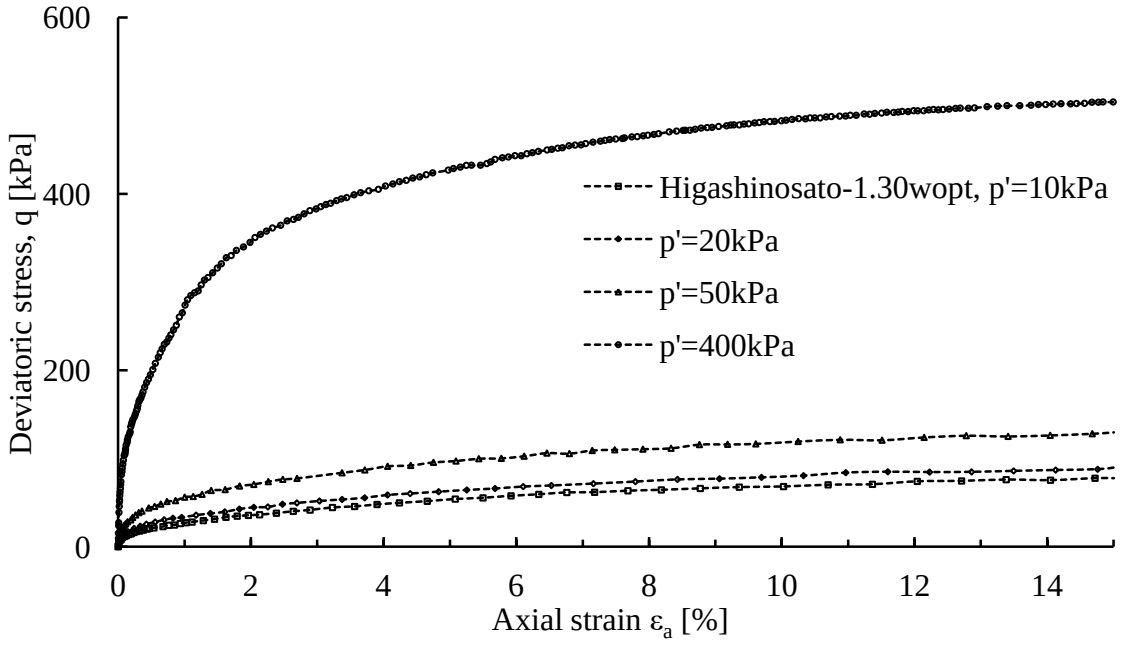

(b)

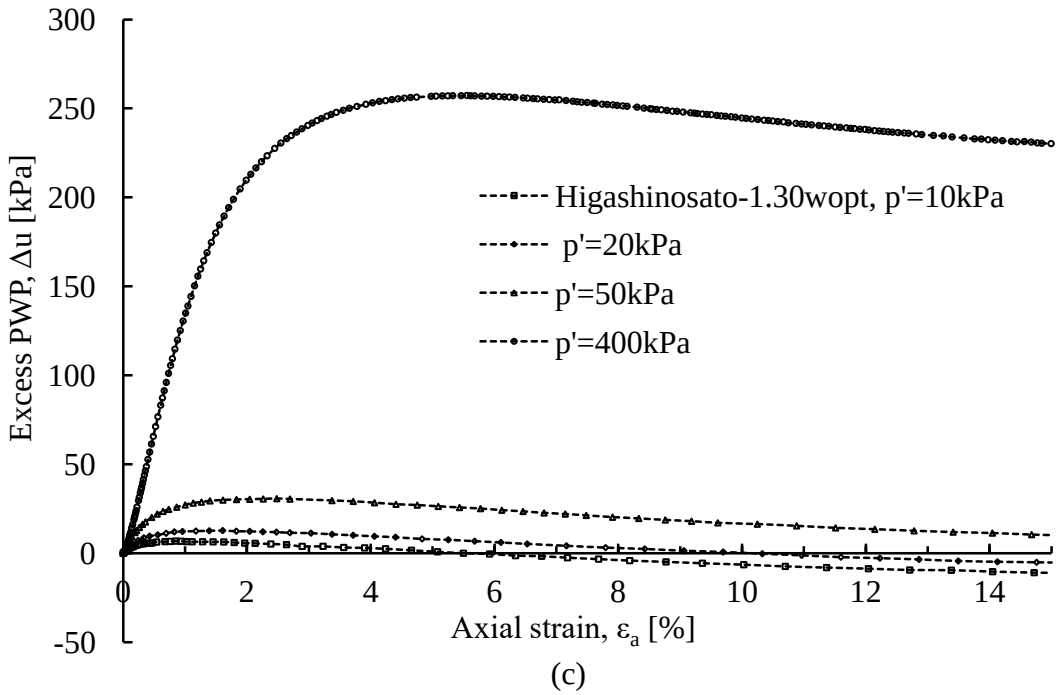

(c)

Figure 7.7. Undrained effective stress paths and stress-strain curves for as-compacted Higashinosato soil (a) Stress paths (b) Deviatoric stress-axial strain curves (c) Excess pore water pressure-axial strain curves

Undisturbed and as-compacted Maizuru soil

Figure 7.8 (a) shows the undrained effective stress paths for the field-compacted (undisturbed) and the as-compacted samples of Maizuru soil. The experimental result on the as-compacted sample with a confining stress (p'=20kPa) is only included in this section because other results were not reliable due to the problem with sensors' calibration, as mentioned in Chapter 5. The stress paths for both types of samples are strain hardening up to high strain, similar to the as-compacted samples of Ebetsubuto and Higashinosato soils. Similar behaviour of stress paths was also observed from the constant-volume direct shear tests and hollow cylinder simple shear tests on the as-compacted samples of Maizuru soil, as explained in Chapter 6. All the stress paths eventually converge along a critical state line with a gradient M=1.66. The deviatoric stress (q)-axial strain (ε_a) curves and the excess pore water pressures (Δu)-axial strain (ε_a) curves also conform well to the as-compacted samples of

Ebetsubuto and Higashinosato soils ranging from smaller to larger strains, as shown in **Figures 7.8 (b)** and **(c)**.

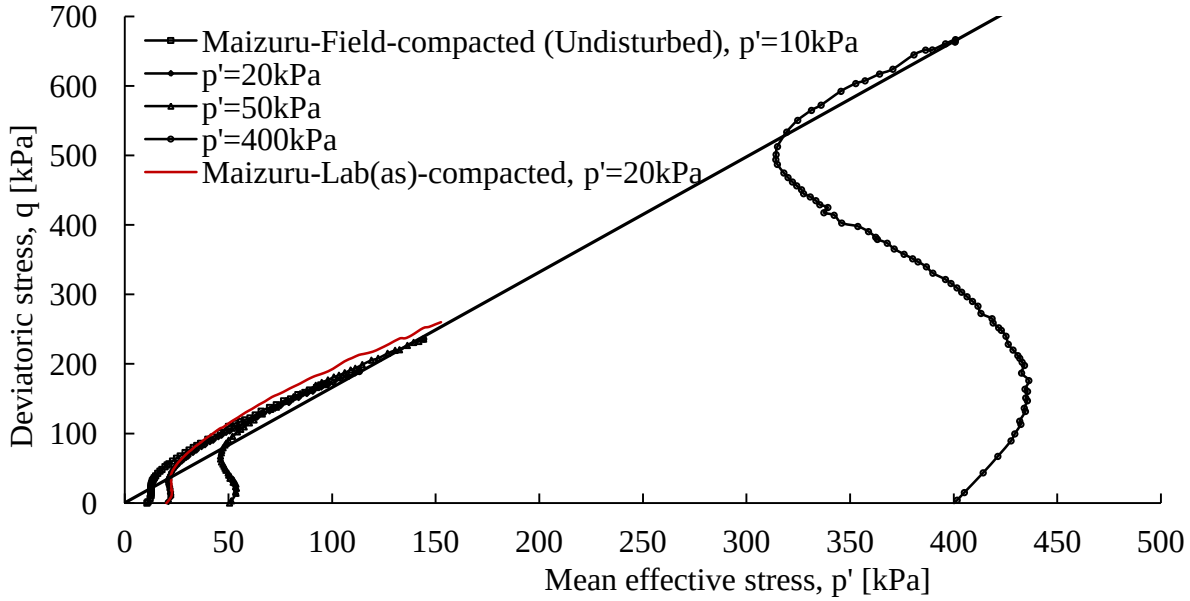

(a)

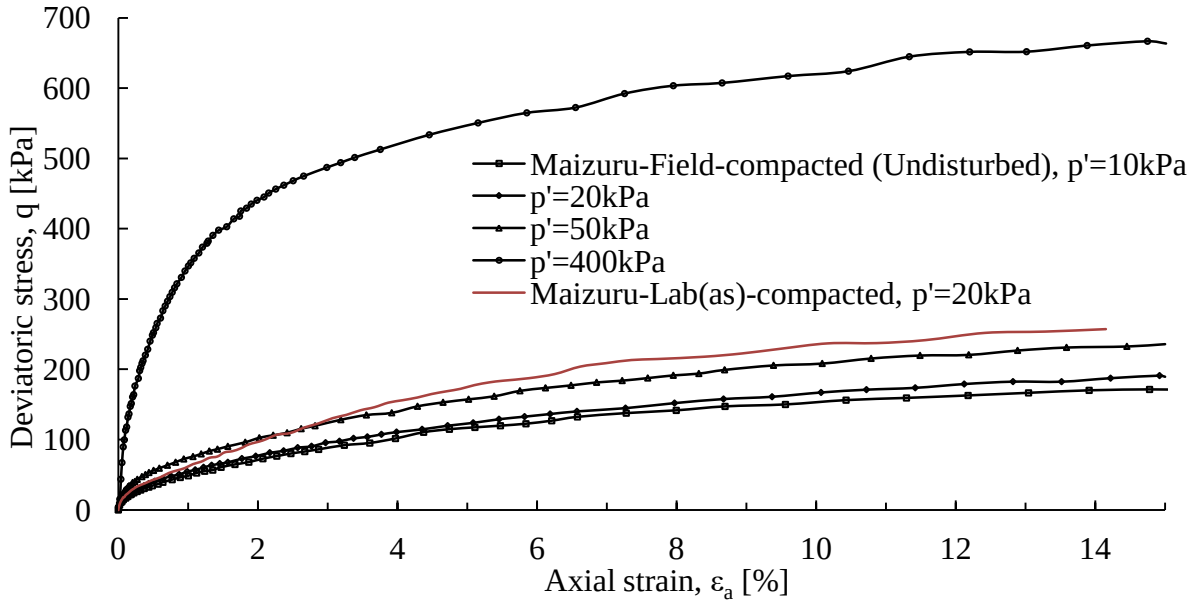

(b)

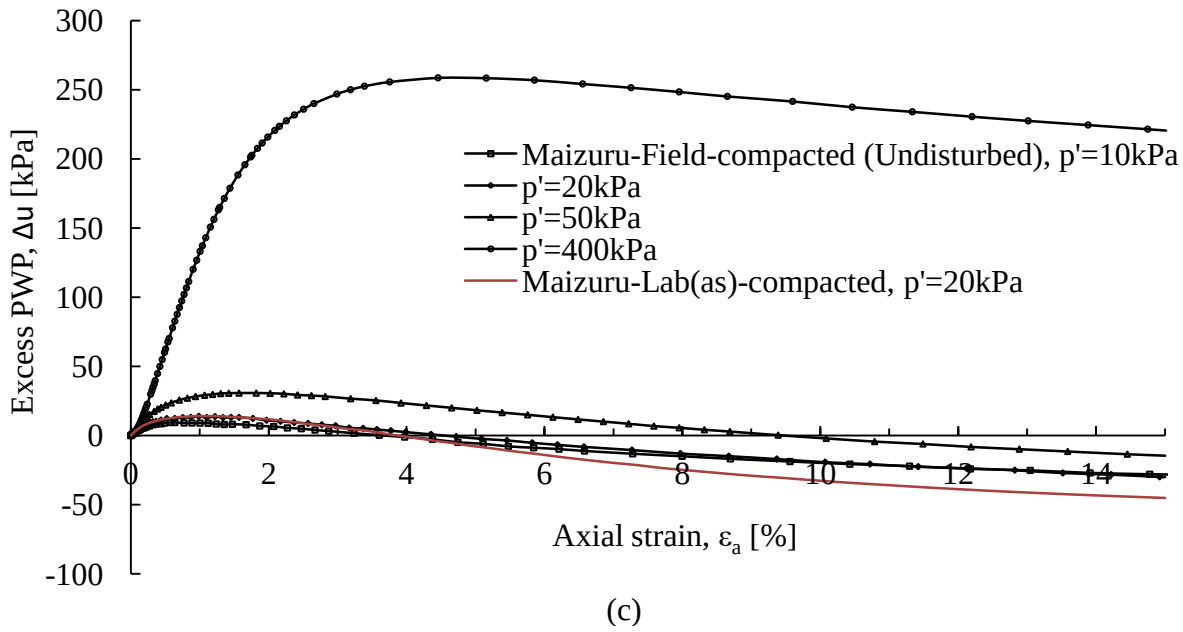

(c)

Figure 7.8. Undrained effective stress paths and stress-strain curves for Maizuru soil (a) Stress paths (b) Deviatoric stress-axial strain curves (c) Excess pore water pressure-axial strain curves

7.4.2 UNDISTURBED VS AS-COMPACTED STATES

Figure 7.9 shows the comparison of the undrained effective stress paths, for both as-compacted samples of Ebetsubuto and Higashinosato soils, and undisturbed samples of Maizuru soil, although they all have different density and apparent OCRs before shearing. The compacted samples of all the tested soils contracted initially upon shearing in an identical manner and changed their behaviour to dilative and strain hardening without well-defined peak state. However, at higher confining stress (*p'*=400kPa), the difference in the contractive behaviour were more pronounced between the samples of different states before reaching the failure. The triaxial compression test results reported by Coop (1990) on the compacted carbonate sand sample also showed similar initial contractive behaviour of the stress path at a similar range of confining pressure.

Assuming the critical states at the end of shearing, corresponding to the maximum axial strain ε_a = 15%, on the stress paths, the critical state lines are drawn for both as-compacted Ebetsubuto and Higashinosato soils and undisturbed Maizuru soil, as shown in **Figure 7.9**. It should be noted that a well-defined critical state for such dense clay-sand mixed soil specimens might need shearing further, as indicated by the strain-hardening behaviour, but due to the problem of non-uniformity of deformations and constraints of boundary conditions all the tests were stopped after reaching the maximum axial strain, ε_a = 15%. Kim et al. (2016) reported that identifying the critical state conditions in the dense compacted specimens have always been a difficult task, even at large strains (>25%) changes were observed in deviator stress and volumetric strains. In this study, assuming critical states at the maximum axial strain, ε_a = 15%, do not affect significantly the subsequent discussion on the strength behaviour of both as-compacted and undisturbed soils, as the curves of deviator stress and excess pore water pressure with axial strain became almost flat at the larger axial strain range, as explained earlier.

The critical state line in a *q-p'* plane can be represented by:

$$q = Mp' \qquad \text{Equation 7.1}$$

Figure 7.9 shows the critical state lines for both as-compacted and undisturbed soils, which give average critical state strength parameters of gradients, M = 1.34 and 1.50, and critical state friction angles, φ_{crit} =33.2^o and 36.9^o, for the as-compacted Ebetsubuto and Higshinosato soils, respectively, and M =1.66 and φ_{crit} = 40.55^o for the undisturbed Maizuru soil.

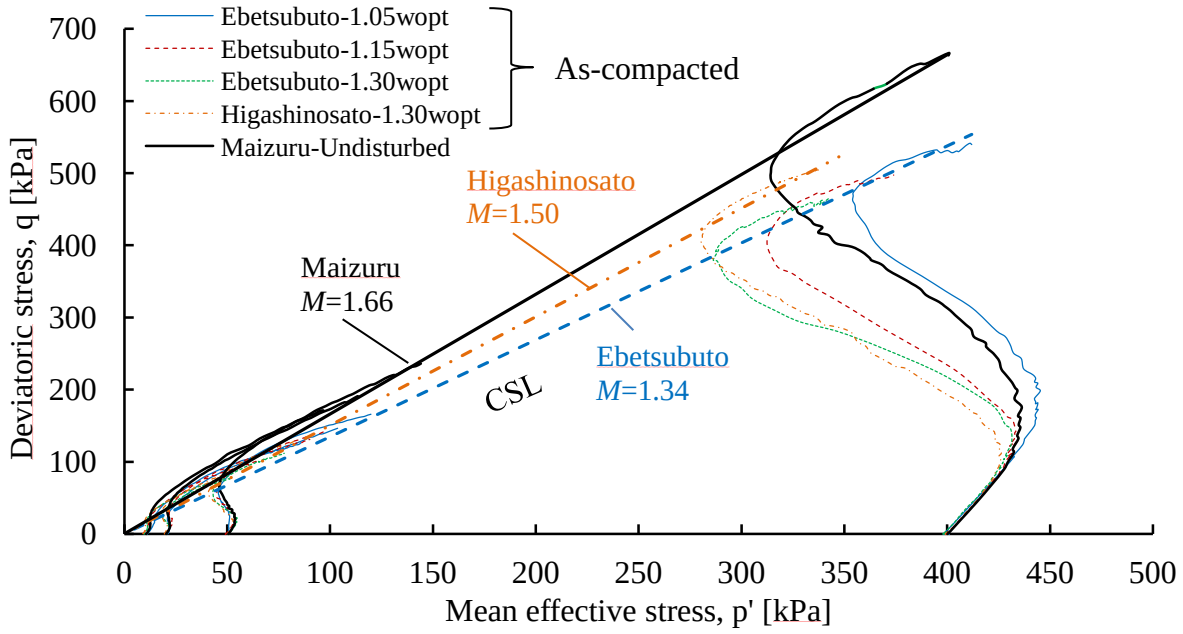

Figure 7.9. Comparison of undrained effective stress paths between as-compacted Ebetsubuto and Higashinosato soils, and undisturbed Maizuru soil

Additional undrained isotropic triaxial compression tests on as-compacted samples of Maizuru soil and Higashinosato soil are compared with those of the undisturbed Maizuru samples, as shown in **Figure 7.10**. The as-compacted Maizuru soil sample was prepared with the water content (23.19%) same as that of the undisturbed sample, and the triaxial test was then performed at an isotropic confining pressure, p'=20kPa. Similarly, the as-compacted sample of Higashinosato soil was prepared with the water content close to that of the undisturbed Maizuru sample and the triaxial test was then performed at an isotropic confining pressure, p'=10kPa. When comparing the stress paths at p'=20kPa, between the undisturbed and as-compacted Maizuru samples, as shown in **Figure 7.10 (a)**, the undisturbed sample showed initially stiff behaviour, but eventually resulted in less dilative behaviour and significantly lower undrained strength than the as-compacted sample. This may indicate that the soil fabric in the undisturbed specimen was significantly different than that in the as-compacted specimen, probably due to the influence of seasonal wetting drying cycles in the

near-surface soil. When comparing the stress paths at p'=10kPa, the undisturbed Maizuru sample showed stiff and brittle behaviour with significantly higher undrained strength than the as-compacted Higashinosato sample. In **Figure 7.10 (b)**, it is interesting to note that the stress ratio (q/p') for the sample of undisturbed Maizuru soil at p'=10kPa showed a marked peak state with $q/p' \approx 3$ similar to the overconsolidated soil with bonding. From this observation it can be concluded that the higher strength soil layer at the depth of 0.4-0.5m in the Maizuru river dyke slope, where the undisturbed sampling was carried out, may have experienced overconsolidation, possibly the inter-particle bonding.

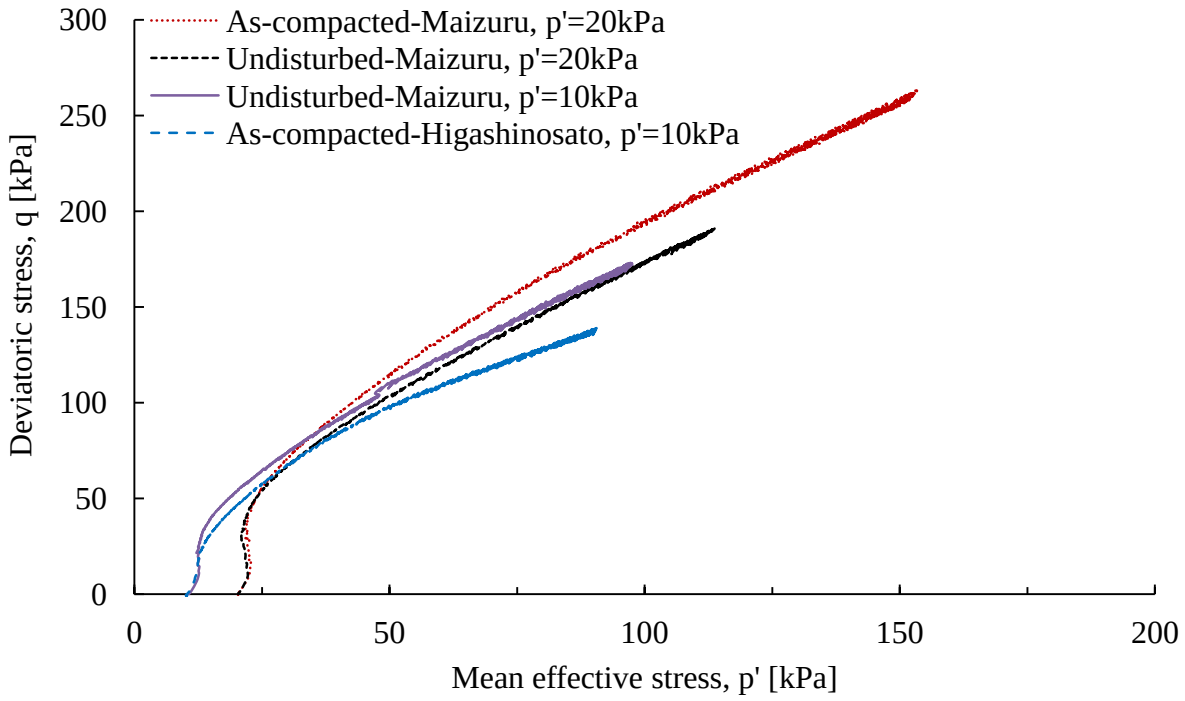

(a)

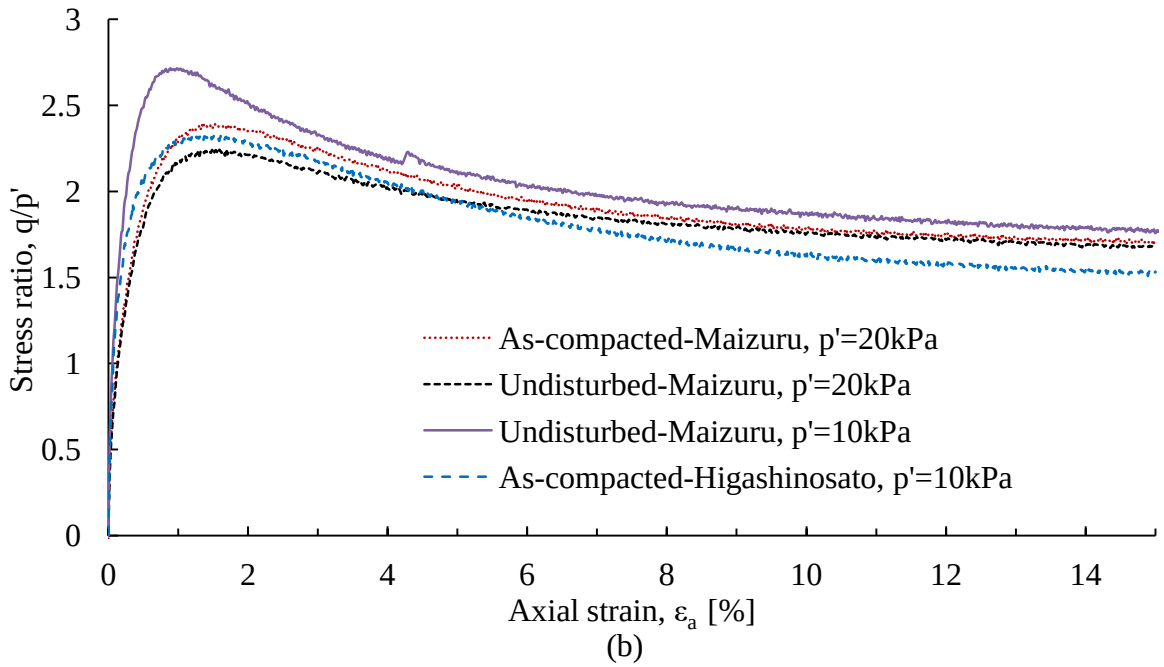

(b)

Figure 7.10. Comparison of stress-strain behaviour between undisturbed samples and as-compacted samples (a) Undrained effective stress paths (b) Stress ratio

7.4.3 CONSOLIDATED-UNDRAINED STRENGTH ENVELOPES

For the conventional limit equilibrium analysis of short-term problems, such as failure due to cone penetration, and shallow slope failure due to heavy rainfall, the consolidated-undrained strength envelopes based on total stress term is more straightforward than effective stress term. As the total stress analysis generally does not involve excess pore water pressure, the consolidated-undrained strength envelopes are drawn based on the undrained shear strength (c_u) and the vertical effective consolidation stress (σ'_0) from the triaxial compression tests. **Figure 7.11** shows the consolidated-undrained strength envelopes for the as-compacted samples of Ebetsubuto and Higashinosato soils and undisturbed Maizuru soil. It can be seen from the undrained effective stress paths of different samples, as presented earlier, the undrained strength (c_u) is difficult to define for these strain hardening compacted soils, a limiting axial strain criterion is assumed (Fleming and Duncan, 1990), and the shear strength measured at axial strain, ε_a=15%, is assumed as the undrained strength (c_u) in this study.

The consolidated-undrained strength envelopes are fitted well with lines and they are significantly different for different states of the same soil indicating a strong effect of initial compaction water contents on the undrained strength behaviour. Similar undrained strength behaviour was also observed on the compacted clay specimens by VandenBerge et al. (2014). They highlighted that the initial compaction conditions affect the pore water pressure response during shearing and eventually the consolidated-undrained strength envelopes, but this effect was less pronounced in the effective stress strength envelopes. The figure also shows the consolidated-undrained strength envelopes for the as-compacted Maizuru soil with water content of $1.15w_{opt}$ from the constant-volume direct shear tests, which is approximately parallel to that of the undisturbed Maizuru soil, but shows significantly lower undrained strength.

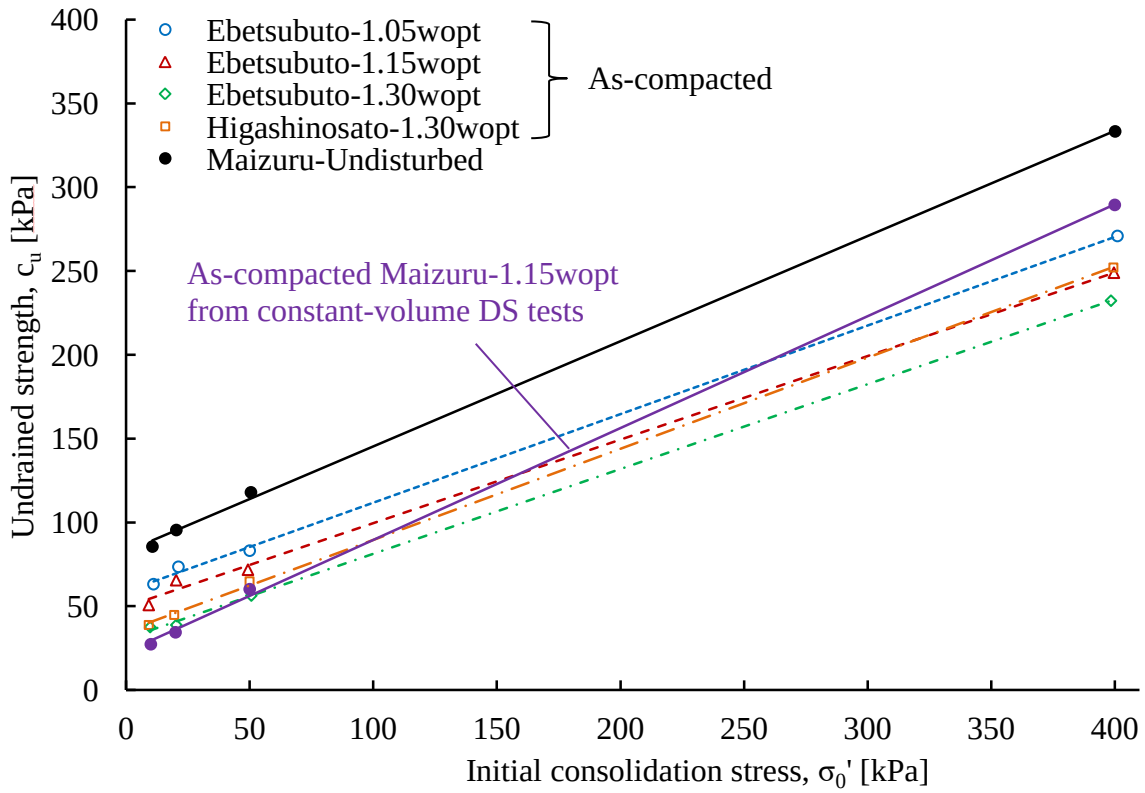

Figure 7.11. Consolidated-undrained strength envelopes for as-compacted Ebetsubuto and Higashinosato soils, and undisturbed Maizuru soil

7.5 PEAK AND CRITICAL STATES

Figures 7.12 and **7.13** show the critical state lines for different states of as-compacted Ebetsubuto and Higashinosato soils, and undisturbed Maizuru soil in *q-p'* and *v*-log*p'* planes. These critical state lines in the *q-p'* plane are drawn by taking the critical state points on the stress paths corresponding to the maximum axial strain, ε_a=15%, as explained earlier. In the *v*-log*p'* plane, they are drawn by calculating specific volumes based on water contents measured at the end of undrained shearing. The gradients (*M*) of these critical state lines in the *q-p'* plane for the different states of as-compacted Ebetsubuto soil are comparable with each other, which lie in a range, *M*=1.33-1.37. Similarly, for the as-compacted Higashinosato soil and the undisturbed Maizuru soil, the gradients are, *M*=1.50, and 1.66, respectively.

In the *v*-log*p'* space, the critical state lines for the as-compacted Ebetsubuto soil are distinctly different and approximately parallel with each other, as shown in **Figure 7.13**. Such behaviour of showing non-unique critical state lines for the as-compacted states with different initial water contents or densities is typical for the clay-sand mixed intermediate or transitional soils (e.g. Ferreira and Bica, 2006; Shipton and Coop, 2012; Coop, 2015; Xu and Coop, 2016). In the *v*-log*p'* space, the critical state lines are represented by:

$$v = v_\Gamma - \lambda \, log p' \qquad \text{Equation 7.2}$$

where intercept (v_Γ) and gradient (λ) are critical state parameters, which are listed in **Table 7.1**. For the as-compacted Ebetsubuto soil, the parameters are in ranges, λ =0.145-0.163, and v_Γ=2.03-2.10. For the as-compacted Higashinosato soil and the undisturbed Maizuru soil, the parameters are, λ=0.191 and 0.157, and v_Γ=2.19 and 2.03, respectively.

As this study focuses on the shallow slope stability analysis, to understand the strength behaviour based on the effective stress approach, the power-law strength criterion is used to

represent the peak strength envelopes for both as-compacted and undisturbed soils (de Mello, 1977; Charles, 1982; Maksimovic, 1989; Baker, 2004; Atkinson, 2007), as discussed in Chapter 6. The peak strength envelopes for different states of soils, which are presented in **Figure 7.14**, are expressed as:

$$q = mp^{n} \qquad \text{Equation 7.3}$$

where *m* and *n* are peak strength parameters. The power-law strength parameters, *m* is similar to the friction coefficient, and *n* is the degree of non-linearity, which are listed in **Table 7.1**. The degrees of non-linearity for both as-compacted Ebetsubuto and Higashinosato soils and undisturbed Maizuru soil are comparable with each other, which lie in a range *n*=0.84-0.87. In which *n*=1 represents the linear peak strength envelopes. However, the degree of non-linearity of failure envelope for the as-compacted Maizuru soil from the constant-volume direct shear tests was close to unity, i.e. *b*=0.99, as mentioned in Chapter 6. And the parameter, *m*=3.47, 3.48, and 3.04, for the as-compacted Ebetsubuto soil with initial water contents 1.05w_{opt}, 1.15w_{opt}, and 1.30w_{opt}, respectively. For the as-compacted Higashinosato soil with initial water content 1.30w_{opt} and undisturbed Maizuru soil, the parameter *m*=3.09 and 3.74, respectively. It can be reported that the peak strength of compacted samples was less affected by the initial compaction water contents, as indicated by the power-law effective strength parameters.

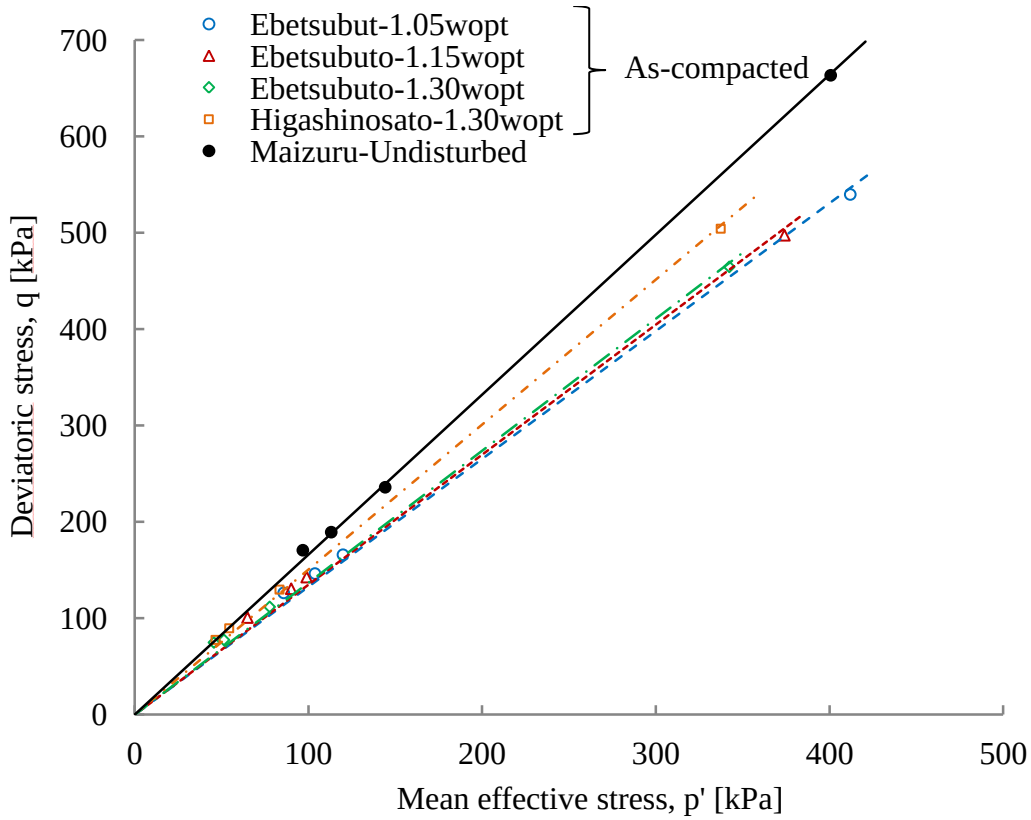

Figure 7.12. Critical state lines for as-compacted Ebetsubuto and Higashinosato soils, and undisturbed Maizuru soil in *q-p'* space

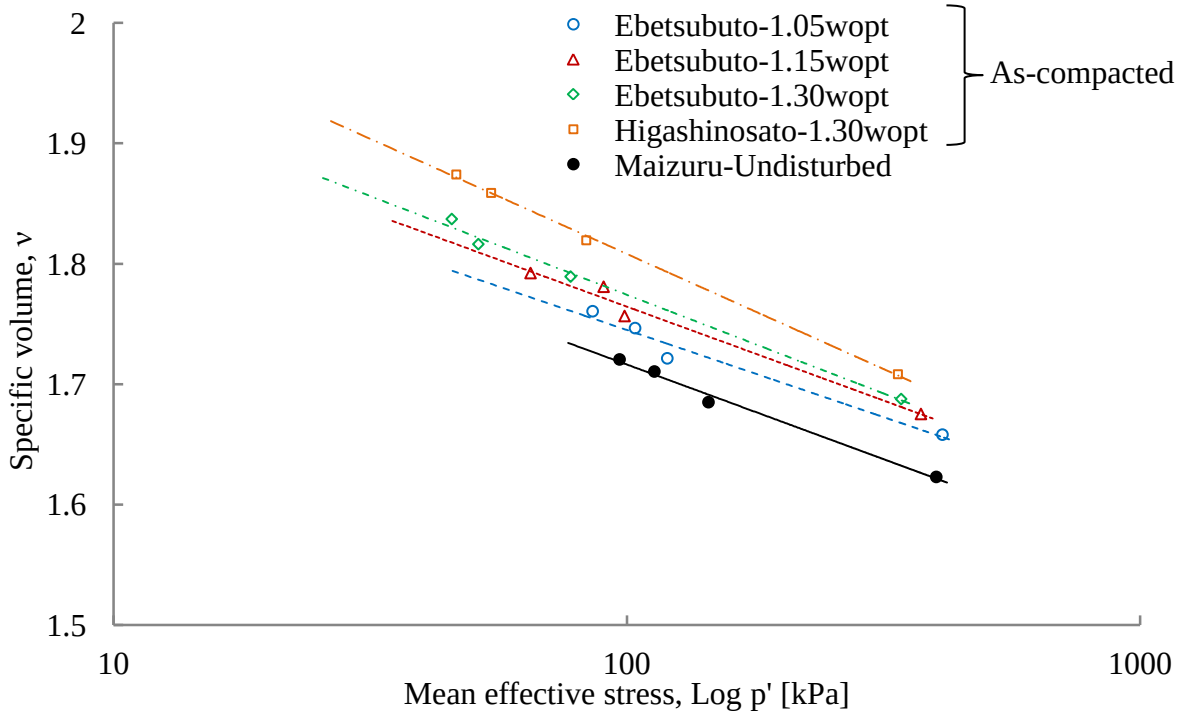

Figure 7.13. Critical state lines for as-compacted Ebetsubuto and Higashinosato soils, and undisturbed Maizuru soil in *v*-log*p'* space

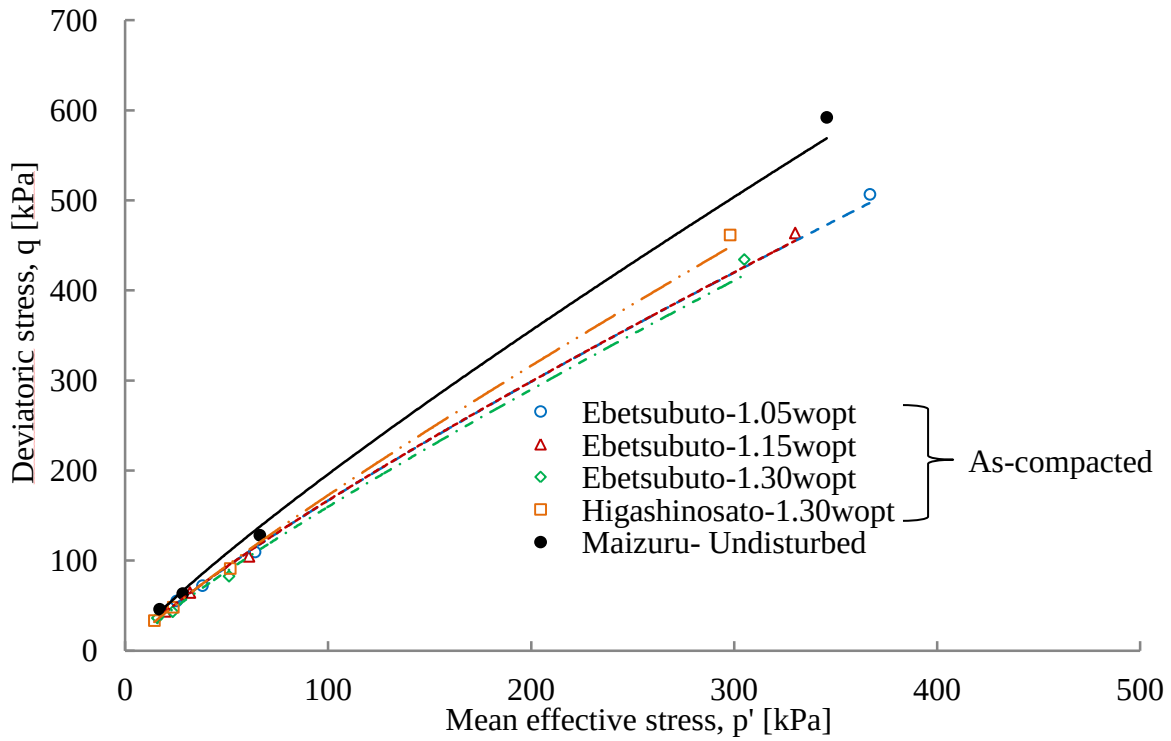

Figure 7.14. Non-linear peak strength envelopes for as-compacted Ebetsubuto and Higashinosato soils, and undisturbed Maizuru soil in *q-p'* space

Table 7.1. Peak and critical state parameters for as-compacted Ebetsubuto and Higashinosato soils, and undisturbed Maizuru soil

Name of soils	States	m	n	M	v_Γ	Λ	μ	H
Ebetsubuto	$1.05w_{opt}$	3.47	0.84	1.33	2.03	0.145	0.98	0.63
	$1.15w_{opt}$	3.48	0.84	1.35	2.08	0.157	1.00	0.65
	$1.30w_{opt}$	3.04	0.86	1.37	2.10	0.163	1.02	0.63
Higashinosato	$1.30w_{opt}$	3.09	0.87	1.50	2.19	0.191	0.97	0.63
Undisturbed Maizuru	$\approx 1.0w_{opt}$	3.74	0.86	1.66	2.03	0.157	0.96	0.72

7.5.1 NORMALIZING TO TAKE ACCOUNT OF DIFFERENT OCR AND SPECIFIC VOLUMES

All the as-compacted and undisturbed specimens of the tested soils have different specific volumes or apparent overconsolidation ratios induced by the dynamic compaction just before undrained shearing. In order to assess the undrained strength behaviour by taking account of these differences, the stress paths and peak strength envelopes are normalized by the critical equivalent pressure (p_c') on the critical state line. The equivalent critical pressure is calculated by using the specific volume just before undrained shearing on the critical state line defined as below:

$$p'_c = exp\frac{\nu - \nu_\Gamma}{\lambda} \qquad \text{Equation 7.4}$$

The mean effective stresses are normalized with respect to p'_c and the deviator stresses are normalized with respect to Mp'_c. The critical state points for all the tested soils fall close to a point $\frac{p'}{p'_c} = 1$ and $\frac{q}{Mp'_c} = 1$.

After the normalization, the non-linear power-law peak strength envelopes become:

$$\frac{q}{Mp'_c} = \mu\left(\frac{p'}{p'_c}\right)^{\eta} \qquad \text{Equation 7.5}$$

The peak strength parameter, μ, which is equivalent to the friction coefficient, became close to unity, as listed in **Table 7.1**. And the other parameter, η, which represents the degree of curvature of the normalized peak strength envelope, along the Hvorslev surface on the dry of the critical, which lie in a range η=0.63-0.72**.** Comparisons of the degrees of non-linearity of peak strength envelopes in the un-normalised and normalised forms show that the degrees of non-linearity increased after being normalised by the critical equivalent pressure. The non-

linear power-law failure criterion used by Shi et al. (2017) to represent the Hvorslev surface for highly overconsolidated soils also showed the similar behaviour after the normalisation with respect to the equivalent pressure. The study concluded that the non-linear Hvorslev surface incorporated into the elastoplastic and hypoplastic models represented well the stress-strain and volumetric behaviour observed in the laboratory and somehow overcame the problem of overestimating the strength in highly overconsolidated range.

The normalised peak strength envelopes for the as-compacted Ebetsubuto and Higashinosato soils, and the undisturbed Maizuru soil are shown in **Figure 7.15**. In the figure, the broken line OA represent the no tension cut-off, for which σ'_3=0. Comparing all the normalised peak strength envelopes, it should be noted that the normalised strength of undisturbed samples was lower than that of all the as-compacted strength of similar Ebetsubuto and Higashinosato soils. However, in un-normalised scale the strength was significantly higher for the undisturbed specimens, as shown in **Figure 7.14.** After observing such deviation between the as-compacted and the undisturbed strength envelopes of the similar soils, an additional triaxial test was performed on the as-compacted Maizuru sample prepared with the initial water content same as that of the undisturbed Maizuru soil. The undrained strength of undisturbed sample was found to be significantly lower than the as-compacted sample, as shown in **Figures 7.8** and **7.10**. The undisturbed samples were taken from the depth of about 0.4-0.5m in the month of October during drying period, which was a region of higher strength soil layer showing maximum cone penetration resistance from the surface (see **Figures 7.2** and **7.4**), as explained in the earlier sections. This finding gives a lesson that the strength of the near-surface soil decreased significantly from its initial as-compacted strength with time, possibly due to the influence climatic action such as repeated drying and wetting cycles. It would be hypothetical to assume without observing the actual soil fabrics of undisturbed

samples, but one of the possible reasons for such lower strength could be fabric deterioration due to soil desiccation, with possible volume shrinkage and cracking, during drying period before surface vegetation developed. In the past research, Hen-Jones et al. (2017) also observed the clearly visible cracks in the in-situ near-surface soil from environmental scanning electron microscope (E-SEM) images as a result of desiccation and reported that these cracks could cause the soil fabric deterioration in the clay soils.

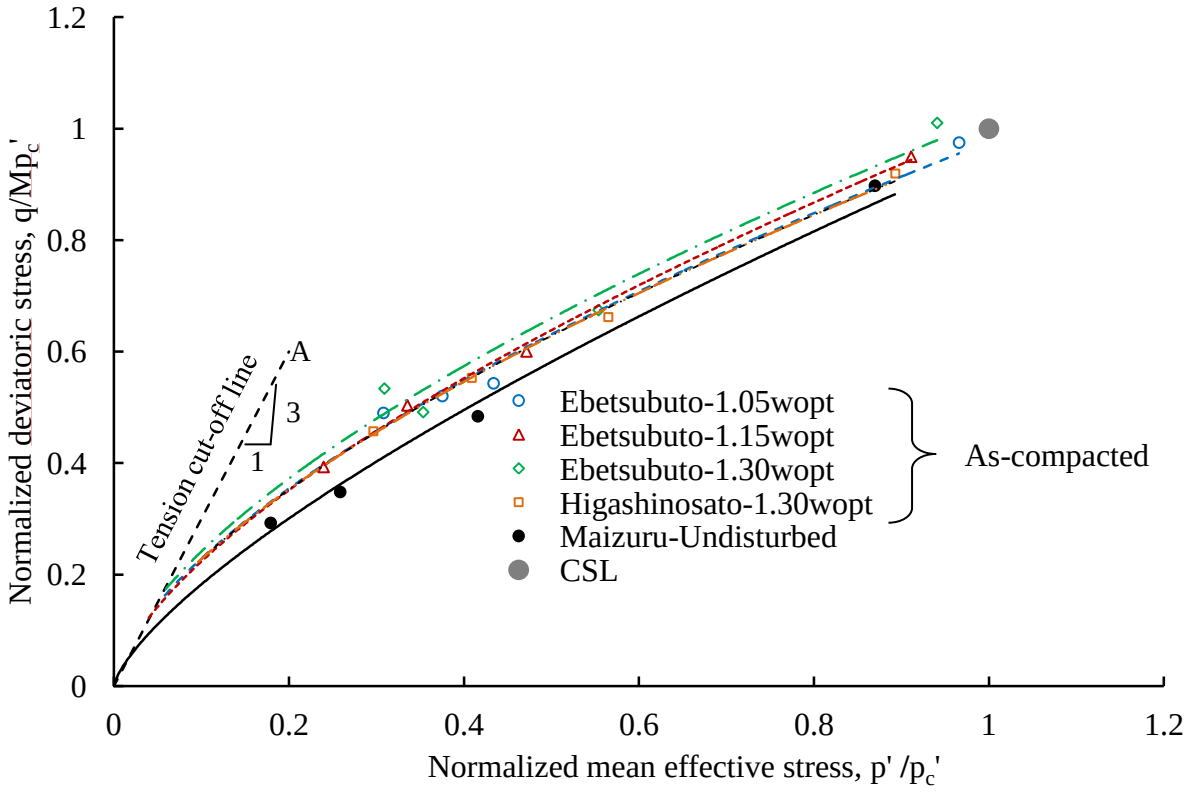

Figure 7.15. Normalized peak strength envelopes for as-compacted Ebetsubuto and Higashinosato soils, and undisturbed Maizuru soil

7.5.2 PEAK STRENGTH AND STRENGTH IN FIELD

The normalised peak strength envelopes for as-compacted Ebetsubuto and Higashinosato soils, and undisturbed Maizuru soil shown in **Figure 7.15** are significantly non-linear compared to those of the un-normalized forms, in which the degrees of non-linearity (η) lie in

a range η=0.63-0.65 for as-compacted soils and η=0.72 for undisturbed soil. These normalized power-law strength equations were derived based on the assumption that the soils have zero inter-particle bonding. The study conducted by Atkinson (2007) on seven overconsolidated clays sampled from compacted motorway embankment slopes, in which the peak strength envelopes at low effective stresses were represented by the non-linear power-law failure criterion, and the normalization was carried out with respect to the critical pressure, found that the degrees of non-linearity of peak strength envelopes were in a range of 0.17-0.73. The study reported that the peak strength envelope was markedly non-linear for clays with the overconsolidation ratio greater than about four. Comparing the degrees of non-linearity of peak strength envelopes obtained in this study with those of the overconsolidated clays, it can be concluded that the degrees of non-linearity of as-compacted and undisturbed clay-sand mixed soils are significantly non-linear which needs careful consideration in the design and slope stability analysis of the embankment.

7.6 FIELD MONITORING

To understand the hydraulic behaviour of river dykes in association with the mechanical behaviour, a long-term field monitoring had been undertaken by a team from Hokkaido University in Maizuru river dyke slope since August, 2014. In this section, the field monitoring data are analysed and discussed, which include measurements of precipitation, pore water pressure, volumetric water content and temperature**.** Although the field monitoring was initiated on 19 August, 2014, in this thesis the data measured during this investigation between 1 January, 2016 and 8 May, 2017 are presented.

7.6.1 MEASUREMENTS OF PRECIPITATION AND SNOW COVER

Observing the data since the very beginning of field monitoring, the immediate maximum precipitation event measured was 204 mm/day on 11 September, 2014. In the following year, on 3 September, 2015, another maximum precipitation event of 110mm/day was also recorded. There were several other medium to small precipitation events, which include seven numbers of events with intensity 50-100mm/day and 21 numbers of events with intensity 20-50mm/day. As the river dyke is located in a snowy cold region of Hokkaido, the maximum snow cover thickness of about 70cm in the year 2014/15 and 50cm in the year 2016/17 were measured. Analysing the data from 1990 to 2010, Yamada et al. (2012) suggested that the frequency of heavy rainfall events are increasing over northern Japan owing to the line-shaped rain bands. The occurrence of line shaped rain bands were as a result of warm sea surface temperature and strong westerly moisture flux.

The records of precipitation during the period of this investigation are presented in **Figure 7.16**. In the figure it can be seen that, the maximum precipitation events were recorded in June and August with intensities 66mm/day and 83mm/day, respectively. These two months are seen considerably rainier than the rest of the year.

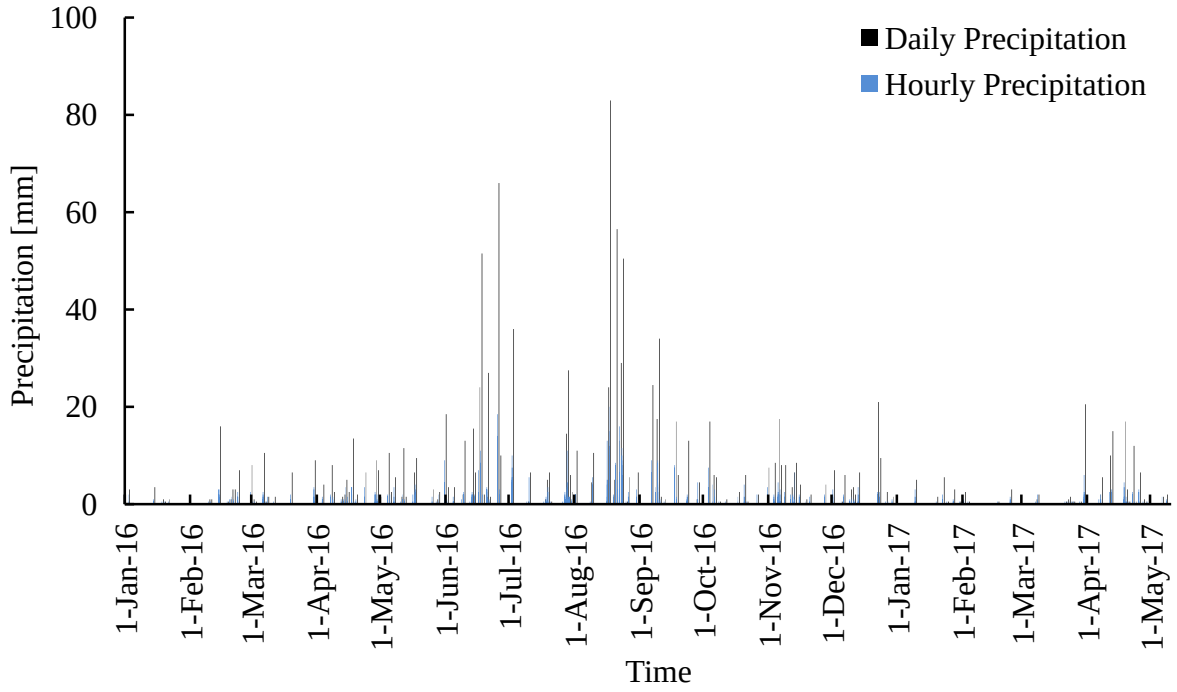

Figure 7.16. Records of daily and hourly rainfall from 1-Jan-2016 to 8-May-2017

7.6.2 MEASUREMENT OF PORE WATER PRESSURE

The time series of field-measured pore water pressure at different depths are presented in **Figure 7.17**. Throughout the period of this investigation, the pore water pressure at shallower depths of 0.4m and 1m reacted sharply in response to precipitation, whereas at deeper depths of 2m and 3m the pore water pressure showed long-term fluctuations in response to seasonal climatic variations. This difference could be due to higher permeability in the near-surface zone and the presence of high strength and potentially low permeability soil layer, as explained earlier; this layer may hinder and delay the moisture movement.

The depth profiles of field measured pore water pressure on the day of cone penereometer tests are presented in **Figure 7.18**. The pore water pressure at shallower depths was closer to hydrostatic pressure (with a level ground assumed) projected from the surface after the snow melting event in March, 2016 and the rainfall events in September, 2016. On the other hand,

the field measured pore water pressure at deeper depths, which was lower than the projected hydrostatic pressure from the surface; this may suggest that the embankment exhibited a significant continuous under-drainage (Nishimura et al., 2015 and 2016). This apparent under-drainage can be explained by the presence of thick volcanic sand layer in the foundation stratigraphy.

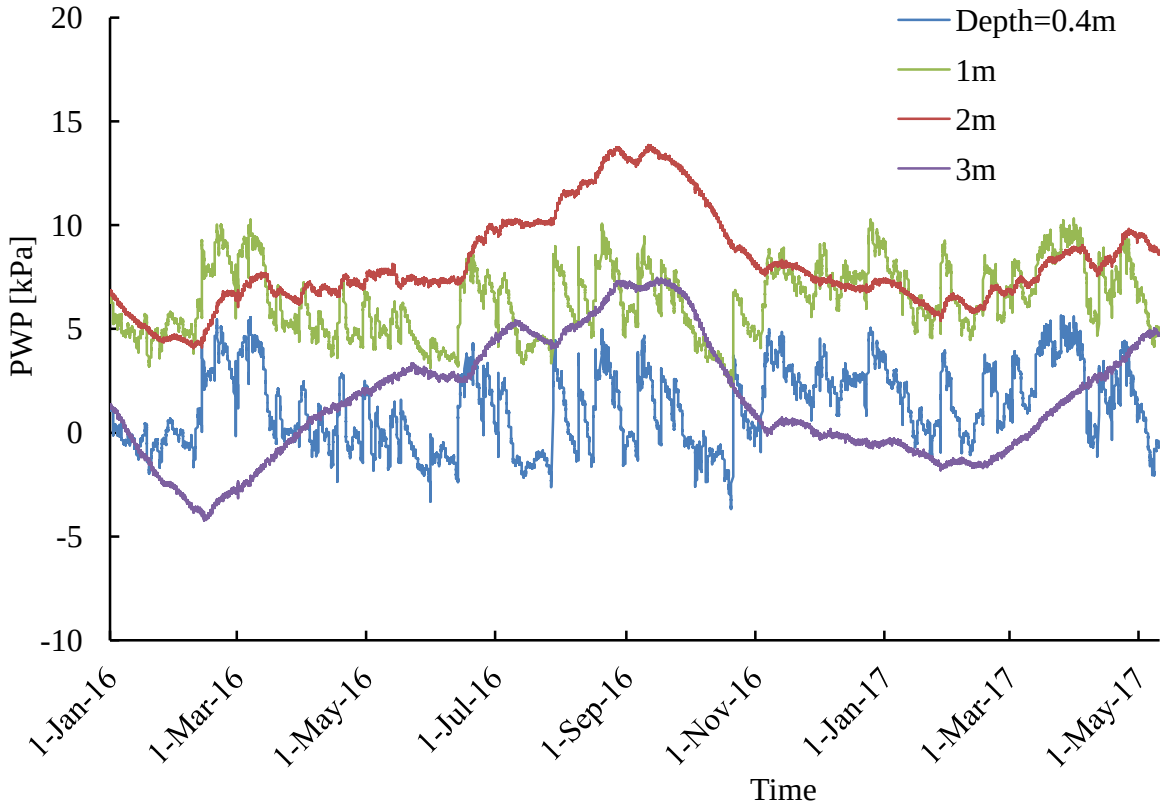

Figure 7.17. Time series of field measured pore water pressure at different depths from 1-Jan-2016 to 8-May-2017

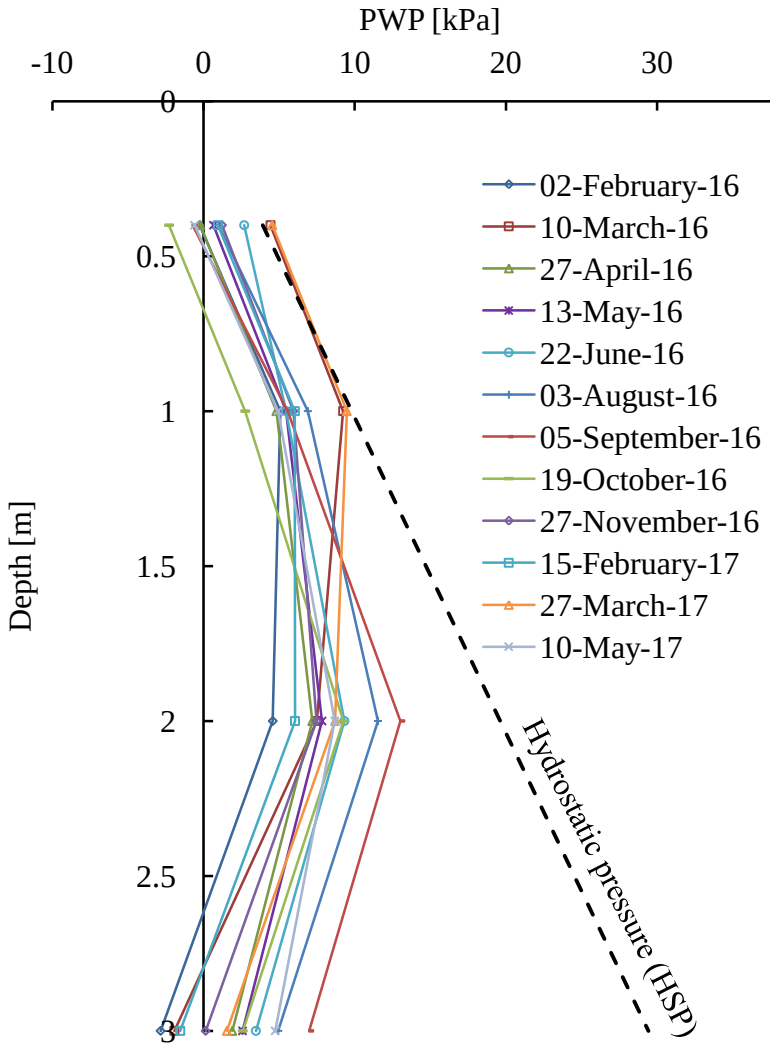

Figure 7.18. Depth profiles of pore water pressure measured on the day of cone penetrometer tests

7.7 NUMERICAL SIMULATION OF PORE WATER PRESSURE

The pore water pressure at different locations was simulated by using a seepage flow model, which considers unsteady unsaturated seepage flow by solving Richards' equation (as discussed by Nguyen et al., 2014) by using non-linear finite element methods. This model also incorporates the evapotranspiration model by using Hamon's (1961) equation. The details of the model and parameters used are presented by Nishimura et al. (2015 and 2016). Thus simulated pore water pressure considering both infiltration and evapotranspiration at

different regions of a slope, compared with the field measured pore water pressure at 0.4m depth, is presented in **Figures 7.19** and **7.20**. The simulated pore water pressure is comparable with the field measured pore water pressure at 0.4m depth, even though the model assumed undrained surface boundaries during the accumulation period of snow and which was converted into the total precipitation and distributed uniformly over the thawing period. The boundary between the accumulation period and the thawing period is defined by the time of peak snow cover thickness. The predicted pore water pressure at different regions reacted sharply with rainfall as observed in the field measurement. In the simulation, the coefficient of permeability for the top 0.5m depth was assumed to have a larger value than the deeper depth. Comparing the predicted profiles of pore water pressure for top-, mid- and toe-regions at shallower depths, the top-region showed slightly lower pore water pressure than other two regions at the same depth, probably due to the gravimetric flow of water towards the mid- and toe-regions keeping soils wetter than the top-region.

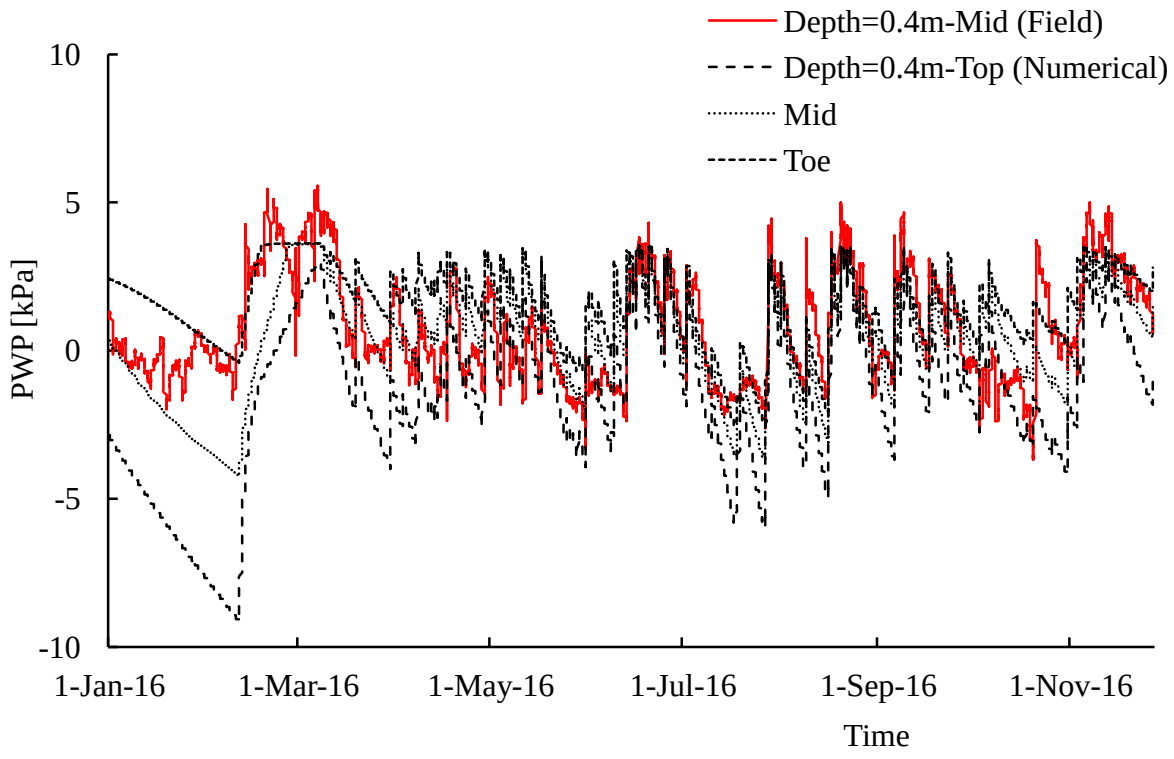

Figure 7.19. Time series of field measured PWP and simulated PWP at 0.4m depth

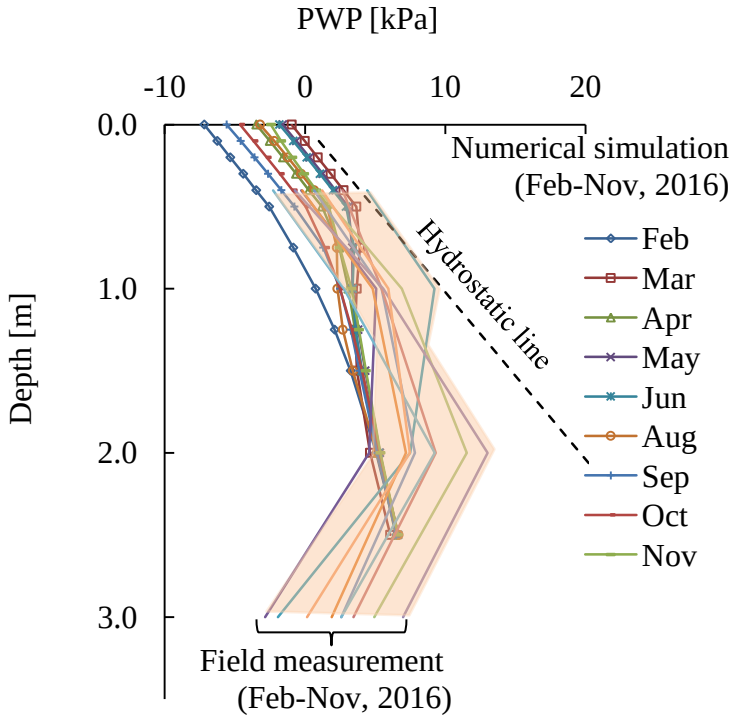

Figure 7.20. Comparison of the field measured and simulated pore water pressure on the day of cone penetrometer testing

7.8 CHARACTERISTICS OF LONG-TERM IN-SITU SURFACE STRENGTH VARIATION

Figure 7.22 shows correlations of the penetration resistance obtained in the Maizuru embankment and the laboratory-compacted model ground of Ebetsubuto soil with the undrained strength obtained from the triaxial compression tests using both the measured and simulated pore water pressure. The undrained strength at each depth in the embankment slope was calculated by using the consolidated-undrained strength envelope of the undisturbed specimens sampled at a depth of 0.4-0.5m in the mid-region closer to the location of cone penetrometer testing. Whereas in the laboratory-compacted model ground, the undrained strength was calculated by using the consolidated-undrained strength envelopes of the same soil compacted with identical initial compaction conditions. In which, the initial consolidation stress at each depth was calculated by using the Terzaghi's effective stress

principle, σ-u_w, as the measured and simulated pore water pressure increased with depth following closely to the hydrostatic line, and showed smaller negative pore water pressure of less than 10kPa within air-entry value of suction, as illustrated in **Figure 7.22**. The depth profiles of field measured water content also showed that the soil was at near-saturated condition when undisturbed sampling was carried out, as shown in **Figure 7.4**.

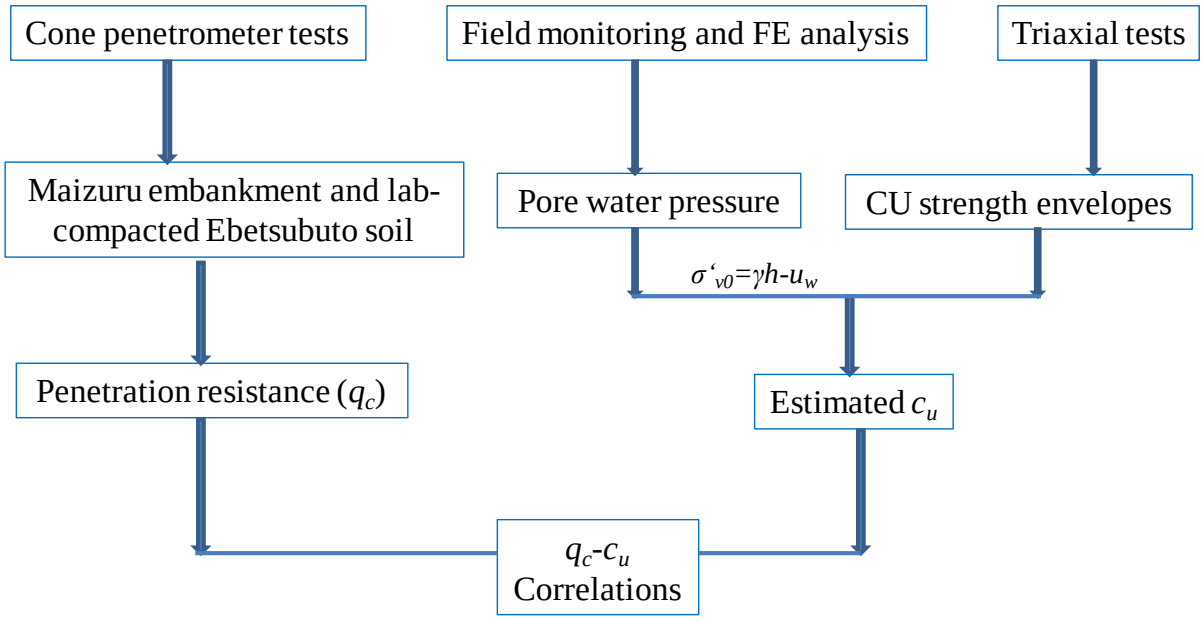

Figure 7.21. Flow chart showing steps followed to make correlations between penetration resistance and undrained strength in the field and laboratory

The correlations of the penetration resistance and the undrained strength in the Maizuru embankment slope were first made for each 0.1, 0.2, 0.3, and 0.4m depth and finally the correlation was also made for overall depth ranging from 0.1 to 0.4m. The linear trend lines drawn for each depth are approximately parallel with each other showing a uniform variation in strength over a period of this investigation, while the trend line for overall depth shows a steep gradient crossing with the trend lines of each depth. The non-unique relationship of penetration resistance with undrained strength for the soil of the same slope could be due to the trend of gradual increment in penetration resistance with depth and the undrained strength

approximated from a single undrained strength envelope obtained from the samples of 0.4-0.5m depth. Similarly, the correlations in the laboratory-compacted model ground were also made for each 0.1, 0.25 and 0.4m depth and overall depth ranging from 0.1 to 0.4m. The linear trend lines for each depth fell close to each other, but did not show a unique relationship, probably due to more compacted soil layers at deeper depth and boundary effect of the container.

Figure 7.23 shows the correlations of the penetration resistance obtained in the field and laboratory from the dynamic cone penetrometer tests with the undrained strength at shallower to deeper depths. The undrained strength was calculated by using the principle of effective stress, as mentioned earlier. By observing the pattern of strength variation in the depth profiles of penetration resistance, the embankment depth has been divided into three regions, and the correlations for each region were made. The correlations show markedly different linear trend of strength variation in three different regions. The trend of strength variation in the top 0-0.5m depth is steep and comparable to that obtained from the correlation of static cone penetration resistance and undrained strength. However, the trends of strength variation in other two regions are significantly different. It should be noted that the trend of strength variation in the bottom 1-3m depth is comparable to that of the laboratory-compacted model ground.

These results and findings will help researchers and engineers to understand and estimate the in-situ strength of river dykes, more importantly due to climate changes, in terms of laboratory undrained strength; however considering drained strength behaviour and partially saturated conditions are out of the scope of this research. Understanding the strength characteristics of river dyke slope with time being by gathering more data is important to assess the true state of soil and understand the mechanism of shallow slope failure.

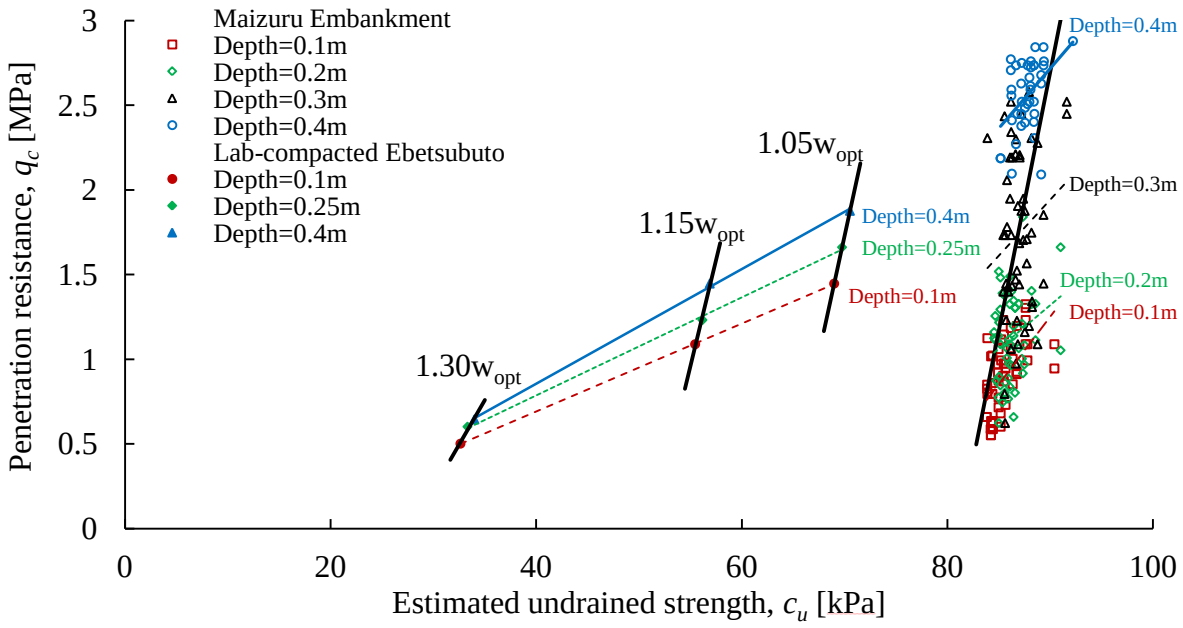

Figure 7.22. Correlations of static cone penetration resistance and undrained strength

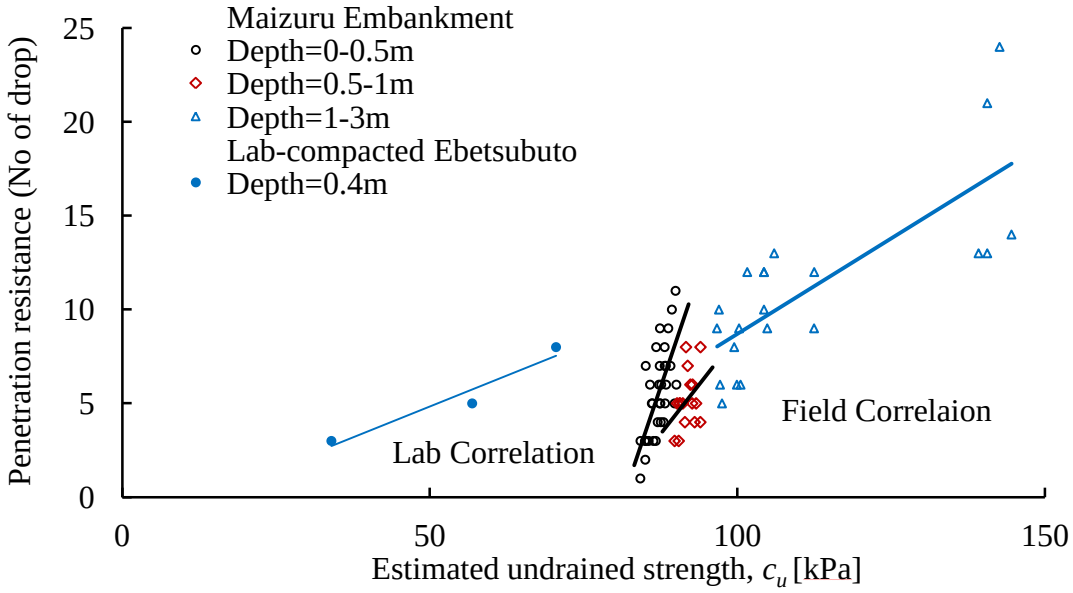

Figure 7.23. Correlations of dynamic cone penetration resistance and undrained strength

CHAPTER 8 CONCLUSIONS, IMPLICATIONS OF RESEARCH FINDINGS AND RECOMMENDATIONS

This chapter presents the conclusions drawn on different parts of this thesis. The implications of research findings and recommendations for future work are also presented.

8.1 CONCLUSIONS

In the first part of this research, an experimental study was carried out to understand the undrained strength behaviour of fine-grained soils in intact and compacted states with reference to reconstituted state at low effective stresses by conducting a series of constant-volume direct shear tests and hollow cylinder simple shear tests. The focus of this study was to characterize the state bounding surfaces at the dry of the critical, with particular emphasis to the compacted state, with reference to the shallow slope stability analysis. The fine-grained soils include two plastic clays such as heavily over-consolidated Izumi clay and soft Atsuma clay, and a clay-sand mixed soil. The non-linearity of strength envelopes constituting the state bounding surfaces were represented by the non-linear power-law strength criterion and the corresponding degree of non-linearity was evaluated. The meso-fabric of both reconstituted and compacted specimens were observed by X-ray micro CT images. The main conclusions are summarized below:

1) The intact Izumi clay showed higher normalized strength (i.e. normalized by its density and apparent overconsolidation ratio) and its degree of its non-linearity than the compacted and reconstituted specimens, due to the presence of natural micro-structure including true inter-particle cohesion enhancing the strength as confirmed by the hollow cylinder simple shear tests. During the hollow cylinder simple shearing, the minor effective stress was evolved towards a negative stress zone before failure in the intact

Izumi clay. However, the intact Atsuma clay and all other reconstituted and compacted samples did not show such features during simple shearing.

2) On the other hand, the compacted specimens of both clays showed significantly lower normalized strength than the reconstituted specimens, while this difference was not notable in the clay-sand mixed soil. This finding means that the undrained strength of compacted clay is not as large as expected for their generally dense states. However, the compacted strength of the clays in an absolute scale may not necessarily lower as provided strength by its density or apparent overconsolidation ratio. Although the clay-sand mixed soil was dominated by clay, its transitional behaviour made the difficulty in determining a well-defined ICL, leaving a degree of uncertainty in the normalized strength. Comparing the degrees of non-linearity of the normalized strength envelopes constituting the non-linear bounding surfaces for the reconstituted and compacted states of each soil, they were comparable.

3) Interestingly, the X-ray micro-CT images revealed that the compacted specimens of both clays exhibited numerous large pores forming fissure-like discontinuities with a size as much as 10mm, while they were absent in the reconstituted specimens. The occurrence of these discontinuities could be due to air entrapment between clay aggregates during compaction, perhaps aggravated by swelling to low effective stresses as the air in the confined large pores rebounded. Whereas the compacted clay-sand mixed soil specimen showed fewer obvious discontinuities, possibly due to the presence of coarser soil particles and lower overall plasticity in the soil, preventing forming clear continuous discontinuities. Although these discontinuities may close under confining pressure, it is likely that they affect the ultimate shear strength. Although qualitatively, the lower normalized strength in the compacted clays can be explained by these discontinuities. It is important to note that the compacted specimen is associated with a meso-fabric

significantly different than the reconstituted specimens, and cannot be considered as just dense and destructured, higher-OCR reconstituted state.

4) The hollow cylinder simple shear stress paths largely conformed to the state bounding surface established by the constant-volume direct shear tests, although they showed more dilative behavior. The more dilative tendency of the hollow cylinder stress paths at low stresses could be due to differences in boundary kinematics and resulting uniform simple shear deformation mode throughout the specimens. However, it is an open question whether hollow cylinder or direct shear deformations give the true field behavior, although hollow cylinder stress paths represent true constant-volume behaviour. The less dilative tendency in direct shear tests generally leads to safer undrained strength assessment.

The second part of this study was carried out by focusing on characterizing the spatial and temporal variations in strength of two river dyke slopes, i.e. 3-5 years aged Maizuru river dyke supplemented by recently-constructed Higashinosato river dyke, particularly in the near-surface zone. The portable static/dynamic cone penetrometer tests were performed on a monthly basis in 2016/2017 to investigate the surface strength in the river dyke slopes. The results were interpreted with reference to the strength of a laboratory-compacted model ground. A series of consolidated-undrained triaxial compression tests were performed on laboratory (as)-compacted soils such as Ebetsubuto soil and Higashinosato soil compacted with different water contents ($1.05w_{opt}$, $1.15w_{opt}$, and $1.30w_{opt}$) and field compacted (undisturbed) and as-compacted samples from Maizuru river dyke. The main conclusions are summarized as follows:

1) The depth profiles of average penetration resistance in the Maizuru river dyke slope indicate that the soil strength increased gradually with depth in each region (top, mid,

and toe), and the top-region showed maximum strength than the other two regions at a same depth illustrating a small spatial variation in strength.

2) All the depth profiles of average penetration resistance in the Maizuru river dyke slope converged into a narrow region indicating a small temporal variation in soil strength due to monthly and seasonal changes in pore water pressure, which was not as significant as expected as the positive pore water pressure near the surface was measured close to hydrostatic levels all the time.

3) The surface strength of Maizuru river dyke at a depth of 0.4-0.5m depth showed higher strength than both the recently-constructed Higashinosato river dyke and the laboratory-compacted model ground, which were young and showed uniform strength along the depth. This may indicate that the Maizuru surface was subject to crusting (overconsolidation of clays as a result of desiccation) after a few cycles of seasons.

4) The results of consolidated-undrained triaxial tests on the different states of laboratory-compacted Ebetsubuto and Higashinosato soils and undisturbed Maizuru soil at a depth of about 0.4-0.5m showed approximately unique critical state lines for different states of the same soil in a q-p' plane, but significantly different in a v-logp' plane depending on initial densities, which indicates the transitional behaviour in the clay-sand mixed soil. To characterize the strength of these soils by following the approach similar to the first part of this study, the normalization of strength was carried out by using these separate critical state lines.

5) Comparing all the normalised peak strength envelopes, the normalised strength of undisturbed samples from Maizuru was slightly lower than that of all the as-compacted samples of similar Ebetsubuto and Higahinosato soils. However, in an un-normalised form it was significantly higher as provided strength by its density and apparent overconsolidation. The lower normalized strength of the field compacted samples than

the as-compacted samples could be as a result of soil fabric deterioration after five years of aging in Maizuru river dyke due to climatic variations and some micro/meso-structural features reducing the soil strength, which needs further investigation. The degrees of non-linearity of the normalized peak strength envelopes constituting the non-linear state bounding surfaces were comparable with each other.

6) The correlations of field and laboratory measured penetration resistances and the estimated undrained strength using both the measured and simulated pore water pressure showed significantly different linear trend lines at different depths, without unique relationship, which needs further investigation.

8.2 MPLICATIONS OF REAEARCH FINDINGS

The results and findings in the first part of this research by performing a series of constatnt-volume direct shear tests supplemented by hollow cylinder simple shear tests on intact, reconstituted and compacted fine-grained soils contribute significantly to the design and slope stability analysis of geotechnical earth structures such as river dykes. Application of non-linear power-law strength criterion to evaluate the undrained strength parameters and state bounding surfaces at low effective stresses will help researchers and engineers to understand the appropriate conditions and behaviour of compacted soils. Particularly, the significantly different undrained strength behaviours between reconstituted and compacted clays at the same density give lesson that the compacted strength cannot be represented simply by the dense and destructured reconstituted clay. The compacted strength characteristics are governed by the meso-structures including inter- and intra-aggregate large pores in contrast to reconstituted clays.

The results and findings in the second part of this research will help researchers and engineers to understand and estimate the in-situ strength of river dykes, more importantly due

to climate changes, in terms of laboratory undrained strength; however considering drained strength behaviour and partially saturated conditions are out of the scope of this research. The results of long-term in-situ strength testing and field monitoring help understand the characteristics of near-surface soil strength in terms of spatial and temporal variations. The findings on the different strength behaviour between field compacted samples and the laboratory compacted samples at the same density help use appropriate strength parameters for solving the problem of shallow slope stability analysis. Understanding the strength characteristics of river dyke with time being by gathering more data is important to assess the true state of soil and understand the mechanism of shallow slope failure.

8.3 RECOMMENDATIONS

The recommendations for future work, which can help improve understanding of the results from the both parts of this research, are as follows:

1. Series of triaxial compression tests on both intact and compacted clays are required to understand the strength behaviour of compacted intermediate clay-sand mixed soils. As all the results from the triaxial tests are only on the clay-sand mixed soils, comparison of similar results on conventional clay may help understand rigorously the transitional behaviour.
2. Uncertainties in evaluating the normalised strength and its non-linearity as a result of state normalization based on ICL and CSL, particularly for clay-sand mixed soils, need further investigation with reference to clays. The uncertainties might be due to difficulty in getting well-defined ICL within a limited vertical effective stress range of 3000kPa and CSL due to incomplete shearing in the clay-sand mixed transitional soils.
3. The correlations of penetration resistance and estimated undrained strength for different depths in the Maizuru river dyke were made by estimating undrained strength with

reference to the undisturbed samples from 0.4-0.5m depth, which could be a reason for the non-unique relationship between the penetration resistance and the undrained strength consistent with laboratory correlation for depths shallower than 0.4-0.5m depth. Estimation of undrained strength from the samples of each depth may help understand the strength characteristics in response to climate with unique correlation.

REFERENCES

Abraham, C. F. Chiu, Zao, X. & Yuan, J. P. (2010). State boundary surfaces for an aged compacted clay. *J. Geotech. Geoenviron. Eng. ASCE* **136**, No. 9, 1251-1262.

Albert, C., Zdravkovic, L., & Jardin R. J. (2003). Behaviour of Bothkennar clay under rotation of principal stresses. *International Workshop on Geomechanics of Soft Soils – Theory and Practice*. 441-446

Allam, M. M. & Sridharan, A. (1981). Effect of wetting and drying on shear strength. *Journal of the Geotechnical Engineering Division, ASCE* **107**, No. 4, 421-438.

Alonso, E. E., Pinyol, N. M. & Gens, A. (2013). Compacted soil behaviour: initial state, structure and constitutive modelling. *Géotechnique* **63**, No. 6, 463-478.

Athapaththu, A. M. R. G., Tsuchida, T., & Kano, S. (2015). A new geotechnical method for natural slope exploration and analysis. *Natural Hazards* **75**, No. 2, 1327-1348.

Atkinson, J. (2007). Peak strength of overconsolidated clays. *Géotechnique* **57**, No. 2, 127-135, http://dx.doi.org/10.1680/geot.2007.57.2.127.

Atkinson, J. H. & Bransby, P. L. (1968). The mechanics of soils. London: McGraw-Hill.

Baker, R. (2004). Nonlinear Mohr envelopes based on triaxial data. *J. Geotech. Geoenviron. Eng.* **130**, No. 5, 498-506.

Barden, L., & Sides, G. R. (1970). Engineering behaviour and structure of compacted clay. *J. Soil Mech. and Found. Div.* **96**, 1171-1200.

Bishop, A. W., Wedd, D. L. & Lewin, P. I. (1965). Undisturbed samples of london clay from the ashford common shaft: strength-effective stress relationships. *Géotechnique* **15**, No. 1, 1-31.

Burland, J. B. (1990). On the compressibility and shear strength of natural clays: 30th Rankine lecture. *Géotechnique* **40**, No. 3, 327-328.

Burland, J. B., Rampello, S., Georginnou, V. N., & Calabresi, G. (1996). A laboratory study of the strength of four stiff clays. *Géotechnique* **46**, No. 3, 491-514.

Charles, J. A. (1982). An appraisal of the influence of a curved failure envelope on slope stability. *Géotechnique* **32**, No. 4, 389-392, http://dx.doi.org/10.1680/geot.1982.32.4.389.

Chen, H., Lee, C. F., & Law, K. T. (2004). Causative mechanisms of rainfall induced fill slope failures. *J. Geotech. Geoenviron. Eng. ASCE,* **130**, No. 6, 593-602.

Coop, M. (2015). Limitations of a critical state framework applied to the behaviour of natural and transitional soils. *Proc. 6th Int. Symp. Deform. Characterist. Geomater.*, Buenos Aires **6**, 115-155.

Coop, M. (1990). The mechanics of uncemented carbonate sands. *Géotechnique* **40**, No. 4, 607-626, http://dx.doi.org/10.1680/geot.2006.56.7.447.

Cotecchia, F. & Chandler, R. J (1997). The influence of structure on the pre-failure behaviour of a natural clay. *Géotechnique* **47**, No. 3, 523-544.

Cuisinier, O. & Laloui, L. (2004). Fabric evolution during hydromechanical loading of a compacted silt. *International Journal for Numerical and Analytical methods in Geomechanics* 26. 483-499.

Day, R.W., & Axten G.W (1989). Surficial stability of compacted clay slopes. *J. Geotech. Eng.* **115**, No. 4, 577-580.

Day, R. W. (1992). Effective cohesion for compacted clay. *J. Geotech. Eng.* **118**, No. 4, 611-619.

de Mello, V. F. B (1977). Reflections on design decisions of practical significance to embankment dams. *Géotechnique* **27**, No. 3, 281-355.

Dijkstra, T. A. & Dixon, N. (2010). Climate change and slope stability in UK: Challenges and approaches. Quaterly Journal of Engineering Geology and Hydrogeology 43, No. 4, 371-385.

Fleming, L. N. & Duncan, J. M. (1990). Stress-deformation characteristics of Alaskan silt. *Journal of Geotechnical Engineering* **116**, No. 3, 377-393.

Ferreira, P. M. V. & Bica, A. V. D. (2006). Problems in identifying the effects of structure and critical state in a soil with a transitional behaviour. *Géotechnique* **56**, No. 7, 445-454, http://dx.doi.org/10.1680/geot.1990.40.4.167.

Fourie, A. B., Rowe D., & Blight, G. E. (1999). The effect of infiltration on the stability of slopes of a dry ash dump. *Géotechnique* **49**, No. 1, 1-13.

Fukutomi, Y. (2015). Undrained strength anisotropy of soft natural clays and influencing factors. *Master Thesis*, Hokkaido University.

Gamez, J. A. & Stark, T. D. (2014). Fully softened shear strength at low stresses for levee and embankment design. *J. Geotech. Geoenviron. Eng. ASCE*, 060140010-1-06014010-6.

Gasparre, A., Nishimura S., Coop, M. R. & Jardine, R. J. (2007). The influence of structure on the behavior of London clay. *Géotechnique* **57**, No. 1, 19-31.

Gens, A. (1996). Constitutive modeling: Application to compacted soils. Proceeding, Ist *International Conference on Unsaturated Soils. Balkema, Rotterdam, The Netherlands: Delage, eds.*, 1179-1200.

Glendinning, S., Hughes, P., Helm, P., Chambers, J., Mendes, J., Gunn, D., Wilkinson, P., & Uhlemann, S. (2014). Construction, management and maintenance of embankments used for road and rail infrastructure: implications of weather induced pore water pressures. *Acta Geotechnica* **9**, 799-816.

Hall, S., Bornert, M., Desrues, J., Pannier, Y., Lenoir, N., Viggiani, G. & Bésuelle, P. (2010). Discrete and continuum analysis of localised deformation in sand using X-ray μCT and volumetric digital image correlation. *Géotechnique* **60**, No. 5, 315-322,.

Hamon, W. R. (1961). Estimating potential evapotranspiration. *Journal of the Hydraulics Division, ASCE* **87**, No. 3, 2817-2822.

Hen-Jones, R. M., Hughes, P. N., Stirling, R. A., Glendinning, S., Chambers, J. E., Gunn, D. A. & Cui, Y. J. (2017). Seasonal effects on geophysical-geotechnical relationships and their implications for electrical resistivity tomography monitoring of slopes. *Acta Geotechnica* **12**, No. 5, 1159-1173.

Hight, D. W., Gens, A. & Symes, M. J. (1983). The development of a new hollow cylinder apparatus for investigating the effects of principal stress rotation in soils. *Géotechnique* **33**, No. 4, 355-383, http://dx.doi.org/10.1680/geot.1983.33.4.355.

Hosseini Kamal, R., Coop, M. R., Jardine, R. J. & Brosse, A. (2014). The post-yield behavior of four Eocene-to-Jurassic UK stiff clays. *Géotechnique* **64**, No. 8, 620-634.

Hvorslev, M. J. (1937). Uber die Festigkeitseigenschaften Gestorter Bindinger Bodn. Denmarks Naturvidenskabelige Samfund. *Ingeniorvidensk. Skr.* A, No. 45.

Japanese Geotechnical Society (JGS), Laboratory Testing Standards for Geomaterials (2015). Vol. 1-3

Kim, B. S., Park, S. W., Takeshita, Y. & Kato, S. (2016). Effect of suction stress on critical state of compacted silty soils under low confining pressure. *International Journal of Geomechanics* **16**, No. 6, D4016010-1-11.

Lambe, T. W. (1958). The engineering behaviour of compacted clays. Journal of the Soil Mechanics and Foundation Division ASCE **84**, 1-35.

Lambe, T.W., Whitman, R.V. (1979). Soil Mechanics. New York, John Wiley & Sons, Inc.

Lee, M. L., Gofar, N. L. & Rahardjo, H. (2009). A simple model for preliminary evaluation of rainfall-induced slope instability. *Engineering Geology* **108**, No. 3-4, 272-285.

Leroueil, S. & Vaughan, P. R. (1990). The general and congruent effects of structure in natural soils and weak rocks. *Géotechnique* **40**, No. 3, 467-488.

Loveridge, F. A., Spink, T. W., O'Brien, A. S., Briggs, K. M. & Butcher, D. (2010). The impact of climate and climate change on infrastructure slopes, with particular reference to southern England. *Quarterly Journal of Engineering Geology and Hydrogeology* **43**, No. 4, 461-472.

Maksimovic, M. (1989). Nonlinear failure envelope for soils. *J. Geotech. Eng.* **115**, No. 4, 581-586.

Mandaglio, M. C., Moraci, M., Rosone, M., & Farulla, C. A. (2016). Experimental study of a naturally weathered stiff clay. *Canadian Geotechncal Journal* **53**, 2047-2057.

Mesri, G. (1993). Cohesion intercept in effective-stress stability analysis. *J. Geotech. Engrg.* **119**, 1229-1249.

Mitachi, T., & Kitago, S. (1976). Change in undrained shear strength characteristics of saturated remolded clay due to swelling. *Soils and Foundations* **16**, No. 1, 45-58.

Mitchell, J. K. (1976). Fundamental of soils behaviour. John Wiley & Sons, Inc.

Mitchell, J. K. & Soga, K.(2005). Fundamental of Soil Behaviour. John Willey and Sons.

Miura, M., Takahashi, M., Kawajiri, S., Torii, N. & Shibuya, S. (2011). Strength-deformation characteristics of a compacted soil over a wide strain range. *Proceeding of the sixth international symposium on deformation characteristics of geomaterials.* Seoul, Korea, 322-327.

Ng. C. W. W., Zhan, C. T., Bao, C. G., Fredlund, D. G. & Gong, B. G. (2003). Performance of and unsaturated expansive soil slope subjected to artificeal rainfall infiltration. *Géotechnique* **53**, No. 2, 143-157.

Nguyen, M. N., Bui, T. Q., Yu, T. & Hirose, S. (2014). Isogeometric analysis for unsaturated flow problems. *Computers and Geotechnics* **62,** 257-267.

Nishimura, S., Tokoro, T., & Rivas, M. F. (2016). Interpretation of hydraulic states in fine-grained soil embankment by considering rainfall infiltration and evapotranspiration. *51st JGS annual conference.* Okayama, 1035-1036.

Nishimura, S., Tokoro, T., Yamada, T., Izumi, N & Rivas, M. F. (2015). A case study of long- and short-term hydraulic state changes in embankment in Hokkaido. *Japanese Geotechnical Society special publication* 1, No. 7, 34-39.

Nishimura, S. (2014). Cross-anisotropic deformation characteristics of natural sedimentary clays. *Géotechnique* **64**, No. 12, 981-996, http://dx.doi.org/10.1680/geot.14.P.088.

Nishimura, S., Jardin, R. J. & Brosse, A. (2008). Simple shear testing of London clay in hollow cylinder apparatus. *4th International Symposium on Deformation Characteristics of Geomaterials*. Atlanta, 199-206.

Nishimura, S., Minh, N. A. & Jardine, R. J. (2007). Shear strength anisotropy of natural London clay. *Géotechnique* **57**, No. 1, 49-62.

O'Brien, A., Ellis, E. A., & Russel, D. (2004). Old railway embankment clay fill: laboratory experiments, numerical modelling and field behaviour. *Advances in geotechnical engineering: Proceedings of the Skempton Conference,* London, Imperial College, 911-921.

Panta, A., & Nishimura, S. (2017). Characterisation of state bounding surface at low effective stresses in clayey soils having different structures. *Géotechnique* 67, No. 6, 394-409.

Parry, R. H. G. (1968). Field and laboratory behaviour of a lightly overconsolidated clay. *Géotechnique* **18**, No. 2, 151-171.

Parry, R. H. G. (1970). Overconsolidation in soft clay deposits. *Géotechnique* **20**, No. 4, 442-446, http://dx.doi.org/10.1680/geot.1970.20.4.442

Porovic, E. (1995). Investigation of soil behaviour using a resonant-column torsional shear hollow-cylinder apparatus . *PhD Thesis.* Imperial College, University of London.

Potts, D. M., Dounias, G. T. & Vaughan, P. R. (1987). Finite element analysis of the direct shear box test. *Géotechnique* **37**, No. 1, 11-23, http://dx.doi.org/10.1680/geot.1987.37.1.11.

Pournaghiazar, M., and Russel, A. R. & Khalili, N. (2013). The cone penetration test in unsaturated sands. *Géotechnique* **63**, No. 14, 1209-1220.

Rahardjo, H., Lim, T. T., Chang, M. F., & Fredlund, D. G. (1995). Shear strength characteristics of a residual soil. *Canadian Geotechnical Journal* **32**, 60-77.

Rahardjo, H., Rezaur, R. B., Leong, E. C., Alonso, E. E., Loret, A. & Gens, A. (2008). Monitoring and modeling of slope response to climate changes. Edited by Chen et al. (eds. *10th International Symposium on Landslides and Engineered Slopes-Chen et al. (eds).* China: Taylor & Francis Group, London, 67-84.

Roscoe, K. H. (1953). An aparatus for the application of simple shear to soil samples. *Proceedings of 3rd International Conference on Soil Mechanics and Foundation Engineering.* Zurich, 186-191.

Amorosi, A., & Rampello, S. (2007). An experimental investigation into the mechanical behaviour of structured stiff clay. *Geotechnique* **57**, No. 2, 153-166.

Saada, A. S. & Townsend, F. C. (1981). State-of-the-art: Laboratory strength testing of soils. *Laboratory shear strength of soil, ASTM STP* **740**, 7-77.

Schofield, A. N. & Wroth, C. P. (1968). Critical state soil mechanics. London: McGraw-Hill.

Seed, H. B. & Chan, C. K. (1959). Structure and strength characterisyics of compacted clays. *J. Soil Mech. Found. Div., ASCE*, **85**, No. SM5, 87-128.

Shi, X. S., Herle, I., & Bergholz, K. (2017). A nonlinear Hvorslev surface for highly overconsolidated soils: elastoplastic and hypoplastic implementations. *Acta Geotechnica* **12**, No. 4, 809-823.

Shipton, B. & Coop, M. R. (2012). On the compression behaviour of of reconstituted soils. *Soils Founds* **52**, No. 4, 668-681.

Smethurst, J. A., Clarke, D., & Powrie, W. (2012). Factors controlling the seasonal variation in soil water content and pore water pressures within a lightly vegetated slope. *Géotechnique* **62**, No. 5, 429-446.

Springman, S. M., Thielen, A., Kienzler, P. & Friedel, S. (2013). A long-term field study for the investigation of rainfall-induced landslides. *Geotechnique* **63**, No. 14, 1177-1193.

Sridharan, A., Altaschaeffl, A. G., & Diamon, S. (1971). *Pore size distribution studies. Journal of the Soil Mechanics and Foundation Division ASCE* **97**, 771-787.

Stirling, R. A., Glendnning, S. & Davie, C. T. (2017). Modelling the deterioration of the near surface caused by drying induced cracking. *Applied Clay Science* **146**, 176-185.

Talesnick, M. & Frydman, S. (1991). Simple shear of an undisturbed soft marine clay in NGI and torsional shear equipment. *Geotechnical Testing Journal* **14**, No. 2, 180-194.

Tarantino, A. & De Col, E. (2008). Compaction behaviour of clay. *Geotechnique* **58**, No. 3, 199-213. http://dx.doi.org/10.1680/geot 2008.58.3.199.

Tatsuoka, F. (2015). Compaction characteristics of physical properties of compacted soil controlled by the degree of saturation. *Proc. 6th Int. Symp. Deform. Characterist. Geomater.*, Buenos Aires **6**, 40-76.

Tatsuoka, F. (2011). Laboratory stress-strain tests for developments in geotechnical engineering research and practice. *Proc. 5th Int. Symp. Deform. Characterist. Geomater.*, Buenos Aires **1**, 3-50.

VandenBerge, D. R., Brandon, T. L.. & Duncan, J. M. (2014). Triaxial tests on compacted c;ays for consolidated-undrained conditions. *Geotechnical Testing Journa* l **37**, No. 4. 1-12.

Viggiani, G. & Hall, S. A. (2008). Full-field measurements, a new tool for laboratory experimental geomechanics. *Proc. 4th Int. Symp. Deform. Characterist. Geomater.*, Atlanta **1**, 3-26.

Vitone, C. & Cotecchia, F. (2011). The influence of intense fissuring on the mechanical behavior of clays. *Géotechnique* **61**, No. 12, 1003-1018.

Wang, Q., Cui, Y. J., Tang, A. M., Xing-Ling, L. & Wei-Min, Y. (2014). Time- and density - dependent microstructure features of compacted bentonite. *Soils Found.* **54**, No. 4, 657-666.

Xu, L. & Coop, M. R. (2016). The mechanics of a saturated silty loesses with a transitional mode . *Geotechnique **67***, No. 7, 581-596, http://dx.doi.org/10.1680/geot.16.P.128.

Yamada, J. T., Sasaki, J., & Matsuoka, N. (2012). Climatology of line-shaped rainbands over northern Japan in boreal summer between 1990 and 2010. *Atmospheric Science Letters* **13**, 133-138.

Yang, H. & Russel, A. R. (2015). Cone penetration tests in unsaturated silty sands. *Canadian Geotechnical Journal* **53**, 431-444.